



**NANYANG
TECHNOLOGICAL
UNIVERSITY**

PULSED FIBER LASER AT 1 μm WAVELENGTH REGION

LIU MENG

SCHOOL OF ELECTRICAL & ELECTRONIC ENGINEERING

2017

**PULSED FIBER LASER AT 1 μm WAVELENGTH
REGION**

LIU MENG

SCHOOL OF ELECTRICAL & ELECTRONIC ENGINEERING

**A THESIS SUBMITTED TO
THE NANYANG TECHNOLOGICAL UNIVERSITY
IN PARTIAL FULFILLMENT OF THE REQUIREMENTS FOR THE DEGREE OF
DOCTOR OF PHILOSOPHY**

ACKNOWLEDGEMENT

It has been four years since I started my PhD journey in Nanyang Technological University. Although filled with many tough times and pressures, it has been a pleasant, enriching, and meaningful journey for me. Without the help from many talented and kind individuals, this journey would not have been possible. I'd like to take this opportunity to express my sincere appreciation to them.

First of all, I'd like to grant my deepest gratitude to my supervisor Prof. Shum Ping. I've benefited tremendously from his wisdom and professional guidance all the way along my PhD journey. His constant encouragement and indomitable spirit towards difficulty, his helpful mind and kindness to others have inspired me and will continue to influence me in the future life journey.

I'd like to express my most heartfelt appreciation to my industrial mentor Dr. Cheng Xueping who introduced me to the fiber laser project eight year ago. He rendered me consistent supports to pursue PhD study by encouraging me and sharing my work load when I don't have sufficient time during the PhD study especially for the last two years.

My deepest thanks go to Assoc. Prof. Wang Qijie who gives me invaluable help, and it will always be remembered. Your hard-working and concentration spirit always inspires me.

I would also like to give my sincere appreciation to Dr. Liu Jian and Mr. Huang Zhijia who give lots of support during my PhD study. Highly appreciation goes to Dr. Liu Jian for his kind consideration and help on the workload-sharing during my last year of PhD

study.

Lots of appreciations are presented to Dr. Zhang Jing, Dr. Yang Yanfu, Dr. Liu Huanhuan, Zhang Meng, Yan Zhiyu, Chen Shaoxiang, Dr. Li Xiaohui, Dr. Tse Junho, Xiong Zhaoqi, Liu Aijiang, Zhu Jiangjie, Zhou Huanxian, Gu Jian, Shuai Simin, Zhang Mengxiong, Hu Shanshan, Lei Meng, Bin Xiangwei, colleagues from JPT Inc. and technicians of the NTU labs for their great help and valuable advice.

Last but not least, I would like to send the heartfelt gratefulness to my family members: my parents, mother-in-law, my wife, siblings and daughters. Thanks for your support and understanding along the life journey. You are the root source for me to do all these things.

TABLE OF CONTENTS

<i>Acknowledgement</i>	<i>i</i>
<i>Table of Contents</i>	<i>iii</i>
<i>Summary</i>	<i>vi</i>
<i>List of Tables</i>	<i>xv</i>
<i>List of Acronyms and Symbols</i>	<i>xvi</i>
Chapter 1 Introduction	17
1.1 Background and Motivation	17
1.2 Objectives	19
1.3 Major Contributions	19
1.4 Outline of the Thesis	21
1.5 Publications and Patents	24
1.5.1 Publications	24
1.5.2 Patents	25
Chapter 2 Background Information and Literature Review	26
2.1 History and current status of pulsed fiber laser with 1 micrometer wavelength	26
2.2 Fundamental elements for pulsed fiber laser	29
2.2.1 Double cladding fiber (DCF)	29
2.2.2 Ytterbium (Yb^{3+}) doped fiber	31
2.2.3 Limiting factors for pulsed fiber laser with 1 μm wavelength	35
2.2.3.1 Thermal damage limitation	36
2.2.3.2 Self-focusing and Self-phase modulation (SPM)	37
2.2.3.3 Gain Saturation	38
2.2.3.4 Stimulated Brillouin scattering (SBS)	39
2.2.3.5 Stimulated Raman Scattering (SRS)	41
2.2.3.6 Mode instabilities	44
2.2.4 Step-index large mode area (LMA) fiber and photonic crystal fiber (PCF) LMA	45
2.2.5 Configurations of high power Ytterbium-doped pulsed fiber lasers	47
2.3 Laser applications by high power Ytterbium-doped pulsed fiber lasers	48
2.4 Summary	49
Chapter 3 Pulsed Pump Ytterbium-doped Pulsed Fiber Laser	51
3.1 Introduction	51
3.2 Numerical model of Ytterbium-doped pulsed fiber amplifier	52
3.2.1 Theoretical Modeling	53
3.2.2 Laser Pulses Analysis and Characteristics	55

3.2.2.1	Amplifier working with different P_p and t_p	55
3.2.2.2	Amplifier working with same pump energy	58
3.2.2.3	Amplifier working with different injecting seed laser	60
3.2.3	Discussion and Conclusion	61
3.3	Pulsed pump for Ytterbium-doped pulsed fiber laser with tunable pulse duration	63
3.3.1	Experimental Design	65
3.3.2	Results and discussion	69
3.3.3	Conclusion	81
3.4	Summary	82
Chapter 4	<i>High power Ytterbium-doped Pulsed Fiber Laser</i>	85
4.1	Introduction	85
4.2	Seed laser pulse shaping for high power Ytterbium-doped pulsed fiber lasers	86
4.2.1	Definition of UPER	87
4.2.2	Pulse shape distortion for high power Ytterbium-doped pulsed fiber lasers	88
4.2.3	Pulse shaping for Ytterbium-doped pulsed fiber lasers	91
4.2.4	Conclusion	97
4.3	High average power Ytterbium-doped pulsed fiber laser	99
4.3.1	Configuration of the Ytterbium-doped pulsed fiber lasers	99
4.3.2	Discuss on the seed and cascade amplifier stage	103
4.3.3	Conclusion	114
4.4	High peak power Ytterbium-doped pulsed fiber laser	116
4.4.1	Seed laser with adjustable pulse duration from ps to ns	117
4.4.2	Experimental setup	118
4.4.3	Seed and 1 st -amplifier stage	120
4.4.4	2 nd -amplifier and 3 rd -amplifier stages	123
4.4.5	Conclusion	129
4.5	Summary	130
Chapter 5	<i>Nanosecond Pulsed Fiber Laser Blackening of Aluminum Alloy with Alumina Surface</i>	134
5.1	Introduction	134
5.2	Experimental Setup	135
5.3	Mechanisms behind the Blackening	135
5.4	Feasibility of the Ytterbium-doped pulsed fiber laser Blackening Application	145
5.5	Potential Applications for the Blackening Surface	149
5.6	Summary	151
Chapter 6	<i>Conclusions and Recommendations for Future Work</i>	152
6.1	Conclusions	152
6.2	Recommendation for Future Work	156

6.2.1	High peak power YDPFLs with LMA PCF	156
6.2.2	High power UV laser seeded with YDPFL.....	157
Reference.....		159

SUMMARY

Thanks to its plentiful merits, such as high efficiency, vibration proof and maintenance free, high power Ytterbium-doped pulsed fiber lasers (YDPFLs) at 1 μm wavelength region have seen rapid development driven by the broad industrial applications over the past decades. However, there is still a lot of room for innovation and the performance enhancement for the YDPFLs is valuable.

This thesis focuses on the analysis of high power YDPFL at 1 μm wavelength region. Firstly, the theoretical modeling of YDPFLs and design of pulsed pump YDPLs with adjustable pulse duration and pulse repetition rate are investigated. Large amount of stored energy is the basis for high power YDPFLs. The more energy stored in the laser cavity, the more available gain for signal pulse laser injection. At the same time, the more inter-pulse Amplified Spontaneous Emission (ASE). When the ASE is not properly controlled, undesired laser treatment outcomes or self-lasing may occur. Pulsed pump is a superior avenue to address this issue. By modeling and simulation an ytterbium-doped double-clad fiber amplifier (YDFA), the most crucial factors of pulsed pump, pump power (P_p) and pump duration (t_p), have been investigated. For YDPFLs with adjustable pulse duration and pulse repetition rate, I proposed a new pulsed pump method. By using this pulsed pump scheme, the performance of the YDPFL is improved without additional pump or cost.

Secondly, high average power and high peak power YDPFLs have been constructed and studied. High power YDPFLs have progressed rapidly and been widely utilized for material processing. When laser-material interaction occurs, the energy of the laser pulse whose peak power is higher than the ablation threshold power of the material contributes

to the final desired treatment outcomes. The rest of the laser pulse energy is wasted. In order to characterize this, a new parameter, Usable Pulse Energy Ratio (UPER), is proposed. Through this parameter, whether the workpiece can be laser processed or not, how much the pulse energy is wasted, and the width of Heat-Affected Zone (HAZ) after laser treatment can be perceived qualitatively. Then a high average power YDPFL with output power of 160 W has been designed. The YDPFL operating with four pulse duration (80 ns, 56 ns, 34 ns and 10 ns) has been studied. The optical-to-optical conversion efficiency of $\sim 67\%$ for the main amplifier and the 4σ beam quality (M^2) of 1.7 is obtained. The limiting factors for high power YDPFLs (such as ASE, Stimulated Raman Scattering (SRS) and Stimulated Brillouin Scattering (SBS)) are cautiously studied and addressed. A high peak power YDPFL with adjustable pulse duration from 350 ps to hundreds of ns seeded by an superluminescent light emitting diode (SLED) is also demonstrated. The monolithic YDPFL is constructed with MOPA configuration which consists of three cascade amplifiers and the 350 ps laser pulses are generated through gain switch.

Finally, laser applications can not only verify the design of the laser, but also provide the design requirements for the laser. Instead of using expensive and bulky ultra-short lasers, high power nanosecond YDPFL is applied to the blackening of a bulk Al alloy substrate with an alumina surface application. The laser induced porous nanostructures/microstructure (NSs/MSs) layer is formed and located beneath the alumina surface of the BSBs. This is the first time to reveal the porous NSs/MSs formed beneath the alumina surface by a nanosecond YDPFL to the best of our knowledge and the NSs/MSs layer is suggested to be responsible for the structural color. From the application

point of view, the properties of the output laser of an YDPFL and the blackening effect are directly related. This in turn emphasizes the strong bond between the application and the laser design.

LIST OF FIGURES

1. Fig. 2-1. Progress of the average output power of diffraction limited or near-diffraction limited fiber laser since 1989 for continuous and pulse laser [7].
2. Fig. 2-2. Fiber laser performances for (a) nanosecond pulse, (b) picosecond and femtosecond pulse [17].
3. Fig. 2-3. Schematic illustration of rare earth-doped double cladding silica glass fiber [7].
4. Fig. 2-4. Different shapes of cross-section for DCF: Circular, Offset and Rectangular [17].
5. Fig. 2-5. Absorption efficiency versus core diameter at 12 μm , 20 μm and 30 μm for a) circular, b) offset and rectangular cross-section shape [33].
6. Fig. 2-6. (a) Energy level structure of the Ytterbium ions in the silicate glass. (b) Absorption (dotted) and emission (solid) cross-sections [47].
7. Fig. 2-7. Cross-sections of absorption and emission in phosphosilicate and aluminosilicate YDF. Data is from Coractive Inc.
8. Fig. 2-8. Power scale advances for fiber laser with diffraction limited or near-diffraction limited beam quality since 1996 to 2011 [54].
9. Fig. 2-9. Limiting factors for high power YDPFLs.
10. Fig. 2-10. Schematic illustration of the energy diagram of SRS from quantum-mechanical viewpoint [64].
11. Fig. 2-11. (Left) Cross-section view of a standard optical fiber with 9 μm fiber core formed using two bulk materials. It is single-mode in the infrared and guides several modes at visible wavelengths. (Middle) an index-guiding PCF with 5 μm core diameter. It guides light in a single mode over the entire optical spectrum range. (Right) a hollow core bandgap PCF with 7 μm core diameter. It guides only over a limited range of wavelengths in the infrared that correspond to the bandgap of the cladding material [115].
12. Fig. 2-12. Part of applications by high power ns YDPFLs (Images are from JPT Inc.).
13. Fig. 3-1. Marking results on ink paper with an YDPFL (Images are from JPT Inc.). (Left) Residual energy stored in the cavity causes the unwanted tail. (Right) Marking result without unwanted tail.
14. Fig. 3-2. The YDDC fiber amplifier configuration with backward pulsed pump scheme (ISO: Isolator, PC: Pump combiner).
15. Fig. 3-3. Upper level population (N_2) along the gain fiber for several pump durations at 20 W pump power.
16. Fig. 3-4. (a) The pulse energy, (b) efficiency and (c) total upper level population in the gain fiber with pump duration from 50 μs to 1500 μs at pump power of 10 W, 20 W and 30 W.

17. Fig. 3-5. (a) Forward and (b) backward ASE power vs. pump duration at 10 W, 20 W and 30 W pump power.
18. Fig. 3-6. At different t_p , (a) Total stored energy in the DCF, (b) Pulse energy and efficiency, (c) The N_2 distribution along the fiber, and (d) Forward and backward ASE.
19. Fig. 3-7. Dependence of the final output pulse energy and efficiency on the seed pulse energy (by changing the peak power of the seed pulse) for $t_p = 400 \mu s$ (a) and $t_p = 600 \mu s$ (b) respectively. (c) dependence of the output pulse energy and efficiency on the seed pulse energy (by changing the seed pulse duration but keeping the peak power constant) at $t_p = 600 \mu s$.
20. Fig. 3-8. (a) Relationship of the average output power of the laser with the pulse repetition rate (f). (b) The pump power maintains at the maximal reachable pump power level when f is equal to or larger than f_t . (c) The pump power is reduced and keeps at the CW pump scheme when f is less than f_t . (d) The pulsed pump scheme when the pulse repetition rate (f) is less than f_t .
21. Fig. 3-9. Structure of the MOPA YDPFL. LD: laser diode. FBG: fiber Bragg grating, ISO: isolator, OC: optical coupler, CT: collimator, P: pump power level.
22. Fig. 3-10. Relationship of the seed laser and the pulsed pump.
23. Fig. 3-11. When the seed laser is at the front (P1), middle (P2) and end (P3) positions of the pulsed pump, the optical spectrum of the inter-pulse ASE measured from Tap1 after using an AOM with $4 \mu s$ time window to filter out the reflection of the pulse laser.
24. Fig. 3-12. The YDPFL is working with 130 ns pulse duration and the f_t of 25 kHz, (a) At 10 kHz pulse repetition rate, the optical spectra measured from tap1 (the black and red curves are for the CW and pulsed pump respectively) and final output (the blue and dark cyan curves are for the CW and pulsed pump respectively). (b) The efficiency difference for pulsed and CW pump schemes for several pulse repetition rates less than f_t .
25. Fig. 3-13. When the YDPFL is working with 130 ns pulse width and 10 kHz pulse repetition rate under the pulsed and CW pumping schemes, the optical spectra measured at Tap2 (a), final output (b) and Tap1 (c) with an AOM to filter out the pulse laser.
26. Fig. 3-14. (a) Optical spectra of the forward ASE after pre-amplifier stage by tuning the P_p from 1.36 W to 1.55 W after the pre-amplifier stage. Without pump current for main amplifier stage, the output ASE power injected to the main amplifier from the pre-amplifier stage increases from 4.24 mW to 5.91 mW. (b) Optical spectra monitored at Tap1.
27. Fig. 3-15. Optical spectra of the Seed and Pre-amplifier stage for the 20-ns pulse.
28. Fig. 3-16. The YDPFL is working with 20 ns pulse width under CW and pulsed pump schemes. (a) The optical spectra from tap1 (the black and red curves are for the CW and pulsed pump respectively) and final output (the blue and dark cyan curves are for the CW and

- pulsed pump respectively) when the laser system is working with 20 kHz pulse repetition rate. (b) Efficiency difference for the two pumping schemes.
29. Fig. 3-17. Pulse shapes of 130 ns pulses. (a) The seed pulse (black) and after pre-amplifier stage (red). (b) Pulse shapes of the CW pump (black) and pulsed pump (red) at final output of the YDPFL.
 30. Fig. 3-18. Pulse shapes of 20 ns pulses. a) the seed pulse (black) and after pre-amplifier stage (red). b) Pulse shapes of CW pump (black) and pulsed pump (red) at final output of the YDPFL.
 31. Fig. 3-19. The simulation results of the efficiency improvement for pulsed pump comparing with the CW pump. (a) The YDPFL is working with 130 ns and the pulse repetition rate is less than f_t (25 kHz). (b) The YDPFL is working with 20 ns and the pulse repetition rate is less than f_t (72 kHz).
 32. Fig. 3-20. Reflectance of commonly used metals as a function of wavelength from 200 to 2000nm [131].
 33. Fig. 3-21. The optical spectra measured at Tap1 with different threshold pulse repetition rates when the YDPFL is working at 20 kHz pulse repetition rate and 130 ns pulse duration. The red and black curves are for the spectra of processing material with very low and high reflective surface respectively. (a) The laser is working with 28 kHz threshold pulse repetition rate (f_t). (b) The laser is working with 20 kHz threshold pulse repetition rate (f_t).
 34. Fig. 4-1. The effect of pulse shape on machining with nanosecond lasers [136].
 35. Fig. 4-2. Different pulse shapes with same pulse duration and pulse energy.
 36. Fig. 4-3. Structure of the MOPA fiber laser system (FBG: fiber Bragg grating, ISO: isolator, OC: optical coupler, CT: collimator).
 37. Fig. 4-4. For the rectangular shape of seed laser, pulse shape of the seed laser (a), after the pre-amplifier stage (b) and main amplifier stage (c) at 10%, 30%, 50%, 80% and 100% output power scale.
 38. Fig. 4-5. The pulse shapes of the seed laser. (a) Rectangular shape, (b) triangular shape, (c) RWTT shape.
 39. Fig. 4-6. Pulse shapes of the laser with (a) rectangular, (b) triangular, (c) RWTT seed pulse shapes at final output with 20.3 W output power and 35 kHz pulse repetition rate.
 40. Fig. 4-7. UPER at different ablation threshold power for the YDPFL with rectangular, triangular and rectangle-with-triangular-top shapes.
 41. Fig. 4-8. Optical spectra measured at the final output (a) and Tap1 (b) for the laser with three different seed pulse shapes.
 42. Fig. 4-9. SBS spike in a pulse train.

43. Fig. 4-10. (a) The frequency components of the rectangular and Gaussian shape laser pulses. (b) The relationship between rising time and SBS threshold.
44. Fig. 4-11. The pulse shapes of the laser from the seed (yellow), after the pre-amplifier (cyan) and main amplifier (purple), and at Tap1 (green). The images in the left and right are for the YDPFL operating at the moment without and with SBS spike, respectively.
45. Fig. 4-12. Experimental setup of a nanosecond MOPA pulse fiber laser. SLED: superluminescent light emitting diode, ISO: isolator, OC: optical coupler, MFA: mode field adapter, CB: combiner, CL: collimator, F1: splicing point 1, F2: splicing point 2.
46. Fig. 4-13. The optical spectra of the SLED seed diode when operating at different pulse duration and pulse repetition rate.
47. Fig. 4-14. The pulse shapes (a) and the optical spectra (b) of the seed laser of the YDPFL.
48. Fig. 4-15. The pulse shape (a) and the optical spectra (b) of the pre-amplifier stage of the YDPFL.
49. Fig. 4-16. (a) The peak power of the YDPFL pulse with different seed pulse duration. (b) UPERs at different threshold with several different seed laser pulse durations.
50. Fig. 4-17. The pulse shape of the seed and final output with triangular (a) and RWTT seed pulse shape (b). (c) UPERs for the YDPFLs with triangular and RWTT seed pulse shapes at different threshold.
51. Fig. 4-18. (a) The optical spectra of the 80-ns final output laser pulses at different output power. (b) The optical spectra of the final output laser pulses at different pulse duration and ~ 160 W average output power.
52. Fig. 4-19. The pulse shapes (a) and the optical spectra (b) monitored at the Tap3 of the YDPFL.
53. Fig. 4-20. M^2 test result of the YDPFL.
54. Fig. 4-21. The Optical-to-optical conversion efficiency for the main amplifier of the YDPFL.
55. Fig. 4-22. The waveform of the 80-ns seed pulse (yellow), driving current for the pump LD of pre-amplifier (cyan) and main amplifier (purple) when the YDPFL is operating at 2 kHz (a), 10 kHz (b), 30 kHz (c), 70 kHz (d), 110 kHz (e) and 150 kHz (f) with f_s of 110 kHz.
56. Fig. 4-23. Pulse shape (a) and optical spectra (b) of the 80-ns final output laser at several different pulse repetition rates.
57. Fig. 4-24. (Left) The output laser of the YDPFL irradiates at the FC connector of the AOM with 10 μ s open window for distinguishing the ASE and signal. (Right) The optical spectra of the laser signal and ASE.
58. Fig. 4-25. The processing effects of an ultrashort (e.g., femtosecond) pulse laser compared to a long-pulse (e.g., microsecond) laser [149].

59. Fig. 4-26. Structure of the YDPFL in the experiments (ISO: isolator, CB: optical combiner, MFA: mode field adaptor, CL: collimator, F1: splicing fusion point 1).
60. Fig. 4-27. The pulse shape (a) and optical spectrum (b) of the laser pulses with 350 ps and 183 ns pulse duration.
61. Fig. 4-28. The average output power (a) and the optical spectra (b) of the 1st-amplifier stage with different seeding conditions.
62. Fig. 4-29. (a) The average output power of the 2nd-amplifier stage with different pump power. (b) and (c) are the optical spectrum of the 2nd-amplifier stage when the pump power is at 4.28 W and 5.68 W respectively.
63. Fig. 4-30. For the 350 ps laser pulses, optical spectrum at the final output (a) and pulse shapes at the seed and the final output (b).
64. Fig. 4-31. Laser signal proportion and final output laser power with pump powers.
65. Fig. 4-32. Pulse shapes (a) and optical spectra (b) after the 2nd-amplifier and final output of the laser pulses with 183 ns pulse duration.
66. Fig. 4-33. Waveform of pulse trains (a) and one pulse (b) monitored from Tap1 to capture the SBS in 3rd-amplifier stage by oscilloscope via a photo detector.
67. Fig. 5-1. Laser irradiation setup up with a high power nanosecond YDPFL (The pulse duration of the laser is tunable from 2 ns to 200 ns with an average output power of 20 W (Averaging over the entire time span between laser pulses and the pulse duration), the beam quality M^2 (4 σ) equals to 1.3 and pulse repetition rate ranges from 1 kHz to 1 MHz).
68. Fig. 5-2. (a) The image of the square blocks after the laser treatment. The different visual effects are obtained with different pulse energy ranging from 8.23 μ J to 16.47 μ J, with \sim 1.18 μ J increment per step. The pulse repetition rate ranges from 150 kHz to 850 kHz. To have a clear view the photo is taken at a tilted angle. The BSBs are enclosed in red lines. The GSBs are the blocks on the right side to the BSBs. (b) the CIE L^* value for each square block in (a).
69. Fig. 5-3. The CIE L^* value of the sample square blocks vs. laser power density (Accumulated irradiation dose which is calculated by multiplying the laser power and the number of pulses per area).
70. Fig. 5-4. The CIE L^* value and laser power density corresponds to (a) the hatching and (b) scanning speed respectively. The laser system is working with 9.41 μ J pulse energy, 500 kHz pulse repetition rate.
71. Fig. 5-5. The surfaces profiles of the BSB, the GSB and the original sample. The BSB and the GSB are the square blocks taken from Fig. 5-2 with 11.76 μ J pulse energy and 250 kHz and 850 kHz repetition rate respectively.

72. Fig. 5-6. The microscope images of the surfaces profiles of the BSB, the GSB and the original sample. The BSB and the GSB are the square blocks taken from Fig. 5-2 with 11.76 μJ pulse energy and 250 kHz and 850 kHz repetition rate respectively.
73. Fig. 5-7(a) and (b), the SEM images of the cross-sections of the original sample without laser irradiation ((a) amplified by 2 K X, (b) amplified by 20 K X). (c) and (d), the SEM images of the cross-sections of the BSBs ((c) amplified by 4 K X, (d) amplified by 15 K X).
74. Fig. 5-8. The SEM images of the surface of GSBs.
75. Fig. 5-9 The reflectance of the original sample without laser processing, the BSB and the GSB. The BSB and GSB are the square blocks chosen from Fig. 6-1(a) with 11.76 μJ pulse energy, 250 kHz and 850 kHz repetition rate respectively.
76. Fig. 5-10. (a) The BSB, original surface of the plate without laser treatment, and the GSB which is formed above a BSB. (b) The GSB and BSB are co-existent after laser treatment.
77. Fig. 5-11. The surface profile of the plate without laser treatment.
78. Fig. 5-12. The possible scenarios that may affect the blackening effect (the drawing is not in scale), (a) the thickness of the alumina layer is not consistent and it varies from 6 μm to 10 μm . (b) the thickness of the alumina layer is consistent. However, the surface of the aluminum substrate is not smooth which causes the inconsistent alumina surface.
79. Fig. 5-13. CIE L^* value with the offset between the plate surface and the focal position of the laser system.
80. Fig. 5-14. The structure of the surface absorber (This picture is from the catalog of OPHIR Inc.).

LIST OF TABLES

1. Table 3-1. Part of the parameters used in the simulations.
2. Table 3-2. Different sets of P_p and t_p combinations.
3. Table 4-1. The statistics of the SBS spikes captured by the oscilloscope in the experiments within 5 minutes.
4. Table 4-2. Average output power at several pulse durations with different pulse repetition rate.

LIST OF ACRONYMS AND SYMBOLS

AOM: Acousto-Optic Modulator	NS: Nanostructure
ASE: Amplified Spontaneous Emission	OC: Optical Coupler
BSB: Black Square Block	OSA: Optical Spectrum Analyzer
CIE: International Commission on Illumination	OSC: Oscilloscope
CPLD: Complex Programmable Logic Device	PCF: Photonic Crystal Fiber
CT: Collimator.	PD: Photo Detector
CW: Continuous Wave	ps: Picosecond
DC: Duty Cycle	RWTT: Rectangle-With-Triangular-Top
DCF: Double Cladding Fiber	SBS: Stimulated Brillouin Scattering
DFB: Distributed Feedback Laser Diode	SEM: Scanning Electron Microscope
FBG: Fiber Bragg Grating	SLED: Superluminescent Light Emitting Diode
FI: Faraday isolator	SOA: Semiconductor Optical Amplifier
FP: Fabry-Parot	SPM: Self-phase Modulation
fs: femtosecond	SRS: Stimulated Raman Scattering
FWHM: Full Width Half Maximum	TEC: Thermal Electrical Control
GSB: Gray Square Block	UPER: Usable Pulse Energy Ratio
HAZ: Heat-Affected Zone	UV: Ultraviolet
IR: Infrared	YDDC: Ytterbium-doped Double-clad
ISO: Isolator	YDF: Ytterbium-doped Double-clad Fiber
ITO: Indium Tin Oxide	YDFA: Ytterbium-doped Double-clad Fiber Amplifier
LD: Laser Diode	YDFL: Ytterbium-doped Double-clad Fiber Laser
LMA: Large Mode Area	YDPFL: Ytterbium-Doped Pulsed Fiber Laser
MOPA: Master Oscillator Power Amplifier	
MOSFET: Metal-Oxide-Semiconductor Field-Effect Transistors	
MS: Microstructure	
MUP: Material under Processing	
NA: Numerical Aperture	
NIR: Near-Infrared	

Chapter 1 INTRODUCTION

1.1 BACKGROUND AND MOTIVATION

Laser, associated with the high brightness, small divergence and non-contact process, has been widely applied in lots of fields which include industry, research, medical treatment and military etc., ever since the invention. Fiber, which is invented for the telecom communication applications, is also proposed to be a suitable waveguide for high power laser [1,2]. When being doped with rare earth ions, it becomes gain fiber from a passive component which can be utilized for not only guiding light, but also amplification light. When the laser and gain fiber come together, we “obtain” fiber laser. By using the fiber as gain media and light waveguide, the high optical-to-optical efficiency, promising heat dissipation resulting from the large surface area, and vibration proof induced from the monolithic configuration etc., are achieved. For a 1 μm wavelength fiber laser doped with Yb^{3+} ions, the laser firstly has high quantum efficiency due to the relatively small wavelength difference between the pump and the signal laser and this is crucial for high power fiber lasers design. Secondly, Yb^{3+} ions possess a wide absorption and emission spectra and this renders a greater range of options of the pump laser wavelength. The wavelength of the output laser can also be set according to design requirements.

In 1961 E. Snitzer proposed a laser with an optical fiber cavity [3] and in 1964, Koester and Snitzer utilized a 1-meter-length fiber with a neodymium-doped core in a laser amplifier [4]. The fiber laser at 1 μm wavelength has progressed rapidly especially after the concept of double-cladding-fiber and multi-mode high power pump became available. YDPFLs have drawn the interest of a large number of researchers during the past two

decades. Recently, higher peak power, larger pulse energy, novel laser cavity configurations and better efficiency etc. are still among the popular research topics.

From the market data from Strategies Unlimited [5], fiber lasers have emerged as the most widely utilized industrial lasers, accounting for 57% of the total revenue of all types of lasers in 2016. The revenue of it has the fastest growth in the past two years which is 16% for 2015 and 11% for 2016. When coming to the marking/engraving applications where high power YDPFLs are mostly utilized, the YDPFL has the dominant share of 73% in 2016.

When YDPFL is used for material processing, it is essentially a laser-material interaction. The properties of the laser pulses strongly associate with the treatment effects. After laser treatment, the unique features of the surface morphology that allow modification of the mechanical, optical, chemical, tribological and other properties of the surface attract the attention of researchers in many fields. The full explanation on the formation dynamics by laser pulses is still an unfinished task due to the complicated laser-material interaction.

Due to the many merits and wide implementation of high power YDPFLs, the performance enhancement for the lasers is valuable, and there is still a lot of room for innovation. By exploring and investigating the laser-material interaction, a better understanding of the high power YDPFL is achieved. This understanding, in turn, is critical to the design of high power YDPFLs with better performance.

This is my motivation to analyze high power pulsed fiber laser at 1 μm wavelength. The research focuses on high power YDPFLs and furthermore, the laser-material interaction by the lasers.

1.2 OBJECTIVES

As described in the Background and Motivation Section, YDPFLs possess a number of superiorities, which are expected to play a key role in many applications. The objectives of this work are to analyze and improve the performance of high power YDPFLs. At the same time, to study the mechanism behind the laser-material interactions by the high power YDPFLs.

1.3 MAJOR CONTRIBUTIONS

The original contributions in this thesis are listed as follows:

- I propose a pulsed pump design for YDPFLs with adjustable pulse repetition rate and pulse duration. By using such a pulsed pump scheme, the pump power (P_P) is kept at the maximal reachable pump power level or a fixed level, and the pump duration (t_p) for each seed pulse is modulated according to the pulse duration. The experimental results show the efficiency is improved by $\sim 10\%$ at 2 kHz and $\sim 6\%$ at 5 kHz for long (130 ns) and short (20 ns) pulse duration respectively comparing to the CW pump scheme. There is the same trend obtained from both the numerical simulation and experimental results.
- I propose a new parameter, Usable Pulse Energy Ratio (UPER), to characterize the laser pulse of a nanosecond high power YDPFL by considering the laser-material interaction. UPER is defined as the ratio of the pulse energy of the part of the nanosecond laser pulse whose peak power is higher than the predefined ablation threshold power to the maximum reachable pulse energy. With this parameter, we qualitatively perceive whether the workpiece can be laser processed or not, how

much pulse energy is wasted, and how wide the heat affected zone (HAZ) is after laser treatment. High power YDPFL with pulse shaping has been analyzed with UPER.

- I design a novel high average power MOPA YDPFL with adjustable pulse duration and pulse repetition rate. The average output power reaches 160 W. To mitigate the SRS component and enhance the pulse energy, a triangular seed pulse shape is adopted for the laser. The laser with pulse energy of 1.45 mJ has been achieved with 80 ns seed pulse, and the power in the 1st Raman peak at ~ 1115 nm is at -20 dB compared to the center wavelength of the signal laser. In order to address SBS, an SLED seed source with 3 dB optical spectrum of 20 nm, has been utilized to produce the seed pulses. The inter-pulse ASE has been suppressed through the proposed pulsed pump scheme in this thesis. The optical-to-optical conversion efficiency of $\sim 67\%$ for the main amplifier and the 4σ beam quality (M^2) of 1.7 is obtained.
- I design a novel high peak power YDPFL with adjustable pulse duration in the range of 350 ps to hundreds of ns seeded by an SLED. Due to the ~ 20 nm optical spectrum of the SLED, SBS is avoided for this laser. The 350 ps laser pulse generated through gain-switching technique reaches the peak power of 275 kW and pulse energy of 92 μ J after amplification. The ASE component of the laser is investigated and the laser proportion is $\sim 53\%$. The pulsed pump technique proposed in this thesis is implemented to the laser to suppress inter-pulse ASE for laser operating at pulse repetition rate less than threshold pulse repetition rate. For the laser with 183 ns seed pulse duration, pulse energy of 3.2 mJ and peak power

of 137 kW is achieved. The beam quality ($4\sigma M^2$) of this laser is 2.7 and 2.8 for the X and Y directions, respectively.

- I reveal the high power nanosecond YDPFL induced porous nanostructures/microstructures (NS/MS) layer beneath the alumina surface. The NS/MS layer is suggested to be responsible for the structural black color. The black square blocks (BSBs) and the gray square blocks (GSBs) formed after laser treatment are characterized qualitatively and quantitatively. The reflectance for the BSB is much lower than the original sample from 280 nm to 2500 nm and the reflectance is considerably uniform in visible light range. The feasibility of this application is studied and proved.

1.4 OUTLINE OF THE THESIS

In this thesis, the analysis of high power YDPFL at 1 μm wavelength is focused. An introduction of high power YDPFL has been presented in Chapter 2. In Section 2.1, the history and current state of fiber lasers are reviewed. Due to the superiority of fiber lasers and the demand from industry, the power scale of fiber lasers has developed rapidly since the invention of double-clad fiber (DCF) and high power multimode pump diodes. In Section 2.2, the fundamental elements of YDPFLs have been introduced, including DCF, Ytterbium-doped fiber, and limiting factors for pulsed fiber laser at 1 μm wavelength. For DCF, the influence of fiber geometry on the pump absorption efficiency is summarized. For ytterbium ions fiber, the energy level, absorption and emission spectra are reviewed. Aluminosilicate (Al) and phosphosilicate (P) glasses are also compared. In Section 2.2.3, the limiting factors such as thermal damage, self focusing, SPM, gain saturation, SBS,

SRS and mode instabilities are described. The comparison between the step-index LMA fiber and photonic crystal LMA fiber for high power fiber laser is performed in Section 2.2.4. A few applications of the YDPFLs have been shown in Section 2.3.

Large amount of stored energy is the basis for high power YDPFLs. However, if the ASE is not properly controlled, undesired laser treatment outcomes or self-lasing may occur. Pulse pump is an effective avenue of suppressing ASE between laser pulses of high power YDPFL, especially when the laser operates at a low pulse repetition rate. In Chapter 3, I focus on the pulsed pump design of high power YDPFLs. For pulsed pump design, the most important factors to be determined are the pump power and pump duration. In Section 3.2, the pulsed pump YDFA is numerically studied and the relationship between the pulse energy, efficiency and ASE with pump power and duration is investigated. In Section 3.3, the pulsed pump design for YDPFLs with tunable pulse repetition rate and pulse duration is studied. By using this pump scheme, the P_p is kept at the maximal reachable pump power level or a fixed level. The t_p for each seed pulse is modulated according to the pulse duration. When the laser is operating with pulse repetition rate less than the threshold pulse repetition rate (f_t), the efficiency is improved by $\sim 10\%$ at 2 kHz and $\sim 6\%$ at 5 kHz for laser pulses with long (130 ns) and short (20 ns) pulse duration respectively comparing with CW pump scheme. Numerical simulation results indicate the same trend as that of the experiments.

I dedicate Chapter 4 to the high power YDPFL design. In Section 4.2, a new parameter, UPER, to characterize the laser pulse of high power YDPFLs by considering the laser-material interaction, is proposed. The gain saturation effect for a high power YDPFL with three seed pulse shapes, rectangles, triangles and rectangle-with-triangular-top (RWTT)

shapes have been experimentally investigated. The UPER of the laser with triangular and RWTT is lower when the ablation threshold power is higher than 3 kW. However, it grows to 70.3% for a laser possessing a triangular seed pulse shape and is about 5% higher than that of the rectangular seed pulse shape at a lower ablation threshold power 2 kW. The nonlinear effects (SBS and SRS) associated with the laser of these seed pulse shapes have been studied. SBS spikes are frequently captured for the laser with triangular seed pulse shape. However, for the seed laser with RWTT shape, no SBS has been found in the experiment. In Section 4.3, a high average power YDPFL with output power of 160 W has been constructed and investigated. The properties of the output pulsed laser with four different pulse durations (10 ns, 34 ns, 56 ns and 80 ns) have been analyzed. The ASE, SBS and SRS are cautiously addressed during the laser design. The pulse repetition rate can be varied from one shot to 1 MHz and the 4σ beam quality is ~ 1.7 for both X and Y direction. The optical to optical power conversion efficiency reaches $\sim 67\%$. YDPFLs with wide adjustable pulse duration are appealing and valuable for industrial applications. In Section 4.4, we demonstrate a novel high peak power MOPA YDPFL with adjustable pulse duration from 350 ps to several hundred ns seeded by an SLED. For the 350 ps laser generated through gain-switching technique, a peak power of 275 kW and pulse energy of 92 μJ is reached after amplification. The laser proportion is $\sim 53\%$ for the final output laser excluding ASE component. For the laser with 183 ns seed pulse duration, the peak power of 137 kW and pulse energy of 3.2 mJ is obtained. The $4\sigma M^2$ is 2.7 and 2.8 for the X and Y directions, respectively. Due to the ~ 20 nm optical spectrum of the SLED, SBS is avoided. The pulsed pump technique proposed in Section 3.3 is implemented to this laser to suppress the inter-pulse ASE at lower pulse repetition rate operation.

In Chapter 5, the application of blackening aluminum alloy with alumina surface is achieved and investigated with a nanosecond YDPFL. The surface blackening effect is quantitatively studied by the CIE L^* value. The surface profile and optical properties of the surface with and without laser treatment are analyzed. The NSs/MSs layer formed under the alumina surface is revealed and considered to be the cause of the structural blackening color. The potential application of ns YDPFL induced blackening has been discussed. And the feasibility of blackening for mass production is studied. From this application, it is recognizable that the duration of the laser pulse, pulse energy, the final output laser beam quality is extremely linked with the processing effects. It illustrates the strong relationship between laser applications and laser design.

Finally, the conclusion of this thesis and the suggestions for future work are presented in Chapter 6.

1.5 PUBLICATIONS AND PATENTS

1.5.1 Publications

1. **M. Liu, et al.**, Pulse shape tuning for 1064 nm nanosecond MOPA fiber laser, *Procedia Engineering*, 140: pp. 123-126 (2016).
2. **M. Liu, et al.**, 1 micrometer wavelength pulse fiber laser assisted black marking on the surface of aluminum oxide, *Optoelectronics Global Conference (OGC)*, IEEE, pp. 1-2, (2015).
3. **M. Liu, et al.**, Nanosecond Pulse Fiber Laser Blackening of Aluminum Alloy with Alumina Surface. *IEEE Photonics Technology Letters*, 28(23), pp. 2701-2704 (2016).
4. **M. Liu, et al.**, Pulsed pump for Pulse Duration Tunable Nanosecond Ytterbium-Doped Fiber Laser. *IEEE Photonics Technology Letters*, 28(24), pp. 2842-2845

(2016).

5. **M. Liu, et al.**, Dynamics of nanosecond pulsed pump ytterbium-doped double-clad fiber amplifier. *Optics Communications*, 403 pp. 325-329 (2017).
6. **M. Liu, et al.**, 160 W Nanosecond Ytterbium-doped Pulsed Fiber Laser. *CLEO-PR/OECC/PGC*, accepted (2017).

1.5.2 Patents

1. **M. Liu, et al.**, A pulsed laser and pulsed laser marking system, CN102892585A, WO2013120248A1, 2015.
2. **M. Liu, et al.**, Pumping modulation mode of pulsed laser, CN105140770 A, 2015.

Chapter 2 BACKGROUND INFORMATION AND LITERATURE REVIEW

2.1 HISTORY AND CURRENT STATUS OF PULSED FIBER LASER WITH 1 MICROMETER WAVELENGTH

Fiber lasers are lasers in which the waveguide is an optical fiber and the gain medium is doped in the fiber core. Optical fibers possessing the superiority of high-capacity channels and low-attenuation waveguides have been extensively studied and practiced in the world as suitable transmission media for light waveguide and optical communication [1,2]. However, the utilization of optical fibers in lasers is even longer than in the field of telecommunications. The first fiber laser was invented one year after the laser was born. In 1961 E. Snitzer proposed a laser with an optical fiber cavity [3] and in 1964, Koester and Snitzer utilized a 1-meter-length fiber with a neodymium-doped core in a laser amplifier [4].

Lasers benefit from the utilization of optical fiber as gain media. First, the area-to-effective volume ratio of the fiber geometry is large, resulting in excellent heat dissipation, as this is essential for generating high power lasers [6]. Second, the waveguide structure of the fiber is stable over long distances, which allows a large gain to be obtained because of the long interaction path between the signal and the gain medium [7]. The high gain also allows a simple laser cavity, such as the main oscillator power amplifier (MOPA), which benefits from less nonlinearity. Because of this waveguide structure, the basic mode is almost unaffected by the thermal lens effect [8]. Third, the laser cavity can be made up of FBG as reflection mirrors, and FBG can be generated by a UV excimer laser or

a picosecond laser in a fiber core. Along with the entire system joint by fiber splicing without free space component, these characters make fiber laser free from mirror alignment, free from mirror surface cleaning, free from maintenance and vibration proof [9]. Finally, when compared to other types of lasers, fiber lasers have higher optical to optical conversion efficiency, especially for ytterbium-doped fiber lasers with wavelengths of ~ 1064 nm.

Fiber lasers have attracted intense interest from researchers all over the world, even recently [10-16], because of the special properties associated with optical fibers. Continuous-wave (CW) and pulsed fiber lasers were developed rapidly, especially after the double-clad pump and high power multimode diodes were introduced in the late 1980s. Fig. 2-1 summarizes the power advance of CW and pulsed fiber lasers with diffraction-limited or nearly diffraction-limited lasers over the past two and a half decades [7]. The green diamond presents a 20 KW power scale fiber laser in 2013 but the beam quality needs to be specified.

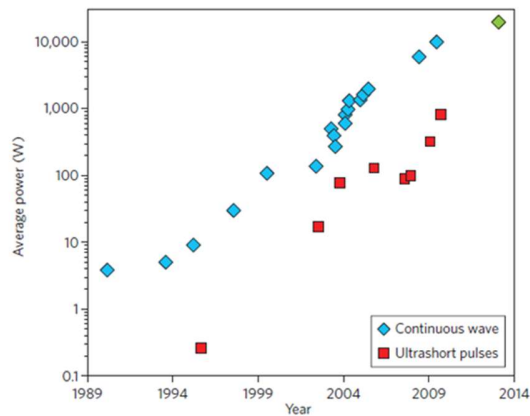


Fig. 2-1. Progress of the average output power of diffraction limited or near-diffraction limited fiber laser since 1989 for continuous and pulse laser [7].

In addition to the high average power of CW fiber lasers, another attraction

characteristic of fiber lasers is the diversity of temporal output characteristics from CW to attosecond pulses. Fig. 2-2 illustrates the progress of peak power and pulse energy for nanosecond to femtosecond pulsed fiber lasers [17].

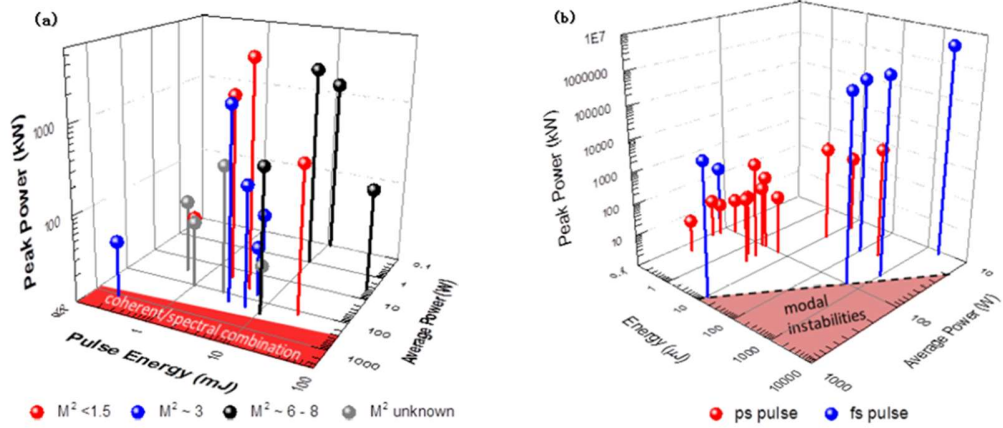


Fig. 2-2. Fiber laser performances for (a) nanosecond pulse, (b) picosecond and femtosecond pulse [17].

Many technologies such as Q-Switching, external modulation, directly modulated, gain-switching, and mode-locked etc., [18-23] can be used to generate pulse trains with different temporal duration from ns to ultrashort (fs) pulse with 1 μm wavelength. The state-of-the-art peak power for ns pulse fiber laser is single mode, 1 ns pulse duration with ~ 4.5 MW peak power (4.3 mJ pulse energy, and 42 W for average power) produced by a MOPA laser system, a 100 μm PCF fiber used for final amplifier stage [24]. For fs pulsed fiber laser, the peak power reaches GW [25, 26]. However, as the output power increases, there is a new constraint called mode instabilities, indicated by the black dash line in Fig. 2-2b [27]. The reasons behind it have not been fully understood.

2.2 FUNDAMENTAL ELEMENTS FOR PULSED FIBER LASER

2.2.1 Double cladding fiber (DCF)

In view of the tiny diameter of the fiber core (typically a few micrometers with a small reception angle for single mode operation), only single-mode diode pump laser can be used for effectively pump. This limits the output power scale since the power of the single mode diode is relatively low compared to a multimode diode laser and the extraction power from the laser cavity is associated with the pump power. For these fiber lasers, the final output power level is normally tens of milliwatts [28]. After the concept of double cladding fiber was demonstrated by Snitzer and Po [29, 30], the output power scale of the continuous wave fiber lasers increases dramatically. Fig. 2-3 shows the schematic of a rare earth-doped DCF.

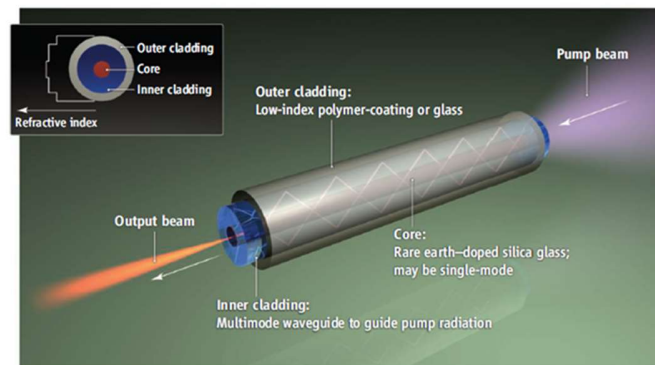


Fig. 2-3. Schematic illustration of rare earth-doped double cladding silica glass fiber [7].

With a DCF configuration, multimode pump light with large numerical aperture (NA) and high power can be emitted and guided in a multimode large-size inner cladding and absorbed by rare earth doped ions in the fiber core. The signal laser is constrained in a tiny single-mode core and is amplified as it travels along the fiber [31].

In order to improve pump light absorption efficiency, non-circular cladding geometries

or offsets are used to increase the overlap of the pump light and the doped core by mode mixing [32]. Fig. 2-4 shows the different types of cross-sections of rare earth doped DCF.

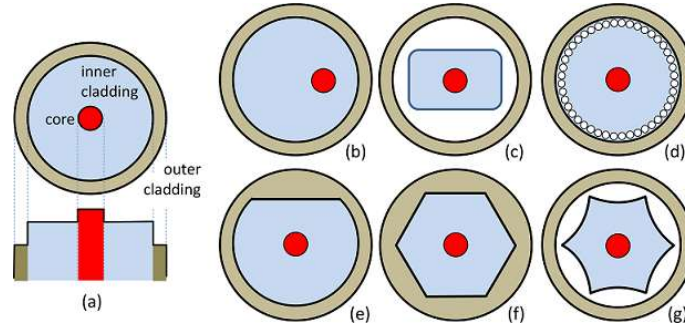


Fig. 2-4. Different shapes of cross-section for DCF: Circular, Offset and Rectangular [17].

According to Liu and Ueda [33], the pump light absorption efficiency of the offset or rectangular cross-sectional shape is much higher than that of the circular shape. As for a double-clad fiber with a symmetric structure, the skewed ray is more likely to propagate at locations away from the center region, which results in low absorption efficiency. When a small surface element on the entrance surface of the fiber is pumped by many different pumping modes and the projections of launching pump on the entrance plane have the uniform distribution, the absorption efficiencies of the three different DCF inner cladding shapes are shown in Fig. 2-5 [33]. The inner cladding has a size of $400\ \mu\text{m}$ and a doping concentration of 0.59 wt%. For circular shape, the absorption efficiency for $\sim 10\ \text{m}$ fiber is less than 25%, and the increase is minuscule even under the longer fiber length. However, when an appropriate fiber length is selected for an optical fiber having an offset or rectangular cladding structure, the absorption efficiency is increased to 100%. Other cladding geometries in Fig. 2-4, such as D-shaped, Octagonal (or Hexagonal), and air-clad fiber structure (PCF) [34] etc. can be selected to achieve high absorption efficiency for active DCF.

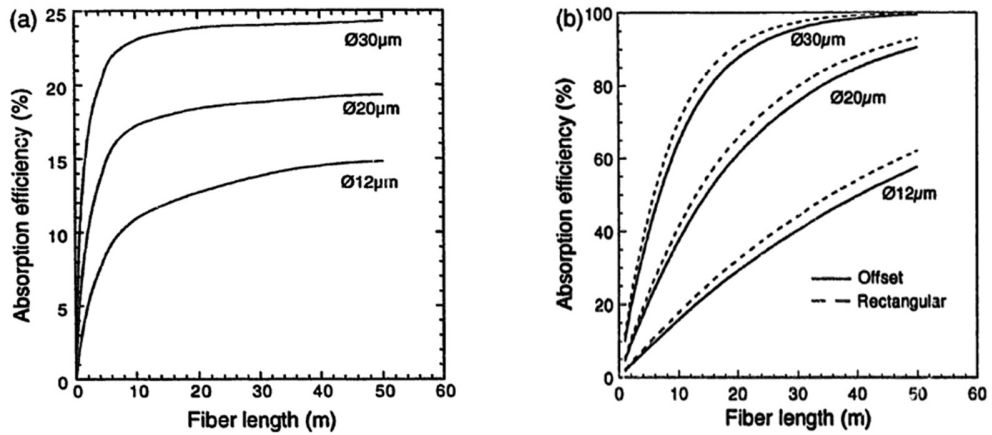


Fig. 2-5. Absorption efficiency versus core diameter at 12 μm , 20 μm and 30 μm for a) circular, b) offset and rectangular cross-section shape [33].

The near-diffraction limit average power developed rapidly from 1988 to 2008, from a few watts in the early 1990s to 1 kW in 2002 and to 10 kW in 2009 by using the cladding-pump technique with the rare earth-doped DCF fibers [35-39].

2.2.2 Ytterbium (Yb^{3+}) doped fiber

The first Yb-doped silicate glass lasers were made by Etzel et al. in 1962 [40]. However, in the next two decades, the study of the laser diode became fairly quiet due to the lack of suitable pump laser diode for Ytterbium ions. In the 1980s, a pump source with 808 nm was achieved by using an AlGaAs active quantum well and it is a suitable pump source for neodymium doped laser materials [41]. Lasers with Nd-doped materials have been extensively studied and used in research and industrial fields because of their higher efficiency than traditional broadband arc and flash-lamp pump lasers. In the 1990s, with the development of erbium-doped fiber amplifiers (EDFA), the study of 9-xx nm diode pumps advanced rapidly [42]. These led to the development of ytterbium-doped laser materials that require a pump wavelength of 900 nm to 980 nm.

The energy level and cross-sectional structure of ytterbium ions are shown in Fig. 2-6

[43-45]. $^2F_{5/2}$ and $^2F_{7/2}$ are ground and excited states of the manifolds. There are 4 sublevels for $^2F_{7/2}$ level and 3 sub-levels for $^2F_{5/2}$ because the Stark division. The narrow line at 975 nm is the peak A for both emission and absorption, corresponding to transition between energy level (a) and energy level I in the energy level diagram. The other peaks B ~ E in the cross-section also correspond to the transition between the different levels in the $^2F_{5/2}$ and $^2F_{7/2}$ states. The laser action in peak A forms a three level laser system. For the peak D, it is a transition from energy level (e) to energy level (b), (c) and (d). This forms a nearly four-level system as level (c) and (d) is essentially empty. Peak E corresponds to the transition from energy level (f) to $^2F_{7/2}$ and its weakness is associated with the small thermal population in that level [46, 47]. Fig. 2-6b shows a broad band of the absorption spectrum of Yb^{3+} ranging from ~ 850 nm to ~ 1080 nm. It allows for the feasibility of multi-pump or multi-wavelength pump solutions, which in turn contribute to power scaling [17]. Thermal control is a key part of designing high power multi-kilowatt fiber lasers. Due to the broadband absorption spectrum, in-band pumping in the range of ~ 1010 nm to ~ 1020 nm can be achieved to increase quantum efficiency and thereby reduce the amount of heat generated. In addition, a low-cost pump without a thermoelectric control (TEC) controller is feasible due to the broadband absorption spectrum. This results in a simplified design and reduces the overall cost and long-term stability of high power fiber lasers [17]. Broadband emission spectrum makes it feasible to implement wavelength tunable lasers and broadband ASE laser sources.

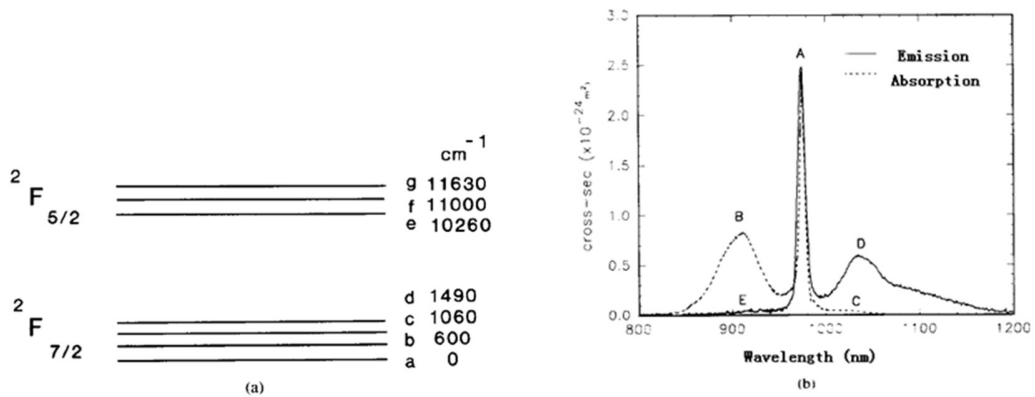


Fig. 2-6. (a) Energy level structure of the Ytterbium ions in the silicate glass. (b) Absorption (dotted) and emission (solid) cross-sections [47].

Fig. 2-7 show emission and absorption cross sections of aluminosilicate (Al) and phosphosilicate (P) YDF (data from Coractive Inc.). The absorption and emission cross sections of the phosphosilicate glass are lower than the absorption and emission cross sections of the aluminosilicate glass. However, the absorption cross-section curve of the phosphosilicate glass from $\sim 910 \text{ nm}$ to $\sim 970 \text{ nm}$ is flatter than that of the aluminosilicate glass, and this feature favors the output laser's stability. Since most commercial low cost high power multimode pump laser diodes are not equipped with an internal TEC for controlling the temperature of the laser diode and the center wavelength of the pump laser is associated with the temperature of the diode. For phosphosilicate glass fibers, due to the flattening of the absorption cross section, the shift of the pump laser wavelength does not give rise to a significant change in the power of the output signal laser. For fiber lasers with a popular MOPA configuration, if the seed signal power fluctuation occurs at the pre-amplifier stage, when the seed laser is insufficient to dissipate much of the energy stored in the next amplifier stage and to keep the ASE at a safe level, this may trigger damage to the laser cavity due to the ASE self-lasing. The phosphosilicate glass has a much greater dopant concentration and has no significant clustering effect. In addition, the

photo-darkening effect which is one of the main concerns of high power fiber lasers is reduced or even eliminated [17].

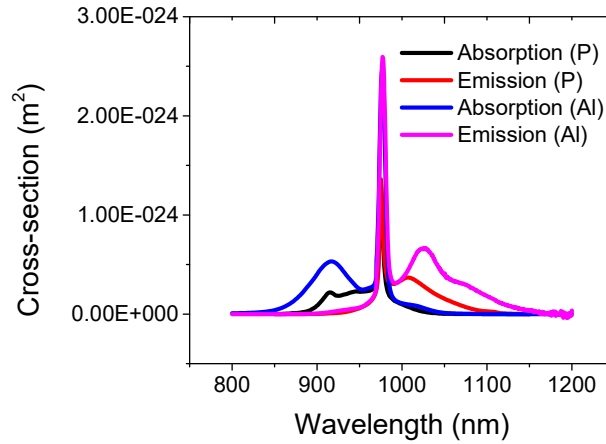


Fig. 2-7. Cross-sections of absorption and emission in phosphosilicate and aluminosilicate YDF. Data is from Coractive Inc.

Comparing with neodymium ions doped in yttrium aluminum garnet crystal (~ 0.3 ms upper-level lifetime), the energy-storage lifetime for ytterbium ions (~ 0.8 ms) is much longer varying in different host fibers [45, 48]. There is no excited state absorption at the pump and laser wavelength because the energy level consists of two manifolds ($^2F_{5/2}$ and $^2F_{7/2}$). The quantum defect is low as a pump of 9-xx nm and lasing of ~ 1064 nm [47]. The quantum efficiency is $\sim 92\%$ (calculated from $980/1064 \times 100\%$) when the wavelength of the pump and signal laser is 980 nm and 1064 nm respectively. Since the wavelength difference between the pump and the laser signal is small, it has a higher quantum efficiency (lower quantum defect) when compared with the other type lasers, such as erbium-doped laser at 1550 nm central wavelength with 9-xx nm pump. Small energy defects lead to less heat load and nonlinearity, which is critical for high power fiber lasers. Finally, ytterbium has a wide emission and absorption spectrum, allowing a wide range of pump and laser wavelength options.

YDFL beneficiary from the merits of ytterbium-ions and the development of the theory of cladding pump has made great progress [49-53]. Since the mid-1990s, the power scale with diffraction limited or near-diffraction limited beam quality for YDF laser has increased by about 2 dB per year (Fig. 2-8). In addition, since 1999, all the record-breaking output power of fiber lasers has been achieved from Yb-doped fiber lasers [54].

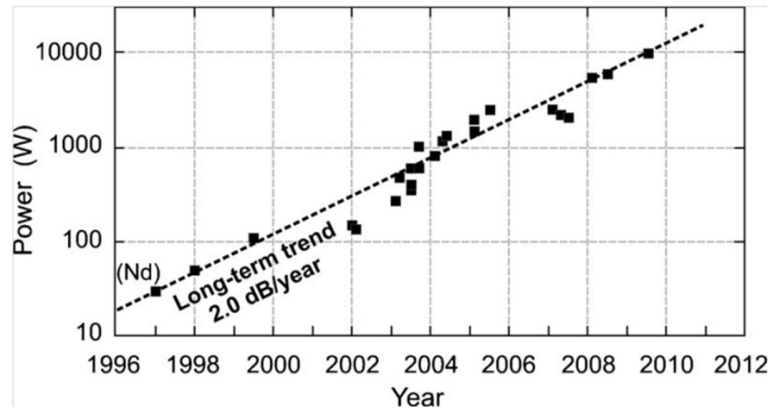


Fig. 2-8. Power scale advances for fiber laser with diffraction limited or near-diffraction limited beam quality since 1996 to 2011 [54].

2.2.3 Limiting factors for pulsed fiber laser with 1 μm wavelength

Fiber is the ideal waveguide for lasers, and the geometry of the fiber is the basis for most of its merits, such as promising beam quality, high gain, and superior heat dissipation from large surfaces. However, the tiny core and long cavity length results in high power density in the core which forms a favorable condition for nonlinearities, such as stimulated self-phase modulation (SPM), self-focusing, SBS, and SRS etc. All of these effects not only limit the power scale of fiber lasers, but also cause the instability of the laser cavity. The fundamental performance metrics for pulsed fiber laser is average output power, peak power, pulse energy and pulse duration etc. However, limitations on the performance of pulsed fiber lasers are usually set by pulse energy or peak power [54]. The

main limiting factors for YDPFL are shown below (Fig. 2-9).

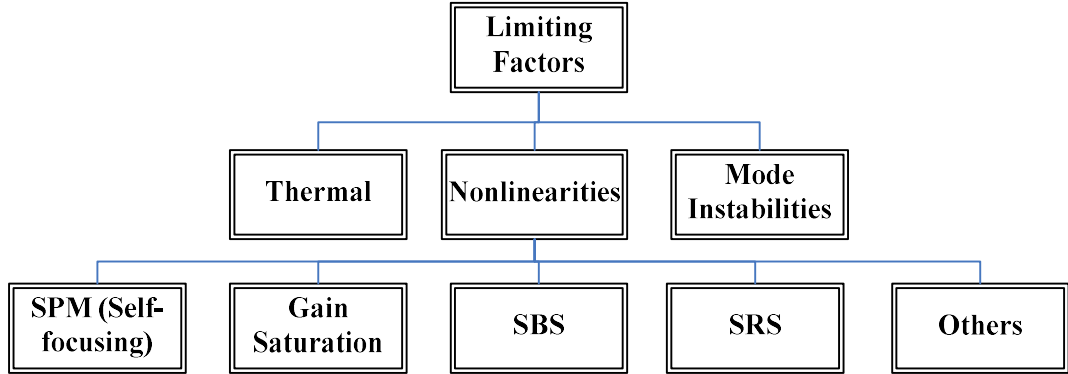


Fig. 2-9. Limiting factors for high power YDPFLs.

2.2.3.1 Thermal damage limitation

Optical damage limit for pulsed fiber laser due to high peak power has been studied by many researchers [55-58]. The damage involves “the heating of conduction band electrons by the incident radiation and transfer of this energy to the lattice. Damage occurs via conventional heat deposition resulting in the melting and boiling of the dielectric material [55]”. For pulse duration from 50 ps to 100 ns at 1.06 μm wavelength, the damage threshold can be estimated by the following equation [54].

$$P_{\max} = I_{th} A_{eff} = X A_{eff} / \sqrt{\tau} \quad (2.1)$$

Where $X = 1.5 \text{ kW ns}^{0.5} / \mu\text{m}^2$, and τ is the pulse duration expressed in nanosecond. A_{eff} is the effective mode area.

When the pulse duration is less than 20 picoseconds, there is not enough time for the electrons to couple to the lattice due to the short duration. The damage mechanism is different from pulses with a pulse duration greater than 50 ps, which is characterized by local ablation [59]. The threshold can be written as equation 2.2 [54].

$$EP_{\max} < 2.25 \text{ mJW} / \mu\text{m}^4 \quad (2.2)$$

Where E is the pulse energy.

2.2.3.2 Self-focusing and Self-phase modulation (SPM)

Due to the nonlinear contribution at high irradiance, the refractive index of the fiber changes and can be written as:

$$n = n_0 + n_2 I \quad (2.3)$$

Where n_0 is the refractive index at low irradiance, n_2 is the nonlinear refractive index also known as Kerr coefficient, and I is the intensity. The nonlinear n_2 leads to the broadening of optical spectrum. This is called self-focusing and is also related to self-phase modulation (SPM) [60].

The critical power for self-focusing is defined by [61]:

$$P_{cr} = a \lambda^2 / (4\pi n_0 n_2) \quad (2.4)$$

Where a is a constant value that is independent from the material property and λ is the signal wavelength in free space. The critical power of self-focusing is about 4 to 5 MW for 50 μm core radius of a straight step-index fiber with 0.06 NA, for smaller fiber core radius, the critical power decreases [62, 63]. SPM plays a crucial role in straight fibers with a core radius of more than 20 μm [63] and it is the temporal analog of self-focusing [64]. The phase shift of the laser pulses traveling along the fiber can be written as [65]:

$$\varphi = n_0 k_0 z + \gamma P(t) z \quad (2.5)$$

Where $n_0 k_0 z$ is the linear phase shift because of signal propagation, and $\gamma = n_2 k_0 / A_{eff}$ represents the nonlinear phase shift. $P(t)$ is the power at each time point and z is the position along fiber core. Pulse shape affects the effect of SPM-induced spectral broadening.

2.2.3.3 Gain Saturation

When propagating through the active fiber core, the signal is amplified due to the gain resulting from the rare earth doped ions in the upper energy levels. However, the signal cannot be infinitely amplified. The gain decreases as the power increases, and eventually there is no excited ion in the metastable level, which can be used to amplify the signal by signal-induced transitions. This is the gain saturation effect [66, 67], which caps the power scale that can be extracted from the laser cavity.

For a CW single frequency YDPFL system, the gain of small signal is [68]:

$$\gamma_0 = \frac{\nu_s}{\nu_p} \left(1 - \frac{\alpha_p}{\alpha}\right) \frac{(1 - e^{-\alpha L})}{L} \frac{P_p^+(0) + P_p^-(L)}{P_{sat}} - N\Gamma_s \sigma_{as} \quad (2.6)$$

Where γ_0 is the small signal gain, ν_s and ν_p are the signal and power frequency respectively, α_p represents the scattering loss at pump frequency, L is the length of the fiber amplifier, $P_p^+(0)$ and $P_p^-(L)$ is the pump power at both fiber end, N represents the doping concentration, Γ_s is the signal power filling factor, σ_{as} denotes cross-section of absorption, and P_{sat} is the saturation power.

The saturation power can be written as follows [68]:

$$P_{sat} = \frac{h\nu_s A}{\Gamma_s (\sigma_{as} + \sigma_{es}) \tau} \quad (2.7)$$

Where h is the Plank's constant and τ represents the spontaneous lifetime. σ_{es} denotes cross-section of emission.

Gain saturation is related to a number of factors, such as the nature of the doped ion, the concentration of ion in the host, the length of the active fiber, the pumping scheme of the amplifier and the pump power etc. In general, a laser system with a shorter gain fiber, a backward pump scheme rather than a co-pump and a higher pump power can mitigate the

gain saturation effect to a certain extent [68].

2.2.3.4 Stimulated Brillouin scattering (SBS)

SBS and SRS are the most encountered nonlinearities for fiber laser. “The process of SBS can be described classically as a nonlinear interaction between the pump and Stokes fields through an acoustic wave [64]”. SBS generates backward-propagating light that is formed by transferring energy from the pumping signal and destabilizes the laser cavity. Due to stress and strong acoustic waves in the fibers, may lead to catastrophic fiber damage [62]. The threshold of SBS can be estimated by the following equation [69], where SBS is the main peak power factor of YDPFL [70].

$$g_B P_{CR} L_{eff} / A_{eff} \approx 21 \quad (2.8)$$

Where g_B is the peak value of the Brillouin gain and P_{CR} is the critical power threshold for SBS. A_{eff} represents the effective core area and L_{eff} is the effective length of fiber and can be calculated by equation (5-4) [64]:

$$L_{eff} = [1 - \exp(-\alpha L)] / \alpha \quad (2.9)$$

Where α is the loss of pump signal propagation in the fiber and L is the fiber length. The frequency shift for SBS can be described as (5-3) [64].

$$\nu_B = \Omega_B / 2\pi = 2n_p \nu_A / \lambda_p \quad (2.10)$$

Where λ_p is the wavelength of the pump signal, n_p is the effective mode index at this wavelength, and ν_A is the velocity of the acoustic wave. For lasers having a wavelength of 1.06 μm , the corresponding SBS frequency shift is ~ 16.244 GHz or ~ 0.088 nm. Due to the minuscule frequency shift and relatively wide bandwidth of the pump signal for the experiments in the following paragraphs, the frequency of the SBS overlaps with the pumping signal and makes it arduous to distinguish the SBS component from the

spectrum. However, the SBS peak can be examined by the oscilloscope through the photo-detector.

Several methods have been proposed to mitigate SBS by researchers [71-74]. First, the SBS threshold can be increased by broadening the line width of the pump signal and the popular way to broaden the spectrum is by using phase or frequency modulation [11, 75]. Using rod type photonic crystal fiber (PCF) in the final amplifier stage and modulating the seed with pseudo-random noise signal, SBS is managed and the peak power reaches 1.5 MW (~2mJ pulse energy) with ~1.55 ns pulses at 10 kHz repetition rate [75]. In another report, with a chirp of 2.5×10^{15} Hz/s for the pump diode, an order of magnitude for the SBS threshold is achieved in a 20-m-length fiber [76].

Second, SBS can be suppressed by broadening the SBS spectrum of the fiber when a strain distribution or temperature distribution is applied to the fiber [77, 78]. An 8 dB SBS threshold increase is achieved when applying a 40-step stair-ramp tensile strain distribution in a 580-m-length dispersion shift fiber [79]. Yoshizawa et al. proposed a new fiber cable which applies sinusoidal fiber strain distribution of $\pm 0.35\%$ to expand the Brillouin gain spectrum from 50 MHz to 400 MHz, and a more than 7 dB increase in SBS threshold is obtained [80]. The SBS threshold is increased by threefold for a 100-m-length highly nonlinear fiber when applying 140 °C of temperature gradient [81].

Third, the threshold can be raised by attenuating the Brillouin Stoke wave. Hojoon et al. proposed a fiber with single or multiple Bragg grating inside, the grating is designed to match the spectrum of the Brillouin scattering to filter the spectrum out. By doing so, 15 ns Q-Switch pulses with 2 kW peak power is transmitted through a 1 m fiber with little energy loss [82]. A few researchers also use isolators to block the backward propagation

Brillouin Stoke wave, by doing so, the threshold power is increased 1~ 2 dB in the experiments [83].

Finally, the SBS threshold can be increased by reducing opto-acoustic interaction. The SBS threshold is improved by 3 dB for a fiber which is specially designed to have large acousto-optic effective area [84]. A 6 dB improvement for SBS threshold is realized by minimizing the overlap of the fundamental optical mode and acoustic modes when using the optical fiber with tailored acoustic speed profile [85].

2.2.3.5 Stimulated Raman Scattering (SRS)

SRS is first reported by Raman in 1928. When SRS happens in molecule medium, a small fraction of power will be transferred from one optical field to another field. The vibration modes of the molecule determine the frequency downshift amount [86]. From the quantum-mechanical viewpoint, when the difference between the pump signal and stock wave matches the energy of a vibration state of the molecule, the incident photon with frequency of ω_p pumps the molecule from ground state to a vibration state with higher energy level, at the same time, a photo with frequency of ω_s called Stokes wave is generated. Fig. 2-10 shows the energy diagram of the SRS from the quantum mechanics point of view [64].

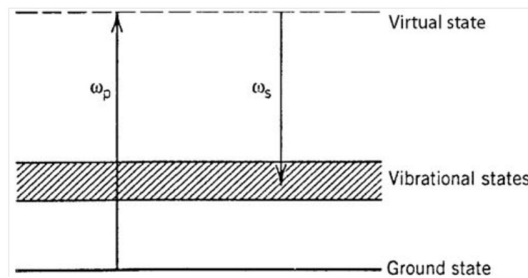


Fig. 2-10. Schematic illustration of the energy diagram of SRS from quantum-mechanical viewpoint [64].

The Raman gain spectrum for silica fibers at 1 μm is a broadband spectrum up to 40

THz with the peak located around 13 THz [87]. When the Stokes power at the fiber output is equal to the pump power, then the input pump power is defined as Raman threshold [68]. The forward Raman threshold P_0^{CR} can be estimated by the following equation [68, 64]:

$$g_R P_0^{CR} L_{eff} / A_{eff} \approx 16 \quad (2.11)$$

Where the L_{eff} is the effective fiber length, A_{eff} is the effective core area, and g_R is the Raman gain coefficient. For backward Raman threshold, the equation still can be used, but the numerical factor need to be changed from 16 to 20.

SRS is a significant and useful nonlinear effect for Raman amplifier, Raman laser and Raman spectroscopy etc. [88-91]. SRS doesn't produce giant pulse which could permanently damage the laser cavity like the SBS will do. The laser line width sometimes is not much cared especially when the laser is under CW operation conditions. However, SRS is also one of the limitation factors capping the power extracted from the fiber laser cavity. SRS reduces the gain of the signal and limits the output peak power for pulse fiber laser when it happens. Several approaches have been proposed by researchers to suppress SRS in fiber laser.

The first one is the implementation of a specially designed fiber to filter out the SRS signal [92]. Fini et al. suggest using a filter fiber with a core-ring design into an YDF. The core-ring has a predefined refractive index profile so that the ring performs a resonant coupling of the index matched noise wavelength light out of the core. The ring is in the cladding without gain, and the noise SRS is filtered to a certain extent. From their experiments, the difference between the signal and the 1st Raman peak is 40 dB when using a 16-m core-ring design filter fiber at 0.83 W output power. By contrast, the

difference is 23 dB when a reference fiber without core-ring designs [92]. Dual-hole assisted single-polarization fiber has the property of single-polarization propagation, which means that the two polarization modes have differential cut-off wavelengths [93]. In this fiber, the propagation of light at wavelengths longer than the cut-off window wavelength is strongly coupled to the cladding modes and thus experiences greater losses than propagation in the fiber core [94]. The counter-propagating Raman amplified spontaneous emission in the 300-m single mode dual-hole-assisted fiber measured is 23 dB reduction fiber comparing with SMF-28 with input power of 1W at the pump wavelength of 1486 nm.

Another proposal to suppress the SRS is by implementing a lumped spectral filter in the cavity of high power fiber laser and amplifiers [95]. Nodop et al. increasing the SRS threshold by inserting long period grating in a fiber amplifier, the long period apodized grating employed in the amplifier couples the Stokes wavelength from the core of the DCF to the cladding, thus reducing the gain of the SRS. The 1% Raman threshold for each long-period grating is increased by 30% and the extraction output power from the laser amplifier is doubled [96].

By using a double-clad fiber with a large mode area (LMA), the power density in the fiber is reduced and the fiber length is shortened, resulting in a decrease in nonlinearity [97]. However, lasers produced in LMA fibers are usually multimode by increasing the diameter of the fiber core only, which results in poor beam quality, sensitivity to bending and beam lurch conditions. Many researchers have turned to photonic crystal fibers (PCFs) for high peak power and single mode operation of laser systems because the core numerical aperture (NA) of PCF is reduced by its microscopic geometry [98, 99]. In 2006,

a 4.5 MW peak power, 1 ns pulse duration, and 100 μm Yb-doped PCF fiber MOPA system were reported [98].

2.2.3.6 Mode instabilities

Mode instabilities are the limiting factor for extracting high average power from LMA fiber laser cavity. A threshold like onset was observed six years ago when the mode instabilities happened. The beam quality remains stable when the power of the laser goes below the threshold. However, the beam quality deteriorates suddenly after reaching the threshold power scale, and the power is transferred between fundamental mode and higher-order modes [26]. The mode instabilities can occur in CW and pulsed fiber laser operation, which means this phenomenon is independent of peak power [100, 101].

The mode instabilities of patterns have aroused strong interest from researchers all over the world. Numerous experiments have been performed and several numerical models have been developed [102-104]. The reason behind mode instabilities is not fully understood yet. The origin of mode instabilities is most likely to be heat [105]. When two transverse modes are excited and interfere with each other, a quasi-periodic intensity pattern is formed in the active fiber core. This quasi-periodic intensity pattern eventually produces a periodic temperature profile, and the profile modulates the refractive index and induces a quasi-periodic change index due to the thermo-optical effect [26, 106].

Several methods have been proposed for mitigating the effects of mode instability. A few of them are derived from novel fiber designs, such as reducing the overlap between basic and high-order modes [107,108]. Reducing the wavelength difference between the signal and the pump is a way to reduce the quantum defect and result in a lower thermal effect, and in turn increase the threshold [109]. The mode instability is increased by

manipulating the pump and signal irradiance through cladding and core size choosing, injecting seed power etc. [110].

2.2.4 Step-index large mode area (LMA) fiber and photonic crystal fiber (PCF) **LMA**

For many laser applications, a near-diffraction-limited laser beam is preferred. When a high power YDPFL with near-diffraction-limited beam quality propagates along a conventional tiny fiber core, the high-power density results in nonlinear effects, which have been discussed in the previous section. Many researchers have suggested that the main nonlinearities (such as SBS and SRS) can be suppressed or eliminated by LMA fiber. From the definition of numerical aperture (NA) and the V number of step-index fiber:

$$NA = (n_1^2 - n_2^2)^{\frac{1}{2}} \quad (2.12)$$

$$V = \frac{2\pi a}{\lambda} NA \quad (2.13)$$

Where n_1 and n_2 represent the refractive index of the fiber core and cladding. a is the radius of the fiber core and λ is the wavelength.

Obviously, when increasing the core radius of a conventional ytterbium-doped step index fiber to reduce the power density, it is indispensable to simultaneously reduce the NA to maintain the same value of V in order to maintain the fundamental mode of operation. For strict single-mode operation of a step index fiber for 1.06 μm laser operation, the maximum core diameter of the fiber is 13 μm (0.06 NA). This method of increasing the fiber core radius but reducing the NA at the same time works to some extent. However, since it is hard to precisely control the NA of the fiber with MCVD type core, there is always a lower practical limit for NA reduction [111]. When the core diameter is scaling up beyond $\sim 15 \mu\text{m}$, it is exceedingly challenging for maintaining fundamental

mode operation due to the reproducibility and uniformity requirements. Thus, in most cases, conventional step index LMA fibers operate in several modes or multiple modes. Researchers have proposed the method to control the output laser beam quality by pattern matching of the input seed and carefully coiling to help leak any higher-order-modes (HOMs) [112]. It helps to improve the quality of the laser beam but does not completely solve this multimode issue and the mode compression caused by the coiling reduces the effective mode area in the fiber which leads to a decrease in the threshold of nonlinear effects [113].

Another approach is to use a PCF that has the same cladding as a conventional fiber but includes a 2D periodic array of air holes along the length of the fiber [114]. A photonic crystal is a structural material on an optical wavelength scale, a fraction of microns or less, such as the hole in the cladding. The regular morphology of the microstructures incorporated into the material will radically alter the optical properties of the material [115]. Many forms of PCFs are reported by researchers over the past decades. The core of a PCF may be either solid or hollow hole. Holes in the core and cladding can be filled with different types of liquids or metals to form PCF with specific properties [116]. Fig. 2-11 shows a cross-sectional view of a conventional fiber and PCF.

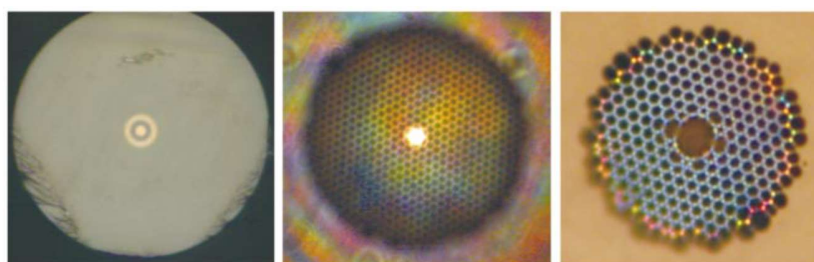


Fig. 2-11. (Left) Cross-section view of a standard optical fiber with 9 μm fiber core formed using two bulk materials. It is single-mode in the infrared and guides several modes at visible wavelengths. (Middle) an index-guiding PCF with 5 μm core diameter. It guides light in a single mode over the entire optical spectrum range. (Right) a hollow core bandgap PCF with 7 μm core diameter. It guides only over a limited range of wavelengths in the infrared that correspond to the bandgap of the cladding material [115].

For controlling the refractive index of the fiber, PCF gets the overwhelming superiority over the conventional step-index fiber. The NA and uniformity of a PCF can be precisely adjusted by varying the size of the embedded holes and the pitching between holes [117]. This makes it possible to fabricate a PCF core with very low NA and even “negative” NA (i.e., smaller refractive index compared to the cladding background index) [111].

The manufacturing single-mode PCFs with core diameter from 10 μm to more than 100 μm are possible after carefully design the cladding structures and the high order mode normally experience higher losses or less overlap with the core region during the propagation. In summary, the PCF is a superior candidate for high power YDPFLs with outstanding beam quality for the output laser.

2.2.5 Configurations of high power Ytterbium-doped pulsed fiber lasers

The typical configuration of high power YDPFLs is MOPA structure [21, 118, 119]. There is a seed source to produce seed laser pulses, and followed by one or multiple cascade amplifiers. The seed laser can be generated through mode-lock, Q-switch and directly modulated LD techniques etc [12-14, 16, 18-23]. By using the mode-lock technology, laser pulses with high pulse repetition rate and ultrashort pulse duration can be reached. For the Q-switch method, the gaussian-like-shape laser pulses can be generated. When directly modulated LD is applied, the laser pulse duration and pulse repetition rate can be tuned per application’s requirements. For the amplifier stage, the forward, backward and bi-direction pump schemes are implemented by researchers. For the forward pump, the forward ASE is lower, however, the output power is less especially when the seed laser injected is with low pulse energy [120].

The state-of-the-art peak power for ns YDPFL is single mode, 1 ns pulse duration with

2.4 SUMMARY

In this chapter, the background information of YDPFLs and the elements associated with YDPFLs have been reviewed.

Fiber laser is a laser that whose waveguide is a fiber and whose gain media is rare earth ions doped in the fiber core. It has a history only one year later than the invention of laser. There are lots of advantages for using fiber as gain medium for a laser, such as the huge area-to-active volume ratio, the higher optical to optical conversion efficiency and all fiber monolithic configuration etc. Because of these merits, the power scale of both CW and pulsed fiber laser advances quickly especially after the double-cladding pumping and high power multi-mode diode technologies presented in the late of 1980s.

For DCF, the signal laser and pump laser propagate along the fiber core and cladding, respectively. Several different shapes of DCF have been invented to improve the pumping light absorption efficiency. For Yb^{3+} ions doped to the host fiber to emit laser light at 1 μm wavelength, the broadband absorption and emission spectra make it a suitable candidate for using pump laser at a wide wavelength range and even intra-band pump. Due to the high quantum efficiency of Yb^{3+} , the output power of YDF laser has increased significantly over the past several decades.

Fiber is the ideal waveguide for lasers, and the geometry of the fiber is the basis for most of its merits. However, the small core and long cavity length results in a high power density, which provides favorable conditions for nonlinearities such as SBS, SRS, SFM and gain saturation etc. Due to the extremely high laser power, several thermal limitations also need to be addressed during the laser design. These limitations have been reviewed

and the researchers have suggested a number of ways to suppress or mitigate them. For a few laser applications, the near-diffraction-limited laser beam is preferred. When high power laser pulses with near-diffraction-limited beam quality propagation along the conventional small fiber core, the high power density will not just give rise to severe nonlinear effects, but also induce catastrophic damage to the bulk and surface of the fiber. The step-index LMA method works to some extent. However, due to the difficulty for precisely controlling the NA of the step index fiber with MCVD type core, there is always a lower practical limitation for the NA reducing. The NA and uniformity of the PCF can be precisely adjusted by varying the size of the embedding hole and the pitching. This makes it possible to fabricate PCF cores with extremely small NA to meet high power and near-diffraction-limited beam quality requirements.

Due to the many merits associated with YDPFLs, they have been widely utilized in varieties of fields, such as industry, military, research and medical treatment etc.

Chapter 3 PULSED PUMP YTTERBIUM-DOPED PULSED FIBER LASER

FIBER LASER

3.1 INTRODUCTION

The more energy is stored in the laser cavity, the more gain is available for the signal pulsed laser injected. At the same time, there is more ASE component. Large amount of stored energy is the basis for high power YDPFLs. However, if the ASE is not properly controlled, undesired laser treatment outcomes or self-lasing may occur. Thus, the inter-pulse ASE needs to be cautiously controlled. Fig. 3-1 shows the marking effect of YDPFLs on ink paper. The image on the left side shows that the laser with large residual energy in the cavity forms the unwanted tail. However, this does not occur to the image on the right side.

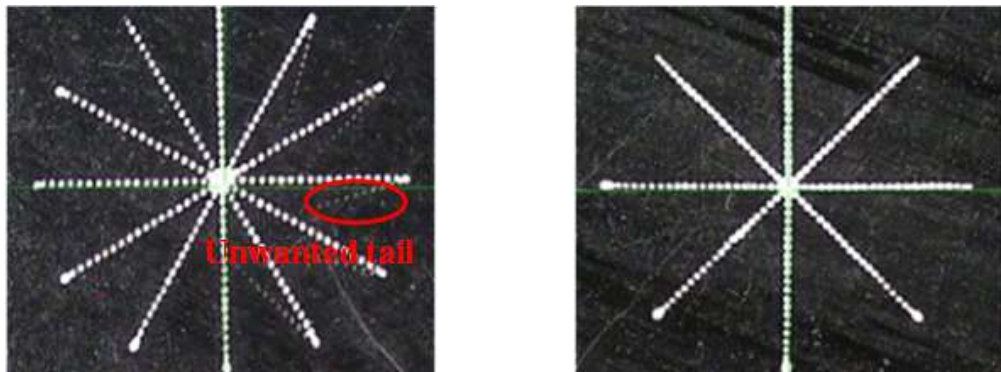


Fig. 3-1. Marking results on ink paper with an YDPFL (Images are from JPT Inc.). (Left) Residual energy stored in the cavity causes the unwanted tail. (Right) Marking result without unwanted tail.

The energy stored in the laser cavity is related to the nature of the host material, the properties of the rare earth ions, the pump power level, the pump method, and the signal laser etc. In this chapter, I will investigate the relationship between these elements.

3.2 NUMERICAL MODEL OF YTTERBIUM-DOPED PULSED FIBER AMPLIFIER

As discussed in the previous chapters, high power YDPFLs are widely used for industry due to their many merits. The inter-pulses ASE is a concern for the lasers as it consumes upper level populations leading to lower efficiency of the final output laser, heats the components in the laser cavity which in turn affects the robustness of the laser, results in self-lasing which causes the instability of the laser operation and affects the maximal reachable pulse energy extracted from the laser cavity. By using pulsed pump instead of CW pump to suppress the ASE is one of the widely used methods suggested by researchers. For example, in 2009, Huang et al. achieved 30 dB gains from an ytterbium-doped fiber amplifier through the pulsed pump to suppress the ASE for a 100-ns pulse with 100 Hz pulse repetition rate [118]. In 2014, a fiber laser with 55 mJ pulse energy and 10 ns pulse duration at 10 Hz pulse repetition rate was reported [119]. The laser was made up of seven cascaded amplifiers and a pulsed pump with different pump power and duration was implemented.

Theoretical modeling and numerical analysis provide the indispensable guidance for ytterbium-doped double-clad fiber amplifier (YDFA) design. A number of papers have been reported on the dynamics of pulsed YDFA with CW pump on a numerical basis [120]. However, few are available for pulsed pump. In 2013, Wei T. et al reported the study on the optimal duration of the pulsed pump, the study is focusing on one pump power level which is not universal [122]. For pulsed pump, the most crucial factors to be determined for amplifier design are the pump power (P_p) and pump duration (t_p). Driven by this, in this section, the laser pulse evolution in a pulsed pump YDFA is numerically studied by solving time-dependent rate equations. The dynamics of the ASE, pulse energy

and efficiency of the pulsed YDFA under pulsed pump with different P_p and t_p are investigated.

3.2.1 Theoretical Modeling

The configuration of the ytterbium-doped double-clad fiber amplifier is demonstrated in Fig. 3-2. The ytterbium-doped double-clad fiber has a length of L and a core/cladding diameter of 30/250 μm . The 200 ns trapezoidal shape seed laser pulses with rising and falling edges of 1 ns at 1064 nm wavelength are produced from a MOPA source. The seed signal with a FWHM bandwidth of 2 nm is injected from the left end of the fiber. Sixteen ASE channels with $\Delta\lambda$ of 5 nm are considered in the calculation. The other parameters are shown in Table 3-1 and the simplified rate equations for the ytterbium-doped double-clad fiber amplifier are as follows [120], where z and t represent the coordinate and time respectively. The N_0 , N_1 and N_2 are for the ytterbium dopant concentration, ground and upper level population respectively. σ_a and σ_e are the absorption and emission cross-section of the gain fiber and the values are from the manufacturer (Nufern Inc.). λ_p , λ_s and λ_k represent the central wavelengths of the pump, signal and ASE respectively. τ is the life time of the upper level ions. Γ_p and Γ are the filling factors for the pump and signal. $S\alpha_{RS}$ is the Rayleigh scattering factor. A is the fiber core size and α is the attenuation coefficient of the fiber. v_p and v are the group velocities of the pump and signal (ASE). P_p^\pm , $P^\pm(z, t, \lambda_k)$ and $P^\pm(z, t, \lambda_s)$ are the forward and backward pump power, ASE power and signal power. P_{pin} and P_{sin} are the pump and signal power injected into the amplifier.

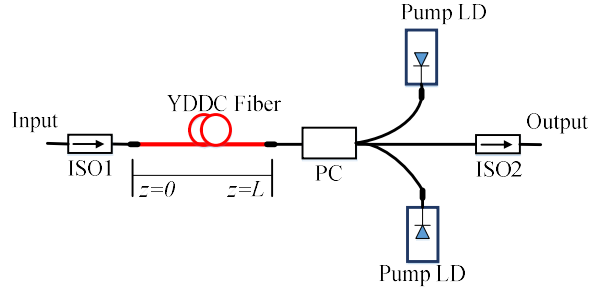


Fig. 3-2. The YDDC fiber amplifier configuration with backward pulsed pump scheme (ISO: Isolator, PC: Pump combiner).

Table 3-1. Part of the parameters used in the simulations.

λ_p 915 nm	λ_s 1064 nm	λ_l 1020 nm	λ_K 1100 nm
τ 880 μ s	$S\alpha_{RS}$ $1.2 \times 10^{-7} \text{ m}^{-1}$	N_0 $7.7 \times 10^{25} \text{ m}^{-3}$	A $7 \times 10^{-10} \text{ m}^2$
Γ_p 0.01	Γ 0.83	L 7 m	$\Delta\lambda$ 2 nm

$$\frac{dN_2(z,t)}{dt} = \frac{\Gamma_p \lambda_p}{hcA} [\sigma_a(\lambda_p) N_1(z,t) - \sigma_e(\lambda_p) N_2(z,t)] \cdot [P_p^+(z,t) + P_p^-(z,t)] - \frac{N_2(z,t)}{\tau} + \quad (3.1)$$

$$\frac{\Gamma}{hcA} \sum_{k=1}^K \lambda_k [N_1(z,t) \sigma_a(\lambda_k) - N_2(z,t) \sigma_e(\lambda_k)] \cdot [P^+(z,t, \lambda_k) + P^-(z,t, \lambda_k)]$$

$$N_0 = N_1 + N_2 \quad (3.2)$$

$$\pm \frac{\partial P_p^\pm(z,t)}{\partial z} + \frac{1}{v_p} \frac{\partial P_p^\pm(z,t)}{\partial t} = -\Gamma_p [\sigma_a(\lambda_p) N_1(z,t) - \sigma_e(\lambda_p) N_2(z,t)] \times P_p^\pm(z,t) - \quad (3.3)$$

$$\alpha(\lambda_p) P_p^\pm(z,t)$$

$$\pm \frac{\partial P_p^\pm(z,t, \lambda_k)}{\partial z} + \frac{1}{v} \frac{\partial P_p^\pm(z,t, \lambda_k)}{\partial t} = -\Gamma [\sigma_e(\lambda_k) N_2(z,t) - \sigma_a(\lambda) N_1(z,t)] \times P^\mp(z,t, \lambda_k) - \quad (3.4)$$

$$\alpha(\lambda_k) P^\pm(z,t, \lambda_k)$$

$$\pm \frac{\partial P_p^\pm(z,t, \lambda_k)}{\partial z} + \frac{1}{v} \frac{\partial P_p^\pm(z,t, \lambda_k)}{\partial t} = -\Gamma [\sigma_e(\lambda_k) N_2(z,t) - \sigma_a(\lambda) N_1(z,t)] \times P^\mp(z,t, \lambda_k) -$$

$$\alpha(\lambda_k) P^\pm(z,t, \lambda_k)$$

$$\pm \frac{\partial P^\pm(z, t, \lambda_k)}{\partial z} + \frac{1}{v} \frac{\partial P^\pm(z, t, \lambda_k)}{\partial t} = \Gamma[\sigma_e(\lambda_s)N_2(z, t) - \sigma_a(\lambda_s)N_1(z, t)] \times P^\pm(z, t, \lambda_s) - \alpha(\lambda_s)P^\pm(z, t, \lambda_s) + 2\sigma_e(\lambda_s)N_2(z, t) \frac{hc^2}{\lambda_s^3} \Delta\lambda_s + S\alpha_{RS} \times P^\mp(z, t, \lambda_s) \quad (3.5)$$

The initial boundary conditions are as below:

$$P_p^+(0) = 0 \quad (3.6)$$

$$P_p^-(L, t) = P_{pin}(t) \quad (3.7)$$

$$P^+(0, t, \lambda_s) = P_{sin}(t) \quad (3.8)$$

$$P^-(L, t, \lambda_s) = 0 \quad (3.9)$$

$$P^+(0, t, \lambda_k) = 0 \quad k = 1, \dots, K, k \neq s \quad (3.10)$$

$$P^-(L, t, \lambda_k) = 0 \quad k = 1, \dots, K, k \neq s \quad (3.11)$$

The rate equations are solved with a time step of 250 ps. The calculation of the pulses is ceased only when the variation of the peak power is less than 0.3% for the successive pulses. In the simulations, the injected seed laser is with 150 W peak power and 200 ns pulse duration (base of the pulse). The seed pulse energy is kept at 30 μ J with 100 Hz pulse repetition rate and the amplifier has a signal gain of approximately 10 ~ 20 dB. The 7-m-length fiber ensures more than 98% pump power be absorbed by the fiber.

3.2.2 Laser Pulses Analysis and Characteristics

3.2.2.1 Amplifier working with different P_P and t_p

The N_2 along the gain fiber before the seed laser injecting into the amplifier is shown in Fig. 3-3 with several t_p from 300 μ s to 700 μ s and 20 W P_P . It is increased along the fiber and reached its peak at the pump end of the fiber when the t_p is less than 400 μ s. However, for longer t_p from 500 μ s to 700 μ s, the peak is no longer at the pump end of the fiber, but moves to the opposite end. The stronger ASE generated reduces N_2 that leads to lower N_2

at the pump end of the fiber.

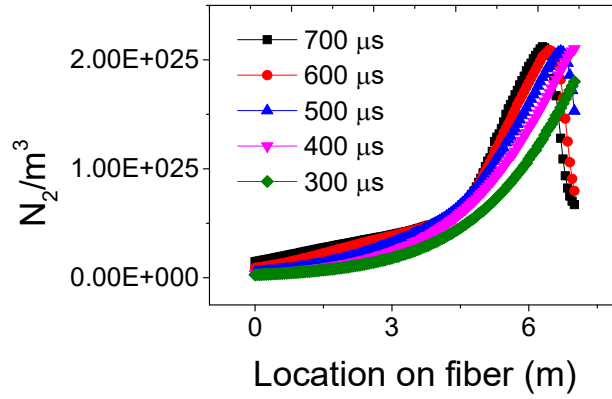


Fig. 3-3. Upper level population (N_2) along the gain fiber for several pump durations at 20 W pump power.

Fig. 3-4(a) manifests the output pulse energy increases as a function of t_p at several P_P levels. However, the maximum achievable pulse energy increased for 30 W P_P is insignificant comparing with the 20 W because of the saturation of the stored energy as show in Fig. 3-4(c). As expected, the t_p for reaching maximum pulse energy is quickly shortened with higher P_P , and the corresponding t_p is 300 μ s, 500 μ s and 1500 μ s for the 10 W, 20 W and 30 W P_P respectively.

As can be seen in Fig. 3-4(b), the maximum amplifier efficiency grows from 25.7% to 35.7% with P_P increasing from 10 W to 30 W. Similar to the maximum achievable pulse energy in Fig. 3-4(a), the improvement in maximum efficiency slows down gradually as the P_P increases. The t_p for reaching the maximum efficiency is shorter than that for achieving the maximum pulse energy as after that more pump energy contributes to the ASE.

The N_2 distribution in the gain fiber before seed laser injection into the amplifier with t_p is shown in Fig. 3-4(c). Obviously, the stored energy grows rapidly at first with longer t_p , then the increasing rate slows down and eventually the stored energy saturates at a certain

level. The t_p for reaching saturation is longer than that for the maximum efficiency and maximum output pulse energy. The reason behind is that the increase in ASE power becomes significant when pump duration is longer than the t_p corresponding to the maximum pulse energy, and this leads to a change in the N_2 distribution.

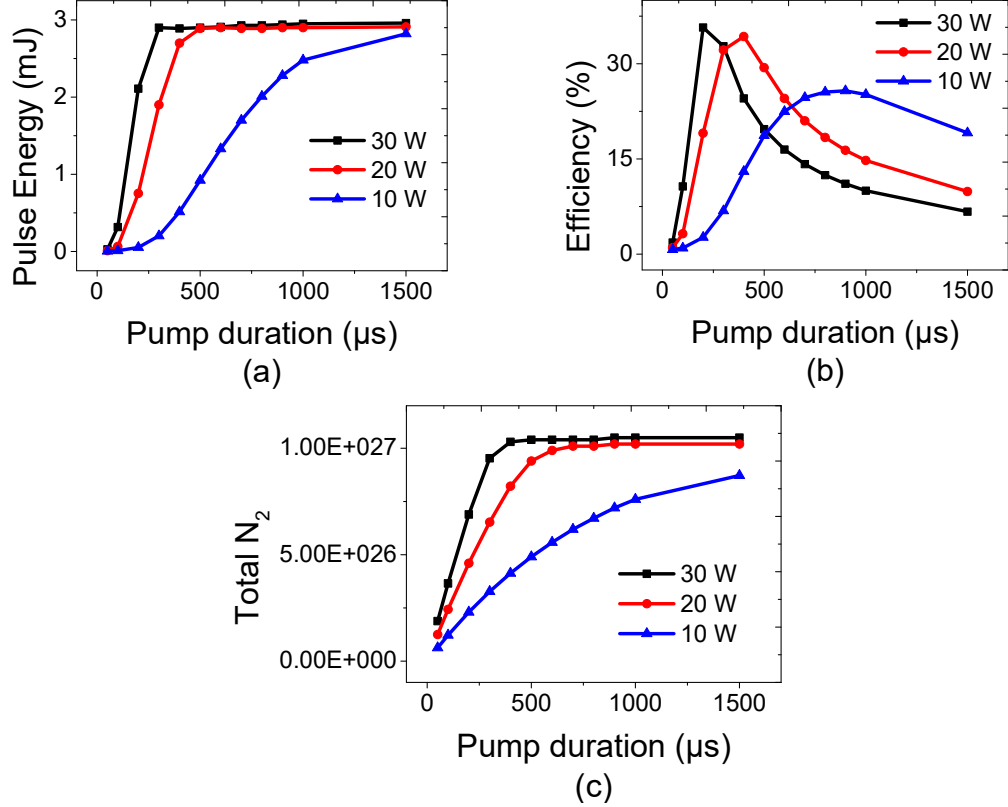


Fig. 3-4. (a) The pulse energy, (b) efficiency and (c) total upper level population in the gain fiber with pump duration from 50 μs to 1500 μs at pump power of 10 W, 20 W and 30 W.

The output forward and backward ASE power before the seed laser is injected into the amplifier is shown in Fig. 3-5. The forward ASE power is higher than the reverse one as the backward pump scheme is used for the amplifier. The ASE power is in a low level when the t_p is less than the t_p for reaching the maximum efficiency. It grows quickly after that and eventually gets saturated and reaches a plateau, where the amplifier can be considered as working in CW mode. Obviously, the higher the P_p , the more the ASE

power.

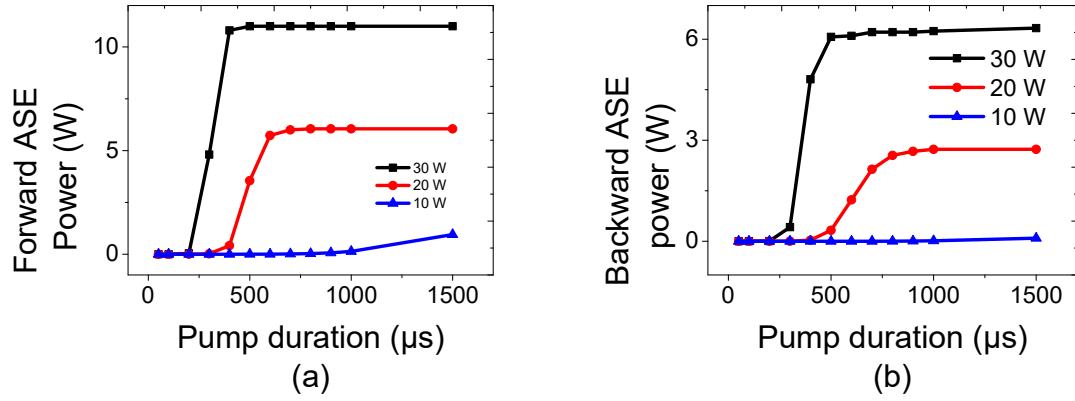


Fig. 3-5. (a) Forward and (b) backward ASE power vs. pump duration at 10 W, 20 W and 30 W pump power.

3.2.2.2 Amplifier working with same pump energy

From Fig. 3-6, the t_p for the maximum efficiency is shortened and the pulse energy is increased at higher P_p . In order to further study the relationship between the pulse energy and the t_p , the following simulation is performed. The YDFA is working with fixed pump energy of 12 mJ and pulse repetition rate of 100 Hz, the sets of P_p and t_p are listed in Table 3-2.

Table 3-2. Different sets of P_p and t_p combinations.

Pump duration (μs)	6000	4000	2000	1000	900	800	700	600	500	400	300	200	100
Pump power (W)	2	3	6	12	13.3	15	17.1	20	24	30	40	60	120

From Fig. 3-6(a), although the pump energy is the same, the stored energy in the gain fiber continues to increase with shorter t_p . From Fig. 3-6(b), it manifests that the pulse energy keeps growing rapidly when t_p is shortened from 4000 μs to 1000 μs . When t_p is longer than 4000 μs , the output pulse energy and laser efficiency are extremely low.

When the t_p is less than 1000 μs , the growth of the pulse energy slows down and eventually ceases at ~ 2.9 mJ. The curves for the N_2 distribution along the gain fiber before the seed pulse injected are depicted in Fig. 3-6(c). The N_2 distribution along the fiber is increased when the t_p shortened from 6000 μs to 2000 μs . The increase results to the higher stored energy in the gain fiber and also the output pulse energy. However, when the t_p is less than 1000 μs , the peak of the N_2 distribution curve deviates from the pumping end of the fiber and it grows taller and steeper. The forward and backward ASE before the seed pulse injecting is shown in Fig. 3-6(d). The N_2 distribution along the fiber and the stored energy in the fiber are different under different pump scheme. These factors lead to the forward ASE to be stronger than backward one, especially at shorter t_p with higher P_p . Both the forward and backward ASE is below 0.3 W at 2000 μs t_p , then the forward ASE rises to ~ 1.25 W at t_p of 1000 μs and further increases to more than 50 W at 100 μs t_p . In reality, the ASE at this high level may cause self-lasing, and high P_p requirements also lead the design not cost effective. A strong forward ASE with a short t_p results in a lower N_2 distribution at the pump end of the fiber. From the above analysis, it can be seen that the different P_p and t_p combinations result in different N_2 distributions along the gain fiber, thus the different forward/backward ASE and the stored energy in the amplifier. When the injected seed laser travels through the amplifier, the N_2 distribution determines the output pulse energy and hence the efficiency.

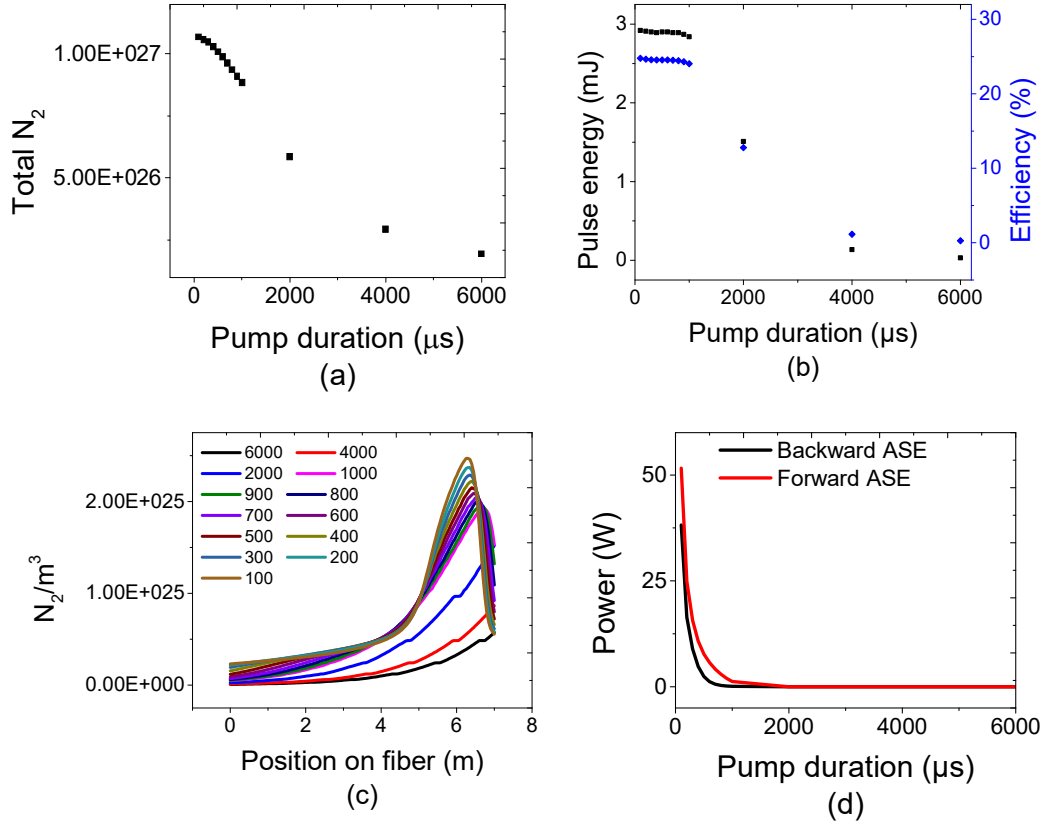


Fig. 3-6. At different t_p , (a) Total stored energy in the DCF, (b) Pulse energy and efficiency, (c) The N_2 distribution along the fiber, and (d) Forward and backward ASE.

3.2.2.3 Amplifier working with different injecting seed laser

To study the influence of the seed laser to the final output laser, the following simulation has been performed. From the previous analysis, the t_p for reaching maximal pulse energy for 20 W P_P is $\sim 500 \mu s$. Here we will choose the 400 μs and 600 μs pump duration which is shorter and longer than the 500 μs t_p . The YDFA works with 20 W P_P . The 200-ns trapezoidal shape pulse with rising and falling edges of 1 ns at 1064 nm wavelength is used as seed pulse. First, the 400 μs t_p is used and the seed pulse energy varies from 10 μJ to 50 μJ in a step of 10 μJ by changing the peak power but keeping the t_p . The output pulse energy and efficiency curves are shown in Fig. 3-7(a). It is obvious both pulse energy and efficiency are improved for the seed with higher pulse energy. The

final output pulse energy grows from 2.43 mJ to 2.78 mJ and the efficiency increases from 31% to 35.5%. From the trend of the curves both pulse energy and efficiency will saturate eventually. Second, 600 μs t_p is used. From the Fig. 3-7(b), there is no significant changing for the pulse energy (~ 0.02 mJ difference) and efficiency ($<0.02\%$ difference) with different seed pulse energy. This indicates the method for extracting higher pulse energy and higher efficiency by increasing the seed pulse energy works just when the t_p is less than the pump duration corresponding to the maximum pulse energy. However, if the increasing of the seed pulse energy is not by enhancing the peak power but widening the pulse duration, the situation is different. Fig. 3-7(c) shows the pulse energy and efficiency increase with 600 μs t_p when the seed pulse energy is enhanced by wider pulse duration but keeping the peak power. During the simulation, the seed laser pulse is synchronized to the end of the pump pulse. If the seed pulse is injected at the beginning or center of the pump pulse, the efficiency will be reduced. There is more discussion about this in Section 3.3.1.

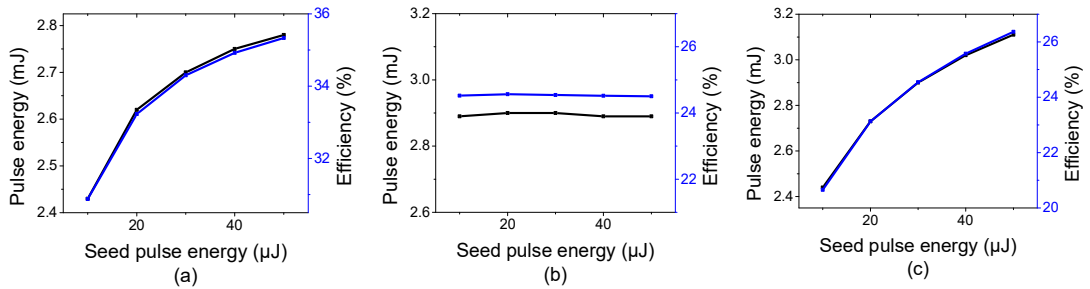


Fig. 3-7. Dependence of the final output pulse energy and efficiency on the seed pulse energy (by changing the peak power of the seed pulse) for $t_p = 400 \mu\text{s}$ (a) and $t_p = 600 \mu\text{s}$ (b) respectively. (c) dependence of the output pulse energy and efficiency on the seed pulse energy (by changing the seed pulse duration but keeping the peak power constant) at $t_p = 600 \mu\text{s}$.

3.2.3 Discussion and Conclusion

For YDFA with pulsed pump design to achieve lower ASE, the most crucial factors, P_p

and t_p , have been numerically studied in this section. The relationship between pulse energy, efficiency, and ASE versus P_p and t_p has been investigated by modeling the pulsed pump amplifier and solving the rate equations.

With the same P_p , when the amplifier operates at t_p corresponding to the maximum efficiency, the ASE is in a relatively low level. The ASE grows quickly when further increasing t_p and eventually it becomes constant. The laser system then can be considered as working in CW mode for the ASE. For different P_p levels, the pulse energy increases with higher P_p and eventually saturates, then pump energy contributes more to ASE instead of signal laser. By enhancing the peak power of the seed laser to increase the injecting seed pulse energy, larger pulse energy and higher efficiency can be achieved at final output when pump duration is less than the t_p corresponding to the maximum efficiency.

When using the pulsed pump avenue, the shorter the t_p , the higher the pump peak power required. This indicates that the laser system needs to be pumped with more P_p which results in higher cost. However, when operating at low pulse repetition rate with low duty cycle, the commercial 9-xx nm pump laser diodes can operate at 5~7 times higher output power than in CW mode [123]. This can be utilized to offset some of concern on the cost.

Nonlinear effects such as SBS, SRS and SPM have not been considered. They absolutely affect the performance of the amplifier and part of the simulation results, especially when the peak power or the pulse energy is at high level. However, they do not affect the relationship among the t_p , P_p , pulse energy, efficiency and ASE, which are the focal points in this section. During an YDFA design, all of these need to be addressed.

3.3 PULSED PUMP FOR YTTERBIUM-DOPED PULSED FIBER LASER WITH TUNABLE PULSE DURATION

As discussed in Chapter 2, high power YDPFLs have been rapidly evolving over the past decade due to their wide range of industrial applications. The YDPFLs with larger pulse duration (hundreds of nanoseconds) are mainly used for material removing and engraving as they possess higher pulse energy and more thermal effect simultaneously [124,125]. For the ones with shorter pulse duration (several to tens of nanoseconds), they are more frequently utilized in precise applications such as indium tin oxide (ITO) etching, sub-millimeter 2D barcode marking and black marking, etc [126].

A typical nanosecond YDPFL can be configured with a seed source to produce seed laser pulses through Q-switch oscillator or directly modulated LD, and followed by several cascade amplifiers. This configuration is also termed as MOPA. The pulse repetition rate of these lasers can be tuned per application's requirements. When the seed laser of a nanosecond YDPFL is generated by the directly modulated LD technique, the pulse duration can be tuned from sub-nanosecond to hundreds of nanoseconds or even larger. The pulse duration tunable feature is highly desirable for many applications.

For the laser design with tunable pulse duration and pulse repetition rate, there is a threshold pulse repetition rate (f_t) for each pulse duration to get the maximum average output power with largest pulse energy (Fig. 3-8(a)). When the laser is operating with a pulse repetition rate (f) is higher than f_t , the average output power keeps at the maximal reachable level but smaller pulse energy. When f is less than f_t , the output power decreases because the energy of each pulse is maintained at the highest level. To achieve this, one straightforward way is to keep the pump power at the maximum reachable level

when f is equal to or larger than f_t (Fig. 3-8(b)). The pump power decreases and maintains at the CW pump scheme when f is less than f_t (Fig. 3-8(c)) [19], [127].

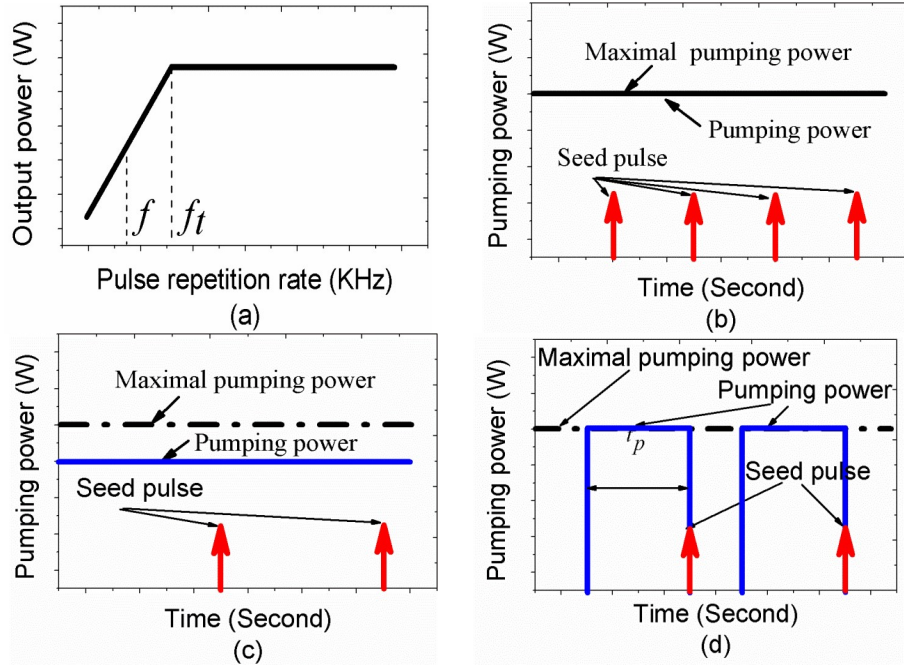


Fig. 3-8. (a) Relationship of the average output power of the laser with the pulse repetition rate (f). (b) The pump power maintains at the maximal reachable pump power level when f is equal to or larger than f_t . (c) The pump power is reduced and keeps at the CW pump scheme when f is less than f_t . (d) The pulsed pump scheme when the pulse repetition rate (f) is less than f_t .

However, when the YDPFL is working with CW pump at the pulse repetition rate less than f_t , the inter-pulse ASE is a concern. The ASE not only generates more heat leading to the degradation of the laser system, but also may give rise to self-lasing between pulses which could devastate the laser cavity. Pushed by this challenge, as discussed in Section 3.2, a few researchers suggest using pulsed pump instead of CW pump [13,123]. However, these reports are focused on suppressing ASE and getting higher pulse energy under either pulse repetition rate or pulse duration. As the lasers with adjustable pulse repetition rate or pulse duration which are widely utilized in current industrial market, in this section, the optimization of the pump design for an YDPFL with simultaneously tunable pulse

duration and pulse repetition rate is demonstrated. Before each seed pulse comes into the amplifier, the pumping LDs are applied with maximal reachable pump power (P_p) and the pump duration (t_p) is modulated according to the pulse duration (Fig. 3-8(d)). The t_p is fixed for each seed pulse. When the laser operates at $f = f_t$, t_p equals the time interval between pulses, and this causes the CW pump to be in reality. It is the same thing when $f > f_t$. When $f < f_t$, t_p is the same for each seed pulse but the duty cycle (DC) varies with the value of f . As both wide and narrow pulse duration are desirable for industrial applications, the YDPFL working with full width half maximum (FWHM) of 130 ns and 20 ns are investigated experimentally. Numerical modeling has been performed for the verification of the experimental results.

3.3.1 Experimental Design

The MOPA structure of the nanosecond YDPFL for the experiments is shown in Fig. 3-9. The seed laser pulses are generated from a Fabry-Perot (FP) laser diode (LC96A1064UBFBG-20R from II-VI Inc.) with central wavelength at 1065 nm and 3 dB bandwidth of 1.8 nm. A fiber Bragg grating (FBG) is spliced to the PM fiber pigtail of the LD to stabilize the central wavelength of the seed laser. The seed LD is directly modulated by the electrical circuit with tunable pulse repetition rate and tunable pulse duration.

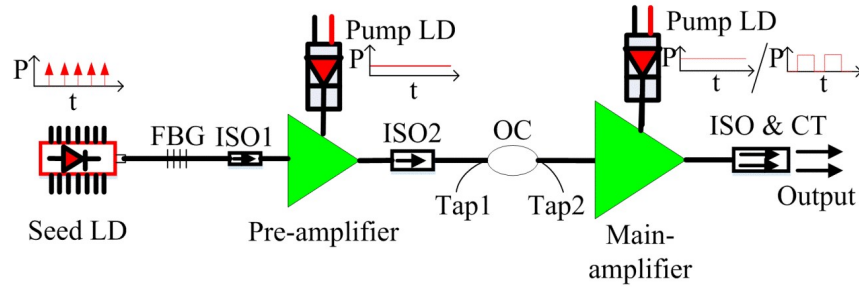


Fig. 3-9. Structure of the MOPA YDPFL. LD: laser diode, FBG: fiber Bragg grating, ISO: isolator, OC: optical coupler, CT: collimator, P: pump power level.

The pre-amplifier stage which consists of a $(1+1) \times 1$ combiner and a 2-meter-long Ytterbium-doped double-clad fiber is used to boost the seed pulses from the seed LD. The backward pump scheme is used. The core/inner cladding diameter and numerical aperture (NA) of the gain fiber are $7/128 \mu\text{m}$ and $0.19/0.46$ respectively. The inner cladding absorption is 1.3 dB/m at 915 nm wavelength. One 915 nm multimode LD with maximal 10 W output power is used for this stage. To ensure the same laser pulses are injected for the main amplifier stage during the pulsed pump and the CW pump experiments, the pre-amplifier stage is kept working under the CW pump scheme.

The structure of the main amplifier is similar as that of the pre-amplifier. The 6-meter-long gain fiber with core/inner cladding diameter of $20/130 \mu\text{m}$ is used for this amplifier stage. The fiber core NA is 0.08 . The inner cladding absorption of the Ytterbium-doped double-clad fiber is 2.1 dB/m at 915 nm wavelength. One $(2+1) \times 1$ combiner is used to couple the maximal $33 \text{ W } P_P$ from two multimode LDs at 915 nm into the amplifier.

Both the pre- and main amplifier stages are using the backward pump scheme to boost the injected laser pulses. By using this configuration, the optical-to-optical conversion efficiency can be improved comparing to the forward pump scheme.

Two fiber pigtailed isolators (ISO1 and ISO2) are equipped to block the counter-propagating light after the seed LD and the pre-amplifier stage. The band-pass film with

18 nm FWHM bandwidth centered at 1060 nm is coated on the optical lens surface within the isolator to filter out the ASE and the stimulated Raman scattering (SRS) components. One 1:99 optical coupler (OC) is for monitoring the forward and backward light in the cavity.

The output average power of the YDPFL after ISO1 and ISO2 with 130 ns pulse duration at 10 kHz repetition rate is 1.1 mW and 101.6 mW respectively. When it comes to the pulses with 20 ns pulse duration and 20 kHz pulse repetition rate, the power is 0.3 mW and 58.2 mW respectively. The damage threshold for the fused silica surface is ~ 0.48 mJ and ~ 0.23 mJ for 130 ns and 20 ns pulse respectively with 20 μm core fiber [128]. To prevent the fiber facet damaging a collimator with isolator embedded is spliced to the output fiber of the main amplifier. The efficiencies in the following paragraphs are obtained by calculating the ratio of the average output power of the YDPFL to the average P_P . The optical spectra are measured by YOKOGAWA AQ6370C and the pulse shapes are measured by Tektronix DPO4104B-L via a 1 GHz photo detector (PD).

It is required to synchronize the pulsed pump with the output of seed laser. To study the relationship of the timing between the seed laser and the pulsed pump, the following experiments with changing the injecting time of the seed laser are performed. The YDPFL works with 130 ns pulse duration, 10 kHz pulse repetition rate, 25 kHz f_t and ~ 13 W average P_P . No matter pulsed pump or CW pump is used for the main amplifier stage, the pre-amplifier stage is kept at CW pump to ensure the same injecting pulses for the main amplifier stage. The average input power of the laser for the main amplifier is 101 mW. Fig. 3-10 shows the timing relationship between the seed laser and the pulsed pump in the experiments. The seed laser is injected at the beginning (P1), middle (P2) and end (P3)

positions of the pulsed pump respectively.

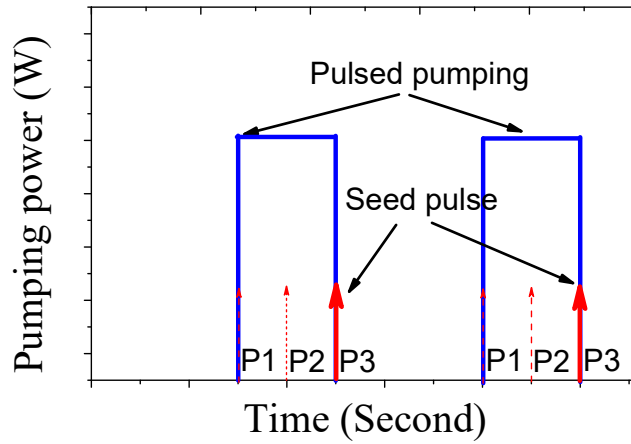


Fig. 3-10. Relationship of the seed laser and the pulsed pump.

The experimental results show that the average power of the final output laser is 6.4 W, 6.58 W and 6.7 W with the seed laser injected at the time of P1, P2 and P3 respectively. From the optical spectrum measured at Tap1 after using an AOM with 4 μ s window to filter out the reflection of the pulse laser, the YDPFL with the seed laser at P3 position has the lowest inter-pulse ASE (Fig. 3-11).

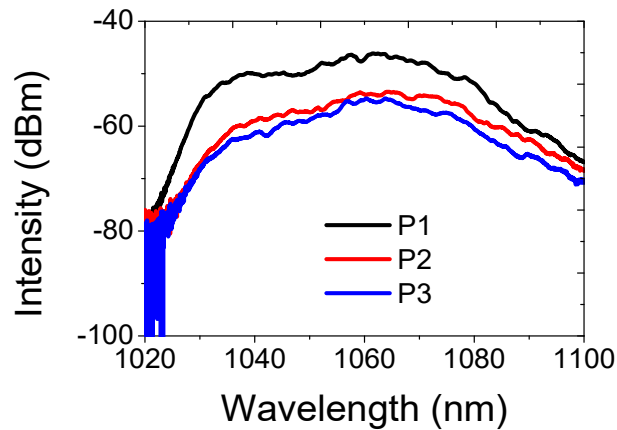


Fig. 3-11. When the seed laser is at the front (P1), middle (P2) and end (P3) positions of the pulsed pump, the optical spectrum of the inter-pulse ASE measured from Tap1 after using an AOM with 4 μ s time window to filter out the reflection of the pulse laser.

If postpone the injecting time of the seed laser further behind P3, there is more ASE

than that of P3. By synchronizing the injecting time of the seed laser with the end position of the pumping pulse, lower inter-pulse ASE and higher average output power are reached comparing with other injecting time of the seed laser.

3.3.2 Results and discussion

When the laser system is working with 130 ns pulse duration at 10 kHz pulse repetition rate, the P_p is at the maximal reachable P_p of 33 W and the t_p is 40 μ s calculated from $1/f_t$. After being boosted by the main amplifier stage, the peak power measured at the final output for pulsed pump is 12.3 kW and it is 13% higher than that of using the CW pump with same pump energy. The average power of the final output laser is 7.7 W and 8.01 W for the CW pump and the pulsed pump, respectively. From the optical spectra monitored at final output as shown in Fig. 3-12(a), the SRS is much stronger for pulsed pump than that of CW pump because of the higher peak power. The backward spectra from 1030 nm to 1090 nm monitored at Tap 1 indicate stronger inter-pulse ASE for CW pump.

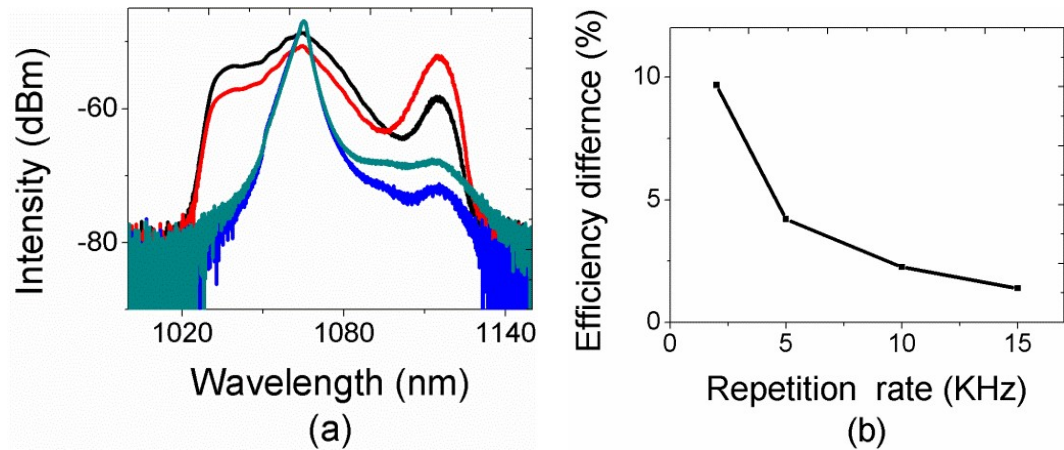


Fig. 3-12. The YDPFL is working with 130 ns pulse duration and the f_t of 25 kHz, (a) At 10 kHz pulse repetition rate, the optical spectra measured from tap1 (the black and red curves are for the CW and pulsed pump respectively) and final output (the blue and dark cyan curves are for the CW and pulsed pump respectively). (b) The efficiency difference for pulsed and CW pump schemes for several pulse repetition rates less than f_t .

Fig. 3-12(b) shows the efficiency improvement of the pulsed pump comparing with the CW pump when the laser system is working with the pulse repetition rates less than f_t . The efficiency improves by $\sim 10\%$ at 2 kHz and $\sim 1.3\%$ at 15 kHz pulse repetition rate respectively. As depicted in Fig. 3-12(a), the improvement is mainly because of the inter-pulse ASE being suppressed under the pulsed pump scheme. However, for higher pulse repetition rate the improvement is not as significant due to the already smaller inter-pulse ASE. This indicates the CW pump in reality is suitable when the pulse repetition rate equals to or higher than f_t (25 kHz) and it is hardly necessary to implement the pulsed pump through using additional P_p and shortening the t_p .

To further study the inter-pulse ASE, an acousto-optic modulator (AOM) with 4 μs time window is used to filter out the pulse laser signal during the measurement. From Fig. 3-13(a), the ASE after the pre-amplifier monitored at Tap 2 is similar for both the CW and the pulsed pump schemes. The spectra are confined within the bandwidth of the band-pass filter within the ISO2. From the optical spectra measured at the final output (Fig. 3-13(b)) the inter-pulse ASE with the CW pump is higher than that with the pulsed pump in the spectrum range of Fig. 3-13(a). The spectra peak located at 1060 nm is the ASE inputted from the pre-amplifier stage and amplified in the main amplifier. The spectra of the two sidebands are the ASE produced within the main amplifier. The ASE power for CW pump measured is 3.4 times higher than that of pulsed pump. Fig. 3-13(c) shows that the backward ASE monitored at Tap 1, for CW pump it is ~ 3 dB stronger than that of the pulsed pump.

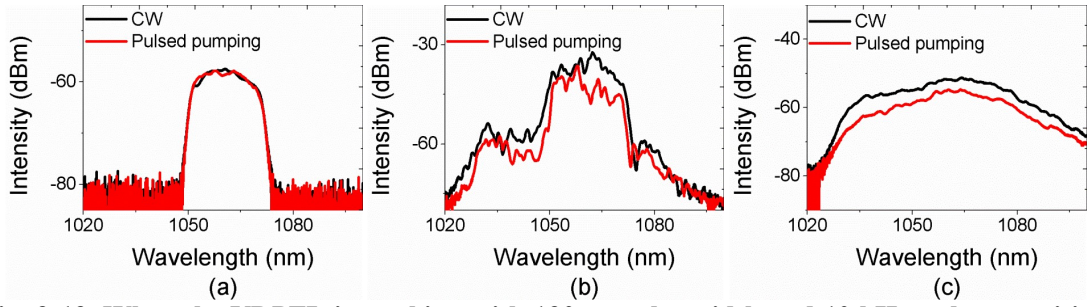


Fig. 3-13. When the YDPFL is working with 130 ns pulse width and 10 kHz pulse repetition rate under the pulsed and CW pumping schemes, the optical spectra measured at Tap2 (a), final output (b) and Tap1 (c) with an AOM to filter out the pulse laser.

Due to the laser pulse is filtered out by the AOM, consequently there is no SRS component in the optical spectra in Fig. 3-13(c). There are two parts contribute to the optical spectra in Fig. 3-13(c) monitored at Tap1. The first one is the backward ASE produced in the main amplifier. The other is the forward light reflected by the surface of the optical components and the fusion point in the main amplifier. The forward light is mainly the ASE injected from the pre-amplifier stage and amplified in the main amplifier stage. To check the amount of these two parts, the following experiment is performed. By tuning the P_P through scaling up the pump current of the pre-amplifier stage, the seeding ASE from the pre-amplifier stage injected to the main amplifier increases (from 86 nW to 117 nW measured at Tap2) as shown in Fig. 3-14(a). The increased ASE is amplified in the main amplifier stage and there should be more back reflection light in Tap1 comparing with the one with 1.36 W P_P . However, from the optical spectra measured at Tap1, it's distinct that there is much less optical spectra density for the one with increased injecting ASE. The ASE power measured at Tap1 is 565 nW and 446 nW when the P_P is 1.36 W and 1.55 W for the pre-amplifier stage respectively. This suggests that the majority light monitored at Tap1 is the backward ASE generated in the main amplifier stage and fairly little part is because of the back reflection. The much lower monitored optical spectrum

after tuning up the injecting ASE is because the stronger injecting ASE from pre-amplifier stage has suppressed the ASE generation in the main amplifier stage.

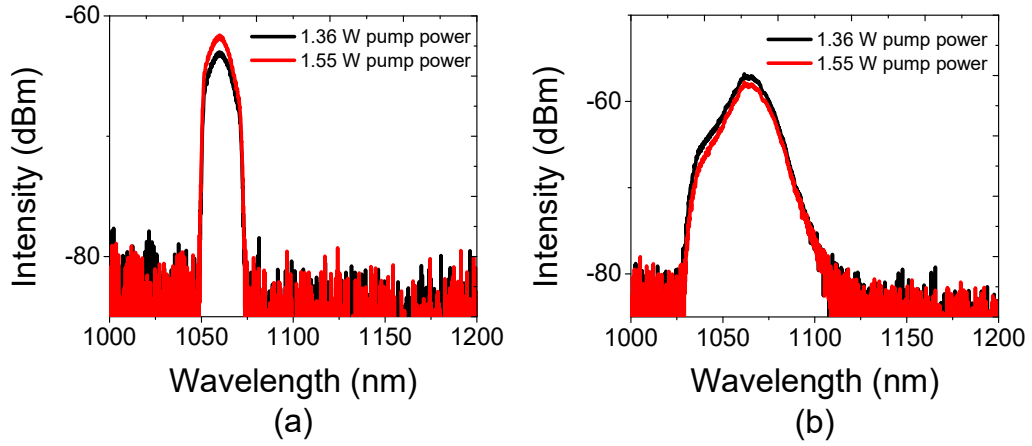


Fig. 3-14. (a) Optical spectra of the forward ASE after pre-amplifier stage by tuning the P_P from 1.36 W to 1.55 W after the pre-amplifier stage. Without pump current for main amplifier stage, the output ASE power injected to the main amplifier from the pre-amplifier stage increases from 4.24 mW to 5.91 mW. (b) Optical spectra monitored at Tap1.

Similar experiments are performed with pulse duration of 20 ns and f_t of 72 kHz. The corresponding t_p is $\sim 13.9 \mu\text{s}$ and the P_P is kept at the maximal reachable 33 W P_P level. When the laser system is working with 20 kHz pulse repetition rate, the optical spectra of the seed and pre-amplifier stage of the 20-ns pulse is shown in Fig. 3-15.

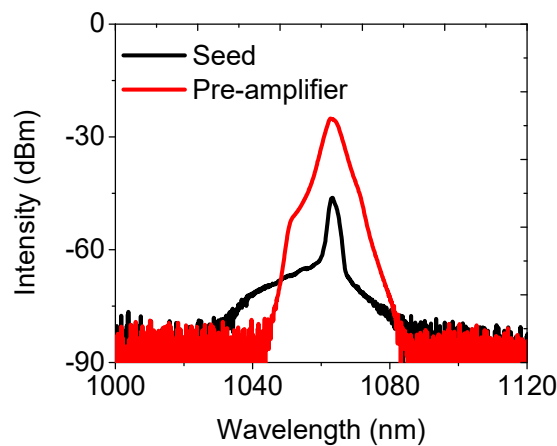


Fig. 3-15. Optical spectra of the Seed and Pre-amplifier stage for the 20-ns pulse.

Fig. 3-16(a) shows the optical spectra measured at final output and Tap 1. Same as the

results of the 130-ns pulse duration, the higher peak power (3.4% improvement) and lower inter-pulse ASE for the pulsed pump scheme are achieved. The average output power is 4.88 W and 5.04 W for the CW pump and the pulsed pump respectively. The efficiency improvement for pulsed pump decreases from ~6% at 5 kHz pulse repetition rate to ~0.7% at 40 kHz comparing with that of CW pump (Fig. 3-16(b)). It also suggests the pulsed pump under f_t (72 kHz) and CW pump above f_t is a suitable design.

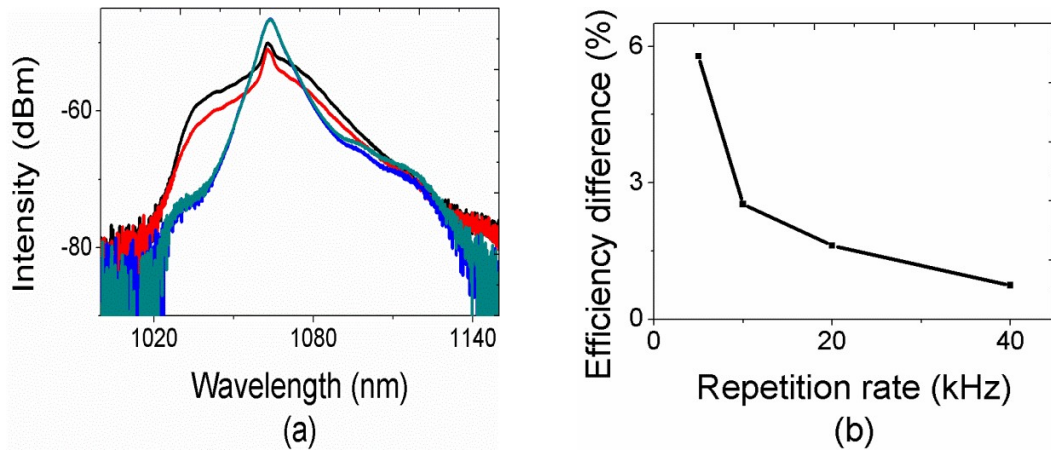


Fig. 3-16. The YDPFL is working with 20 ns pulse width under CW and pulsed pump schemes. (a) The optical spectra from tap1 (the black and red curves are for the CW and pulsed pump respectively) and final output (the blue and dark cyan curves are for the CW and pulsed pump respectively) when the laser system is working with 20 kHz pulse repetition rate. (b) Efficiency difference for the two pumping schemes.

The efficiencies described in this section are obtained by calculating the ratio of the average output power of the YDPFL to the average P_P . The average output power is 7.7 W and 8.01 W for CW pump and pulsed pump respectively when the YDPFL is working with 130 ns pulse duration at 10 kHz pulse repetition rate. For the YDPFL working with 20 ns pulse duration at 20 kHz pulse repetition rate, the output power is 4.88 W and 5.04 W for CW pump and pulsed pump respectively.

Fig. 3-17(a) manifests the temporal pulse shapes of the 130 ns (FWHM) seed pulse and the pulse after the pre-amplifier stage. The pulse shape is distorted, and the leading edge

is higher due to the gain saturation, which makes the gain of the front and rear portions of the pulsed laser unequal. Owing to the merits of directly modulated avenue that the output pulse shape can be tuned through changing the drive current waveform applied to the seed diode. To mitigate the SRS nonlinear effect and to get the final output pulses with higher pulse energy, the shape of the seed pulse is tuned to have a lower leading edge and higher falling edge. In the experiments, the seed pulse shape is tuned to the rectangle-with-triangular-top (RWTT) shape and this part will be further discussed in Section 4.2 and 4.3. The fluctuation around 84 ns on the shape of the seed pulse is due to the un-perfect driving current from the homemade driving circuit board.

Fig. 3-17(b) shows that the pulse shapes are severely reshaped and a sharp peak is formed in the leading edge after the main amplifier stage. The base of the output pulses remains unchanged but the FWHM pulse duration is narrowed down. The pulse duration after main amplifier for the CW pump and pulsed pump is 40 ns and 34 ns respectively. Due to the improved efficiency and higher peak power, the pulse duration obtained with pulsed pump is narrower than that of the CW pump.

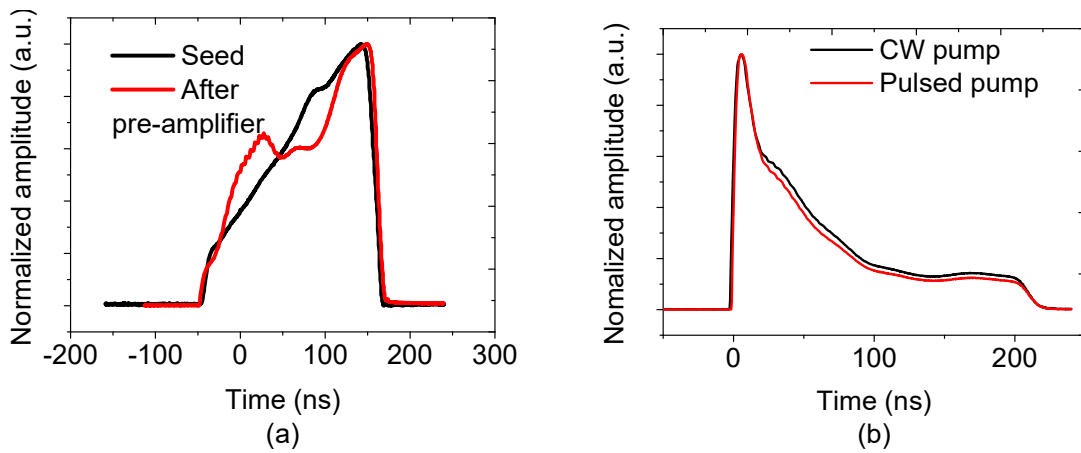


Fig. 3-17. Pulse shapes of 130 ns pulses. (a) The seed pulse (black) and after pre-amplifier stage (red). (b) Pulse shapes of the CW pump (black) and pulsed pump (red) at final output of the YDPFL.

The gain saturation effect is also found for the laser with 20 ns pulse duration. The leading edge of the pulse is steeper after the pre-amplifier and the main amplifier stages as shown in Fig. 3-18. The pulse duration after main amplifier for the CW pump and pulsed pump is narrow down to 9.2 ns and 8.7 ns respectively. Again, the YDPFL pulse with pulsed pump has higher efficiency, larger peak power and narrower pulse duration than that obtained with the CW pump.

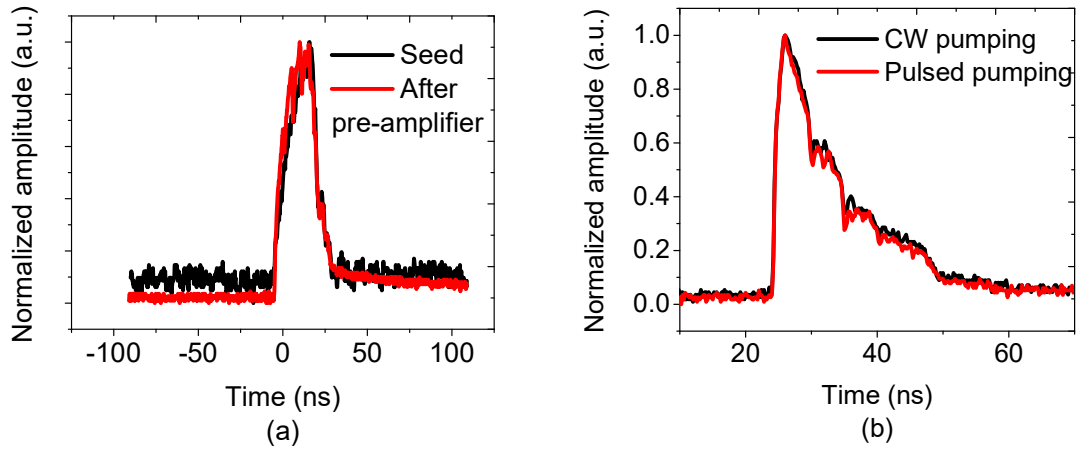


Fig. 3-18. Pulse shapes of 20 ns pulses. a) the seed pulse (black) and after pre-amplifier stage (red). b) Pulse shapes of CW pump (black) and pulsed pump (red) at final output of the YDPFL.

Using the same experimental setup, the simulation results for improved efficiency with pulse pumps at 130 ns and 20 ns pulse duration are shown in Fig. 3-19. The simulation results indicate larger efficiency improvement for pulsed pump at lower pulse repetition rates, which is mainly due to the nonlinearity effects which has not been considered here and the parameters of the components used in the simulation have certain deviations from those in the experiments. However, the trend of the curves is fully consistent with the experimental results.

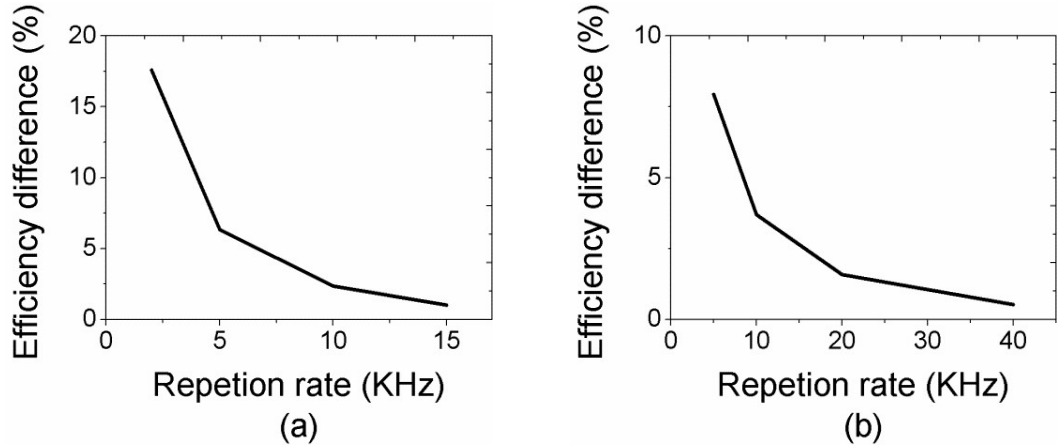


Fig. 3-19. The simulation results of the efficiency improvement for pulsed pump comparing with the CW pump. (a) The YDPFL is working with 130 ns and the pulse repetition rate is less than f_t (25 kHz). (b) The YDPFL is working with 20 ns and the pulse repetition rate is less than f_t (72 kHz).

Larger pulse energy, higher peak power and better efficiency are among the most crucial objectives for the YDPFL design, especially for industrial applications. However, they are also the causes for the stronger inter-pulse ASE and the most often encountered nonlinear effects, such as SRS and SBS as discussed in the previous chapters.

Higher pulse energy requires higher pump energy for each seed laser, which results in a higher inter-pulse ASE under the same conditions. Since ASE is generated in both directions, the heating-related damage to the previous amplifier stage may be caused by the backward-propagating ASE [128]. When the generated ASE is at a high level, parasitic lasers of ~ 1030 nm may damage the components in the laser cavity. For the YDPFL in the experiment, a band pass filter is coated on the lens surface of ISO2 to mitigate the ASE to a certain extent.

For SBS, it is one of the primary peak power capping factors for YDPFLs. It can result in catastrophic fiber damage because of the stress in fiber and the strong acoustic wave as discussed in Chapter 2. For the YDPFL here, the seed laser is generated from an FP laser diode with 3 dB bandwidth of 1.8 nm and peak power of less than 20 kW. The pigtail

length of the component is cautiously controlled. No SBS has been found in the experiments.

When SRS occurs, the laser line width is broadened. It decreases the gain of the signal, generates more heat, and limits the output peak power for an YDPFL. Here, the band pass filter coating within the ISO2 and carefully controlled pigtail length of the components in the main amplifier are utilized to enhance the SRS threshold.

During the laser-material interaction, a portion of pulse energy will be reflected from the surfaces of the material being processed and the surrounding plasma caused by the previous laser pulse. The situation deteriorates when the under-processing materials are Cu, silver and gold etc., with high reflectance for IR laser [129,130]. Fig. 3-20 manifests the typical reflectivity of widely used metals with light at different wavelengths. It is distinct from the curves that gold, silver, aluminum and brass possess high reflectivity when coming to 1 μm wavelength laser.

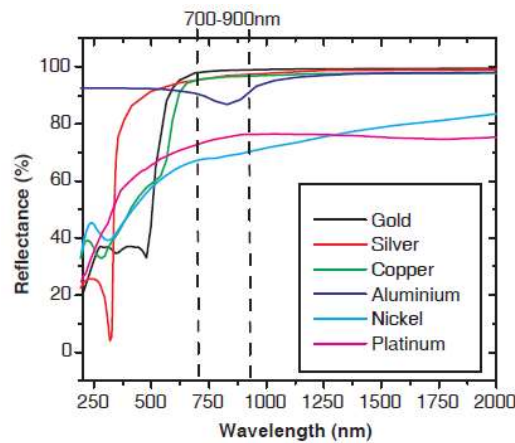


Fig. 3-20. Reflectance of commonly used metals as a function of wavelength from 200 to 2000nm [131].

When back reflection occurs, the reflected light may propagate back to the laser cavity and results in the instability of the output laser pulses. In the case of 5% pulse energy is

reflected to the laser cavity for 20 ns laser pulse at 40 kHz pulse repetition rate, the output pulse energy of the backward pulses exceeds the forward one [120]. The researchers also found that in order to control the energy loss less than 5%, the effective reflectivity need to be controlled at less than 0.1%.

For pulsed fiber lasers, an isolator is often placed at the final output to prevent back-reflected light. For the YDPFL used in the experiment, a band pass filter is coated on the optical lens surface in ISO2 to filter out a portion of the SRS member, but this process results in heating ISO2. Since the Faraday rotators and magnets in the isolators are temperature dependent, temperature changes lead to a change in the Verdet constant, thus affecting the transmission and isolation performances [132]. As isolators are used between amplifiers to prevent the reflected light, the Faraday isolator (FI) by terbium gallium garnet (TGG) is popular used for the YDPFLs [133]. If their performance degrades, the injecting pulse laser from pre-amplifier becomes unstable. The unstable seeding laser may trigger inter-pulse ASE self-lasing in the amplifier. In addition to the TGG absorption band at 480 nm, the transmission spectrum of TGG is broad in the range of ~ 400 nm to ~ 1500 nm [134]. Isolated values for commercially available isolators are typically higher than 30 dB, however, this value typically corresponds to a smaller bandwidth adjacent the center wavelength. The isolation spectrum of FI is usually tens of nanometers for commercially available products [135]. Since the first-order Raman spectrum of the pulsed laser is peaked at ~ 1115 nm, the isolation value decreases quickly when it comes to the ASE and SRS components which are popular for high power YDPFL, and it results in the SRS part a risk factor for YDPFL.

To investigate the effect of back-reflected light on a highly reflective material during

laser processing, the following experiments are conducted. An YDPFL is equipped on a laser system with a Galvo-head, focusing lens and laser control card. The YDPFL has the same MOPA configuration as shown in Fig. 3-9, but the main amplifier uses a different gain fiber (Coractive's 20/128 μm core/cladding diameter). The material in the process is highly polished stainless-steel plate. Fig. 3-21 shows the spectra measured at Tap1 of the YDPFL operating at 20 kHz and 130 ns pulse duration, with different f_t in the experiment. Comparing the black curves and the red curves, when processing the plate, many SRS components are reflected and amplified in the main amplifier stage. The SRS with the f_t of 20 kHz (Fig. 3-21(b)) is much stronger than that of the 28 kHz f_t (Fig. 3-21(a)). The ratio of the signal to ASE peak is ~ 14 dB and ~ 11 dB for the f_t of 28 kHz and 20 kHz, respectively. These suggest that the SRS and inter-pulse ASE are stronger with smaller f_t , and the FI has lower isolation for SRS component.

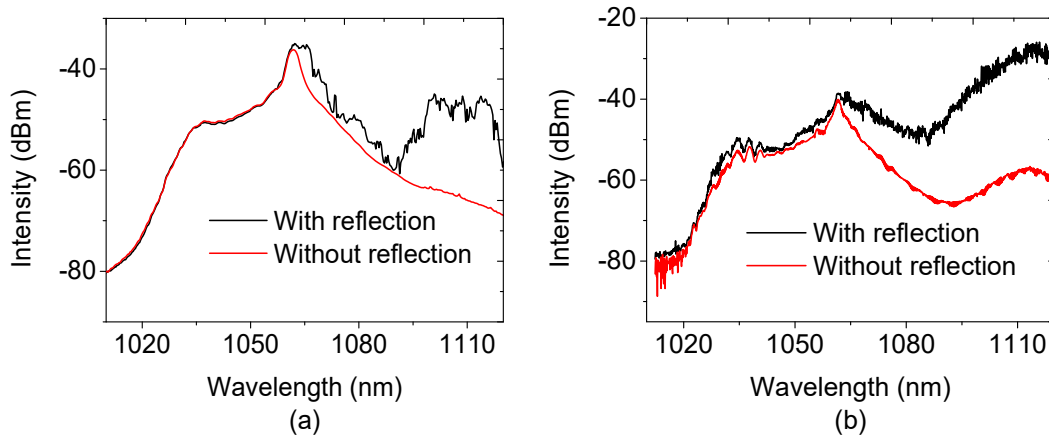


Fig. 3-21. The optical spectra measured at Tap1 with different threshold pulse repetition rates when the YDPFL is working at 20 kHz pulse repetition rate and 130 ns pulse duration. The red and black curves are for the spectra of processing material with very low and high reflective surface respectively. (a) The laser is working with 28 kHz threshold pulse repetition rate (f_t). (b) The laser is working with 20 kHz threshold pulse repetition rate (f_t).

Based on the above analysis, inter-pulse ASE and nonlinear effects (SRS and SBS)

conflict with design goals (higher peak power and efficiency, greater pulse energy, etc.) for YDPFLs for industrial use purposes. These factors should be weighed against during the laser design. Since f_t is directly related to all of it, its value needs to be cautiously determined to achieve a robust YDPFL with superior performance. For the YDPFL used in this section, the f_t is set based on the optical spectrum of the final output laser according to several criteria: a) the ratio of signal to 1st Raman peak is more than 20 dB. b) No higher-order SRS. c) No ASE lasing spike around 1030 nm region. According to all these conditions, the f_t of the 130 ns and 20 ns laser is set at 25 kHz and 72 kHz, respectively.

For other YDPFLs, the designer can determine the f_t according to the laser configurations and the working environment. For amplifier with different gain fiber, of which the fiber core size, length and other parameters are not the same as the one discussed in the above paragraphs, or different pump scheme such as forward pumping, the only difference for the pump design is the f_t for each pulse duration. For laser with several cascade amplifier stages as the pulse energy, ASE and nonlinearity tolerance for each stage are distinct, the f_t and the corresponding t_p for each amplifier stage need to be fine tuned.

For an YDPFL designed for working at low pulse repetition rate with relatively low P_p level, the f_t may be less than 1.25 kHz. When an YDPFL is operating at a low pulse repetition rate, e.g. less than 100 Hz, the t_p may be still long and the ASE is at a relatively high level. When working in this kind of low duty cycle condition, the commercial 9xx nm pumping laser diodes can produce 5~7 times higher output power than operating in the CW mode [123]. This means the maximal P_p level can be raised and the ASE can be

greatly reduced by shortening the t_p .

3.3.3 Conclusion

High power YDPFLs with pulse duration and pulse repetition rate tunable features are desirable for many industrial applications.

In this section, a novel pulsed pump scheme for the YDPFLs with adjustable pulse duration and pulse repetition rate is proposed. By using the optimized pulsed pump scheme, without additional pump or cost, the performance of the YDPFL is improved. For this pulsed pump scheme, the P_p is kept at the maximal reachable pump power level or a fixed level and the t_p for each seed pulse is modulated according to the pulse duration. There is a f_t for each pulse duration to get the maximum average output power with largest pulse energy. For pulse duration, the t_p is fixed for every seed pulse. When the pulse repetition rate is less than f_t , the peak power is enhanced and the inter-pulse ASE is suppressed. The efficiency is improved by ~10% at 2 kHz and ~6% at 5 kHz for wide (130 ns) and narrow (20 ns) pulse duration respectively comparing with using the CW pump scheme. It means that without additional cost, the performance of the laser system is improved. For pulse repetition rate higher than f_t , the inter-pulse ASE is at a low level and it is hardly inevitable to use the pulsed pump by higher P_p and shorter t_p which leads to additional cost. Numerical simulation indicates the same trend as the results of the experiments.

The light reflected during laser-material interaction may propagate back in the laser cavity and result in instability of the output laser pulse. For the SRS and ASE components, they must be cautiously controlled during the YDPFL design because the SRS and ASE components are much less isolated due to their wavelengths are far from the central

operating wavelength of commercial isolators. In addition, the ASE and nonlinear effects (SRS and SBS) conflict with the design objectives (higher peak power and efficiency, greater pulse energy, etc.) of high power YDPFLs. Since f_t is strongly related to nonlinear effects and objectives, the value of it needs to be carefully determined and the criteria for setting f_t are proposed in the context. The pulsed pump design is suitable for the high power YDPFLs with adjustable pulse duration and pulse repetition rate.

3.4 SUMMARY

Pulsed pump is an effective avenue to suppress the ASE between pulses for high power YDPFLs. In this chapter, I focus on the investigation of pulsed pump for YDPFL.

Starting with the analysis of the most crucial factors in pulsed pump YDFA design, P_P and t_p , the simulation model for the pulsed pump YDFA is presented. By numerically solving the rate equations, the pulse energy, efficiency and ASE have been comprehensively studied under different P_P and t_p . The results show that the P_P and t_p are related to the maximum reachable pulse energy and efficiency. Under same P_P , the ASE is at a relatively low level when the amplifier is working with the t_p corresponding to the maximum efficiency. The ASE grows quickly when further increasing the t_p and eventually becomes constant. The laser system can be considered as working in CW mode for ASE under this situation. For different P_P levels, the pulse energy increases with higher P_P . However, the enhancement is not significant after reaching certain level and the pump energy begins to contribute more to the ASE. When the t_p shortening from 6000 μs to 100 μs by keeping the same pump energy of 12 mJ, the stored energy in the gain fiber increases and the peak of the N_2 distribution along the fiber moves towards to the

opposite side of the pumping end. It in turn leads to larger final output pulse energy, from 0.02 mJ to ~2.9 mJ, and higher efficiency, from <0.5% to > 25% when the YDFA operating with t_p shorten from 6000 μ s to 1000 μ s. However, when the t_p is less than 1000 μ s, the increasing is saturated. By increasing the injected seed laser pulse energy from 10 μ J to 50 μ J through enhanced peak power, the output pulse energy and efficiency is improved by 0.34 mJ and 4.5% respectively when the pump duration is shorter than the t_p corresponding to the maximum efficiency. But this doesn't work when the pump duration is longer than the t_p corresponding to the maximum efficiency.

In the second part of this chapter, a novel pulsed pump design for ns YDPFLs with adjustable pulse repetition rate and pulse duration has been proposed. By using this pulsed pump scheme, the P_P is kept at the maximal reachable pump power level or a fixed level and the t_p for each seed pulse is modulated according to the pulse duration. The t_p is a constant value for every seed pulse at particular pulse duration. There is a f_t for each pulse duration to get the maximum average output power with largest pulse energy. When the pulse repetition rate is less than f_t , the peak power is enhanced and the inter-pulse ASE is suppressed. The efficiency is improved by ~10% at 2 kHz and ~6% at 5 kHz for long (130 ns) and short (20 ns) pulse duration respectively comparing with using the CW pump scheme. It means without additional cost, the performance of the laser system is improved. For pulse repetition rate higher than f_t , the inter-pulse ASE is at a low level and it is not recommended to use the pulsed pump by higher P_P and shorter t_p . Numerical simulation indicates the same trend as the results of the experiments. Back-reflected light during laser-material interaction has been investigated and the criteria for setting f_t are proposed.

The novel pulsed pump design is suitable for the high power YDPFLs with adjustable pulse duration and pulse repetition rate. This technique is strongly recommended for the design of robust YDPFLs.

Chapter 4 HIGH POWER YTTERBIUM-DOPED PULSED FIBER LASER

4.1 INTRODUCTION

High power YDPFLs have progressed rapidly and been widely used in lots of fields such as medical, industrial, military and research due to the much superiority associated with them (compact structure, lower heat dissipation, excellent beam quality, etc.). Q-switching and directly modulated LD are the two widely used techniques to generate ns seed laser for high power YDPFLs. The superiority of the fiber laser by the Q-Switching technique is the higher reachable pulse energy. However, the tuning range of the pulse shape and pulse duration of the laser produced by the Q-Switching technique is limited [127]. When the pulse repetition rate is increased, the pulse duration is simultaneously increased, and the peak power of the pulse extracted from the Q-switched system is significantly reduced. In contrast, a system with a directly modulated LD method has the flexibility in terms of adjusting the pulse duration and pulse repetition rate independently, and the peak power of the laser with different pulse duration can be maintained at the same level, which is favorable to many industrial applications.

In this chapter, we first discuss the requirements for the pulse shape of an YDPFL from the application point of view, and then followed by the investigation on the pulse shape of the seed laser. After that, we demonstrate the study on high average power YDPFL with ns pulse duration, and finally a high peak power YDPFL with pulse duration from ps to ns is presented.

4.2 SEED LASER PULSE SHAPING FOR HIGH POWER YTTERBIUM-DOPED PULSED FIBER LASERS

When the laser-material interaction occurs, the energy of the laser pulse whose peak power is higher than the ablation threshold power of the material contributes to the final desired treatment outcomes. The rest of the laser pulse energy is wasted (Fig. 4-1). In addition, this portion of the energy heats the surrounding material and causes damage identified as the heat affected zone (HAZ). In some occasions, at the given pulse energy, the laser with short pulse duration has more usable pulse energy which leading to higher micromachining efficiency and less HAZ.

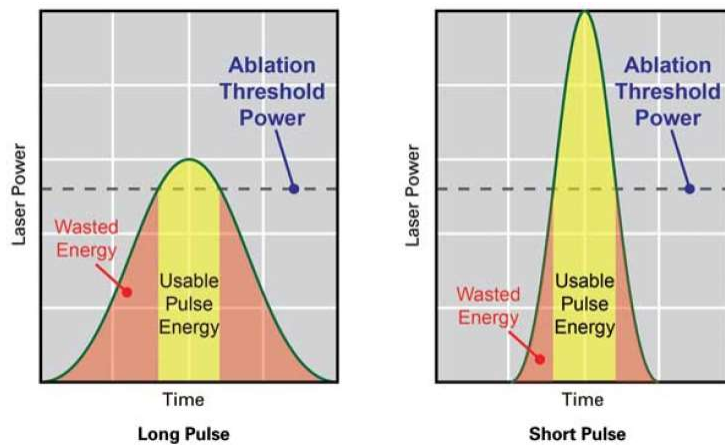


Fig. 4-1. The effect of pulse shape on machining with nanosecond lasers [136].

For laser pulses possessing the same pulse energy and pulse duration, the pulse shapes may be different from each other as shown in Fig. 4-2. When the material ablation threshold is lower the peak power of the laser with rectangular pulse shape, the laser treatment efficiency should be higher than that of the other two pulse shapes as there is no wasted energy. However, if the material ablation threshold power is higher than the peak power of the laser with rectangular pulse shape, then the laser cannot process the material

at all. This is the same for lasers with the other two pulse shapes.

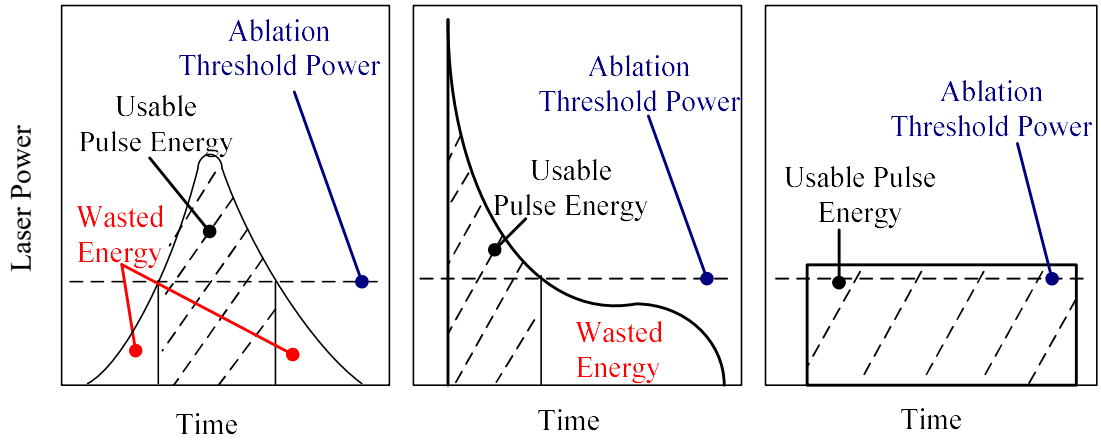


Fig. 4-2. Different pulse shapes with same pulse duration and pulse energy.

There are a few parameters to characterize a high power YDPFL, such as pulse repetition rate, pulse duration, average output power, peak power, pulse energy, beam quality etc., however there is no parameter to directly characterize the situation discussed above as the laser-material interaction is considered.

Driven by this, in this section, a new parameter, Usable Pulse Energy Ratio (UPER), to characterize the laser pulse of high power nanosecond YDPFL is proposed. The high power YDPFL with pulse shaping is analyzed and the nonlinearities associated with the different seed pulse shapes are discussed.

4.2.1 Definition of UPER

The Usable Pulse Energy Ratio (UPER) is defined as the ratio of the pulse energy of the part of the nanosecond laser pulse whose peak power is above a predefined ablation threshold power to the maximum reachable pulse energy. For a nanosecond YDPFL with adjustable pulse duration, as the maximum pulse energy varies with pulse duration, the

UPER is pulse duration related. Obviously, it is also peak power and output power related.

The UPER can be phrased by the following equation:

$$UPER(t_{pd}, P, P_{th}) = \frac{E(t_{pd}, P, P_{th})}{E_{max}(t_{pd})} \times 100\% \quad (4.1)$$

Where t_{pd} , P and P_{th} are the pulse duration, output power and ablation threshold power respectively. $E(t_{pd}, P, P_{th})$ is the pulse energy of the part of pulse whose peak power is higher than the ablation threshold power (P_{th}) at the output power level of P . $E_{max}(t_{pd})$ is the maximum reachable pulse energy for the laser with t_{pd} pulse duration. Through this parameter, we perceive qualitatively whether the workpiece can be laser processed or not, how much pulse energy is wasted, and how wide the HAZ is after laser treatment.

From the laser processing point of view, the rectangular pulse shape of the final output laser with peak power higher than the material ablation threshold is preferred as no waste energy and thus fewer side effects such as less HAZ.

Since the peak power of the ns YDPFL can easily reach higher than 10 kW, the shape of the laser pulse suffers from severe distortion due to the gain saturation effect as described in Chapter 2 when the laser pulse propagates in the waveguide of the fiber [67,137]. For high power YDPFL design, it is indispensable to study the pulse shape of seed laser.

4.2.2 Pulse shape distortion for high power Ytterbium-doped pulsed fiber lasers

Q-switching and directly modulated LD are the two widely utilized techniques to generate ns seed laser for high power YDPFLs. For Q-switched seed laser and an AOM is used as the Q-switching component, the seed and final output pulse shapes are more Gaussian-like and less pulse shape distortion occurs due to the normally slow and smooth leading and falling edge of the seed pulse. For YDPFLs with directly modulated LD

technique to produce the seed pulse laser, the arbitrary pulse shape can be easily achieved by modulating the shape of the drive current. Researchers have analyzed this feature through experiments and numerical simulations [137,138]. The Frantz-Nodvik (F-N) equation can be used to calculate the pulse shape distortion in an amplifier [139], and when the desired output pulse shape is determined, the input pulse shape can be calculated inversely using the equation.

For a high power YDPFL, the pulse duration is adjustable or not depending on the technology for producing seed laser. For ns YDPFL with tunable pulse duration, as a rule of thumb, the peak power of the laser with different pulse duration keeps at a similar level due to the two dominant nonlinearities for ns YDPFL, SBS and SRS, are directly related to the peak power.

To study the pulse shape distortion of high power YDPFLs, an MOPA YDPFL with a central wavelength at 1064 nm is configured in Fig. 4-3 and a directly modulated seed laser diode (LC96A1064BBFBG-20R) is utilized to produce nanosecond pulse with tunable pulse duration and repetition rate. The seed laser diode from Oclaro has a 1W peak output power at 2A drive current. The core/cladding diameters of the DCF used in the pre-amplifier and power amplifier stages are 6.6/128 μm and 21.7/128 μm , respectively, and the lengths were 6 m and 4.4 m, respectively. In between the seed diode, the pre-amplifier stage and the main amplifier, there are isolators to prevent the reflecting light. A coupler (1/1000 coupling ratio) is used to monitor the backward light from the main amplifier cavity via port Tap1. An isolator with collimator embedded is spliced to the pigtail of the main amplifier to prevent the fiber facet damage and the back-reflection light during laser treatment. In the following experiments, the pulse duration used is 200

ns (measured at the base of the pulse).

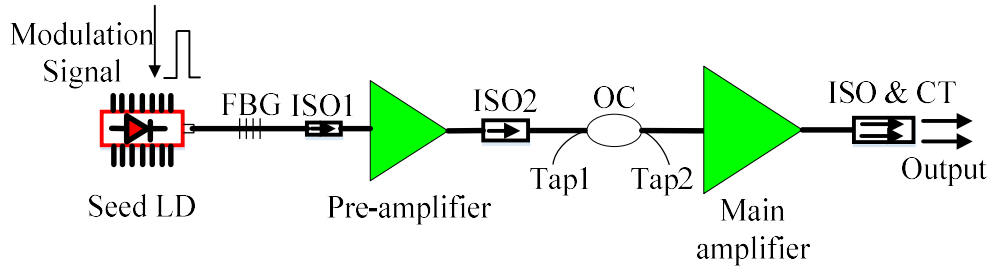


Fig. 4-3. Structure of the MOPA fiber laser system (FBG: fiber Bragg grating, ISO: isolator, OC: optical coupler, CT: collimator).

When the laser pulses from the seed laser diode pass through the cascade amplifier stages in a MOPA configuration system, the laser pulse energy and the peak power are significantly boosted. At the same time, the pulse shape has more distortion. Fig. 4-4 shows the pulse shapes of the laser when a rectangular shape seed laser pulse is used with a pulse repetition rate of 100 kHz. The average output laser power of the seed, after pre-amplifier and main amplifier stage is 3 mW, 296 mW and 21.2 W (100% output), respectively. From the curves, the pulse shape distortion after pre-amplifier is not significant. This is understandable as the input seed signal is small and quite little gain saturation effect occurs in the pre-amplifier stage such that the rear portion of the laser pulse has acquired most of the energy required for amplification.

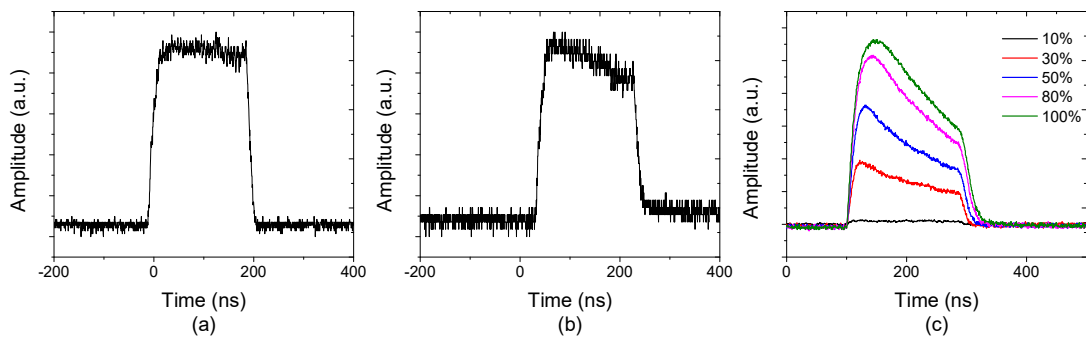


Fig. 4-4. For the rectangular shape of seed laser, pulse shape of the seed laser (a), after the pre-amplifier stage (b) and main amplifier stage (c) at 10%, 30%, 50%, 80% and 100% output power scale.

Fig. 4-4(c) shows the pulse shapes after the main amplifier stage at different power levels and the distortion at low output power level is almost negligible. When the power reaches 6.3 W (30%), there is significant distortion of the pulse shape and the leading edge becomes steeper resulting in a peak. As the power increases, the distortion is more serious.

4.2.3 Pulse shaping for Ytterbium-doped pulsed fiber lasers

From the discussion in the above, the leading-edge surges after main amplifier stage for the rectangular seed pulse shape. To compensate the low gain for the rear part of the seed laser pulse, it's obviously a lower leading-edge pulse is desirable. In the following experiments, seed laser with three different pulse shapes, rectangular shape, rectangle-with-triangular-top (RWTT) shape, and triangular shape, is investigated with the laser system shown in Fig. 4-3 with 20.3 W output average power at 35 kHz pulse repetition rate. The seed pulse shaping is realized through adjusting the driving current pulse shape from a homemade circuit board at a step of 10 ns and this is the same for all the seed pulse shaping in this thesis. The laser pulse shapes of the seed and after the main amplifier stage are shown in Fig. 4-5 and Fig. 4-6, respectively. As expected, the leading edge of the final output laser is sharpened and surged with high peak power even with pulse shaping at seed.

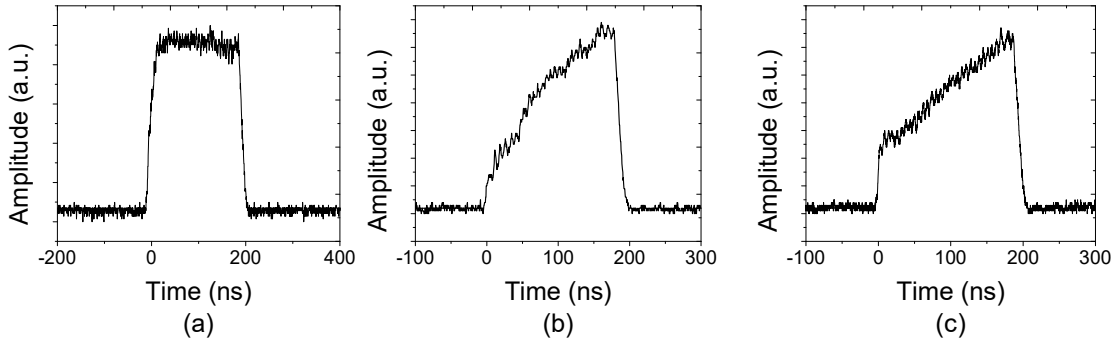


Fig. 4-5. The pulse shapes of the seed laser. (a) Rectangular shape, (b) triangular shape, (c) RWTT shape.

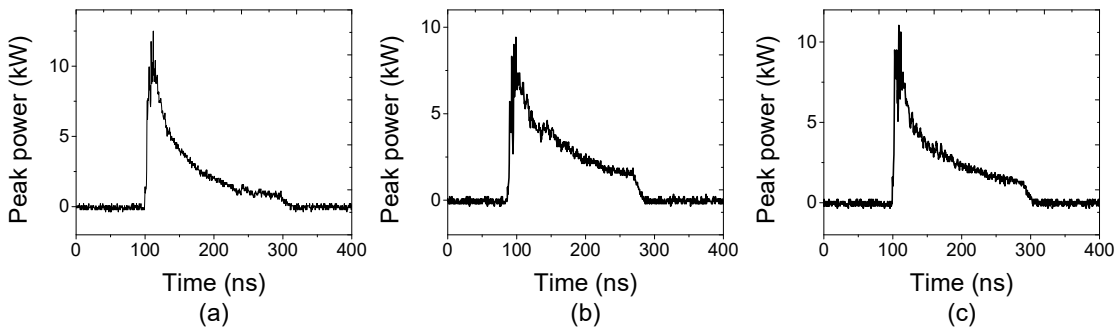


Fig. 4-6. Pulse shapes of the laser with (a) rectangular, (b) triangular, (c) RWTT seed pulse shapes at final output with 20.3 W output power and 35 kHz pulse repetition rate.

As expected, at the given pulse energy of 0.58 mJ, the laser with low leading edge has lower peak power and it is 12.5 kW, 11 kW and 9.4 kW for the laser with rectangular, RWTT, and triangular seed pulse shapes, respectively. Accordingly, the UPER for the laser with triangular and rectangular shapes is lower when the ablation threshold power is higher than 3 kW (Fig. 4-7). However, when at the lower ablation threshold power such as 2 kW, the UPER is 70.3% for the laser with triangular seed pulse shape which is $\sim 5\%$ higher than that of the rectangular seed pulse shape. The UPER for the laser with triangular seed pulse shape is higher than that of the RWTT one when the ablation threshold power is less than ~ 4.6 kW.

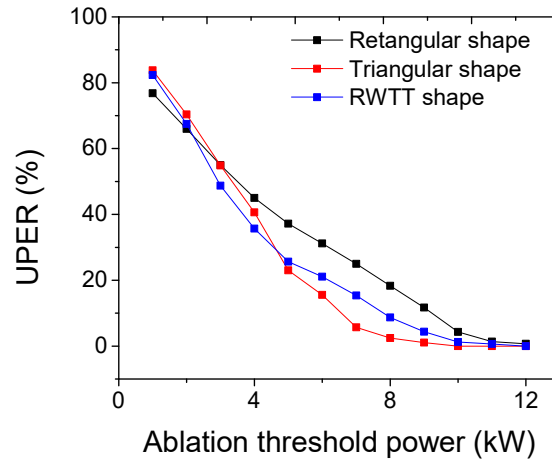


Fig. 4-7. UPER at different ablation threshold power for the YDPFL with rectangular, triangular and rectangle-with-triangular-top shapes.

As discussed in Chapter 2, the SRS and SBS are the two major limiting factors for high power YDPFLs and both are directly related to the peak power of the laser. SRS generally reduces overall optical conversion efficiency and broadens the spectrum. As a result, the SRS of the laser with rectangular seed pulse shape at ~ 1115 nm is higher than that of the other two shapes. This can be found from the optical spectra monitored at the final output and Tap1 shown in Fig. 4-8. The laser with triangular shape has the lowest SRS component. The SRS difference between the laser with rectangular and triangular seed pulse shapes is ~ 2.5 dB and ~ 5.7 dB for the forward and backward SRS respectively. As discussed in Section 3.3.2, due to the limited bandwidth of the Faraday isolator implemented in high power YDPFLs and the light reflected during the laser processing, the SRS is one of the major concerns and must be cautiously controlled.

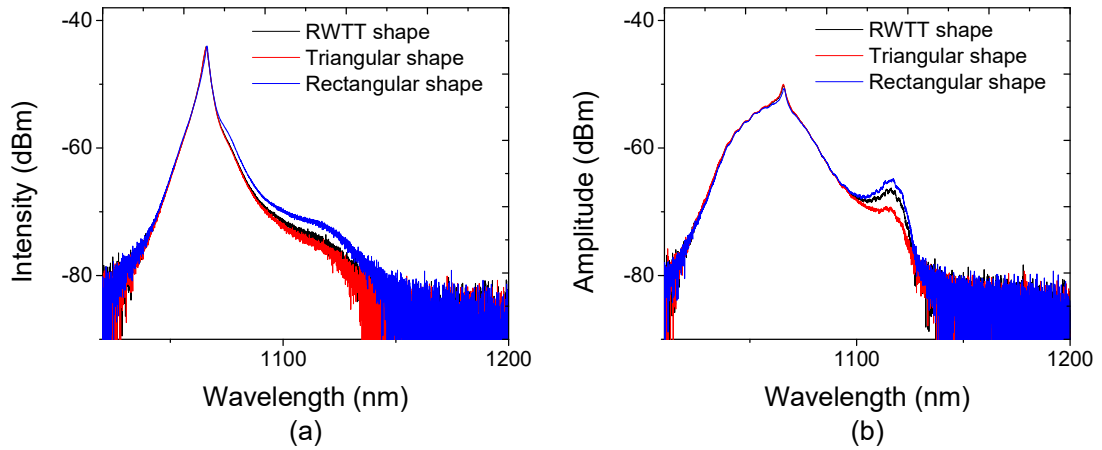


Fig. 4-8. Optical spectra measured at the final output (a) and Tap1 (b) for the laser with three different seed pulse shapes.

The SBS gain factor ($\sim 5 \times 10^{-11}$ m/W for a silica-based fiber) is about three orders of magnitude higher than that of the SRS, and it causes the SBS to occur more frequently for high power YDPFLs [140]. SBS is a killing factor for high power YDPFL as it consumes the upper-level populations during the backward propagation along the gain fiber. As a result, the seed laser to inject into the subsequent amplifier becomes weaker and ASE self-lasing may occur in that amplifier stage. Huge ASE self-lasing pulses are the frequently encountered accidents for permanently damage the laser cavity during our experiments. As described in Chapter 2, the frequency shift of SBS is 0.088 nm for a 1.06 μm wavelength laser. Since the 3-dB spectral bandwidth of the signal laser is 3 nm in the experiments, the SBS spectrum having such minuscule offsets overlaps with the signal spectrum and it is formidable to distinguish the SBS component from the optical spectrum via an optical spectrum analyzer (OSA). To study the SBS for the laser with different seed laser pulse shapes, the SBS spike is examined by an oscilloscope via a photo detector in the following experiments. When SBS occurs, the SBS spike can be monitored from Tap1 as shown in Fig. 4-9. However, if the amplitude of the SBS spike is less than the signal

laser pulse, it also cannot be figured out.

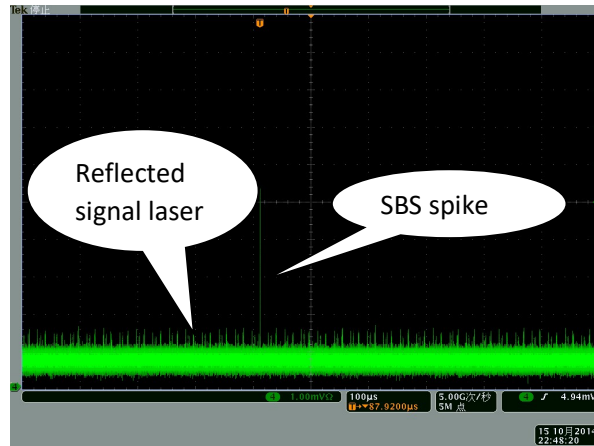


Fig. 4-9. SBS spike in a pulse train.

The SBS for the laser with triangular and RWTT shapes is studied in the experiments. The SBS is triggered by the oscilloscope when the height of a SBS spike is five times higher than that of the reflected signal laser monitored at Tap1. The experiments are performed when the laser is operating at 200 ns, 35 kHz repetition rate and 7.1 W output average power. The peak power is ~ 1.6 kW and ~ 1.4 kW for the laser of RWTT and triangular seed pulse shapes respectively. From the results shown in Table 4-1, the SBS spike occurs frequently for laser pulse with triangular shape although a lower peak power is associated with this laser pulse, and none is found for the laser with RWTT seed pulse shape.

Table 4-1. The statistics of the SBS spikes captured by the oscilloscope in the experiments within 5 minutes.

Pulse shape	Testing period	How many times SBS captured
Rectangle-with-triangle-top-shape pulse	5 minutes	0
Triangle-shape pulse	5 minutes	131

When the leading edge of the laser pulse is a smooth curve, the frequency spectral width of the Fourier transform of the leading edge is narrow and the narrow frequency spectrum significantly deteriorates the threshold of the SBS [141]. Fig. 4-10(a) manifests that the frequency spectra of rectangular and Gaussian shapes are ~ 7 GHz and less than 0.1 GHz, respectively. The relationship between the SBS threshold and the rising time is shown in Fig. 4-10(b) [141] and it is manifest slower rising time leads the decreasing of the SBS threshold.

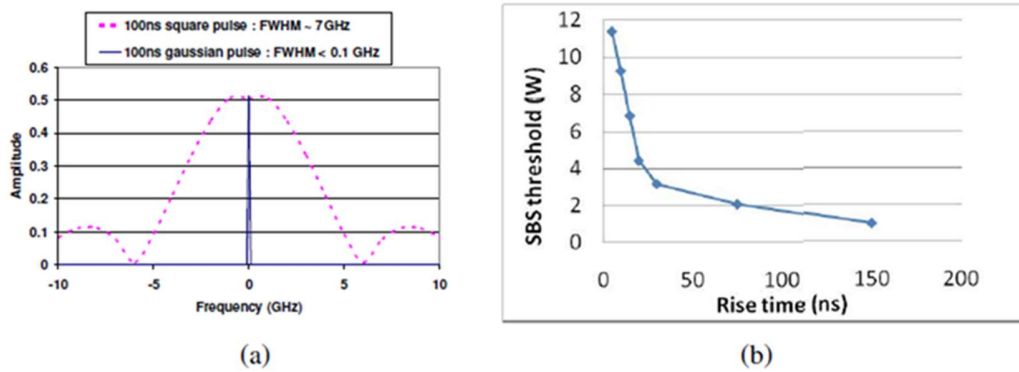


Fig. 4-10. (a) The frequency components of the rectangular and Gaussian shape laser pulses. (b) The relationship between rising time and SBS threshold.

From the above discussion, the smooth rising edge of the triangular shape has a narrow frequency spectrum, which results in a lower SBS threshold. Fig. 4-11 shows the pulse shapes of the laser from the seed, after the pre-amplifier, at the final output and Tap1 with and without SBS spike. The laser is with a triangular seed pulse shape.

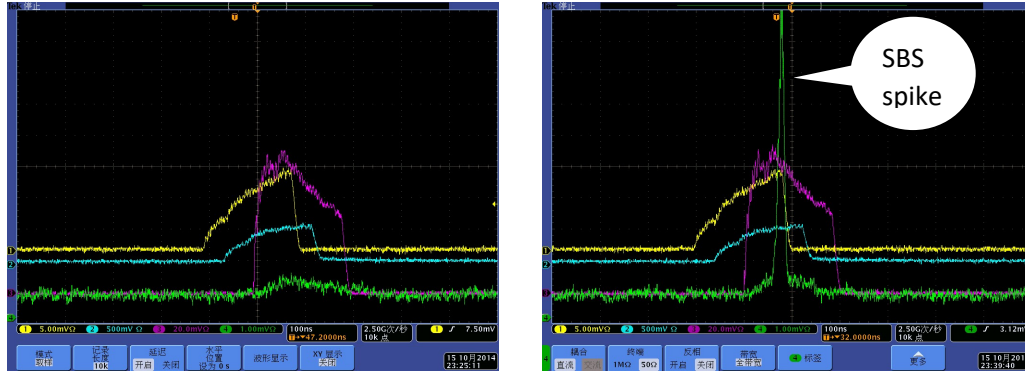


Fig. 4-11. The pulse shapes of the laser from the seed (yellow), after the pre-amplifier (cyan) and main amplifier (purple), and at Tap1 (green). The images in the left and right are for the YDPFL operating at the moment without and with SBS spike, respectively.

4.2.4 Conclusion

From the perspective of laser-material interaction during laser processing, the energy of the laser pulse whose peak power is higher than the ablation threshold power of the material contributes to the final desired treatment outcomes. The rest of the laser pulse energy is wasted and forms the HAZ.

For a high power YDPFL with directly modulated seed source, the pulse shape of the seed laser can be easily turned. The different laser pulse shapes result in different laser processing efficiencies.

To characterize the laser pulse by considering the laser-material interaction, a new parameter, Usable Pulse Energy Ratio (UPER), is proposed. The UPER is defined as the ratio of the pulse energy of the part of the nanosecond laser pulse whose peak power is higher than the predefined ablation threshold power to the maximum reachable pulse energy. It is related to ablation threshold power, peak power, pulse duration, and the output power. Through this parameter, we understand qualitatively whether the workpiece can be laser processed or not, how much pulse energy is wasted, and how wide the HAZ is after laser treatment.

A high power YDPFL with three seed pulse shapes, rectangles, triangles and RWTT shapes have been experimentally investigated. Because of gain saturation, the shape of the final output laser is seriously distorted, and the leading edge of the pulse is surged to form high peak power. At a given pulse energy of 0.58 mJ, the laser with a low leading edge has a lower peak power and the peak power is 12.5 kW, 11 kW and 9.4 kW for the laser having a rectangular, RWTT and triangular seed pulse shape respectively. When the ablation threshold power is higher than 3 kW, the UPER of the laser with triangular and RWTT is lower. However, the UPER grows to 70.3% for a laser having a triangular seed pulse shape and it is about 5% higher than that of the rectangular seed pulse shape at an ablation threshold power of 2 kW.

In addition to the undoubted superiority of pulse shaping such as the higher UPER at low ablation threshold power and less SRS components, when the leading edge of the seed pulse rises slowly and smoothly, such as a triangular shape, it gives rise to another dilemma, SBS. The smooth rising edge of the triangle has a narrow frequency spectrum, and leads to a significant deterioration of the SBS threshold. SBS spikes are captured frequently for the laser with triangular seed pulse shape. However, for the seed laser with RWTT shape, no SBS has been found in the experiment

According to the analysis here, in Section 3.3.2, seed laser with the RWTT pulse shape is utilized for higher pulse energy and less SRS component, at the same time SBS is not an issue. In the following sections of high power YDPFL design, seed laser having a pulse shape similar to a triangular shape is selected to improve the laser performance.

4.3 HIGH AVERAGE POWER YTTERBIUM-DOPED PULSED FIBER LASER

For material processing, general speaking, higher average power YDPFL means higher efficiency as the laser scanning speed could be enhanced. This also can be concluded from the laser blackening the Aluminum alloy with alumina surface application in Chapter 5. As efficiency is one of the most crucial factors for industrial applications, driven by this force, the progress of high average power YDPFL has been quick.

From the discussion in Section 4.2, the final output laser with square pulse shape is desirable and contributes to the processing efficiency during laser-material interaction. Due to the high gain in the YDPFL and gain saturation effect, the seed laser with lower leading edge is preferred, such as the triangular shape pulse and RWTT pulse. However, due to the deterioration of the SBS threshold, the slow leading-edge results in frequent SBS spike in the laser cavity. To address this issue, an SLED seed diode is used for the high average power YDPFL due to its bandwidth of the optical spectrum is much wider than that of the conventional DFB and FP sources. Since the SBS threshold is roughly proportional to ω_s/ω_b , where ω_s and ω_b are the bandwidth of fiber laser emission and SBS interaction, the maximum SBS-free power is increased due to the wider bandwidth and decreasing spectral power density of the laser radiation [142].

4.3.1 Configuration of the Ytterbium-doped pulsed fiber lasers

The configuration of the nanosecond high average power YDPFL is shown in Fig. 4-12. A directly modulated SLED seed diode (LC96A1060CWG-20R from II-VI Inc.) from II-VI is used to produce nanosecond seed laser with tunable pulse repetition rate and tunable pulse duration. The SLED has a curved waveguide with reflectance of 0.1% and 93% for the front and back facets, respectively. The low antireflection coating on the front facet

and the curved-waveguide design are to prevent the light from FP oscillation [142]. The light emission process is based on the SLED operates in the superluminescent regime and the coexistence of spontaneous and stimulated emissions [143]. The broad and smooth optical spectrum provided by the spontaneous emission is amplified by stimulated emission processes (this mechanism is called amplified spontaneous emission (ASE)), and the ASE light is used as the seed for the YDPFL. The average output power is ~ 380 mW at 750 mA pumping current, and no DC bias is applied to the seed diode in the experiments. The optical spectra of the seed diode for different pulse duration at certain pulse repetition rate are shown in Fig. 4-13. 1.8A current is applied to the SLED to generate seed light from a home-made circuit board. It is obvious the seed diode is operating at the ASE region without lasing. With higher current operation (the product of pulse duration times pulse repetition rate), the peak wavelength is shifted to the longer side. The 20-m-length Hi1060 fiber is spliced to the pigtail of the seed diode to ensure the diode is in the laser-off condition when there is backward reflection light from the surface of the material under processing.

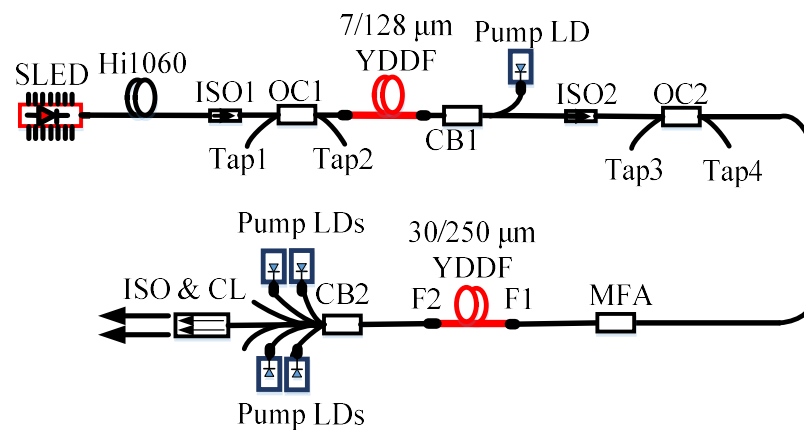


Fig. 4-12. Experimental setup of a nanosecond MOPA pulse fiber laser. SLED: superluminescent light emitting diode, ISO: isolator, OC: optical coupler, MFA: mode field adapter, CB: combiner, CL: collimator, F1: splicing point 1, F2: splicing point 2.

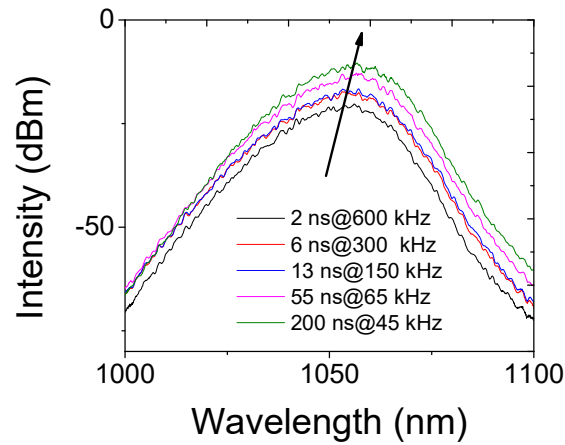


Fig. 4-133. The optical spectra of the SLED seed diode when operating at different pulse duration and pulse repetition rate.

The pre-amplifier stage which consists of a $(1+1)\times 1$ combiner and a 13-meter-long YDF is used to boost the seed laser pulses from the seed diode with the backward pump scheme. The core/inner cladding diameter and NA of the gain fiber are $7/128\ \mu\text{m}$ and $0.19/0.46$ respectively. The inner cladding absorption is $1.3\ \text{dB/m}$ at $915\ \text{nm}$ wavelength. One $960\ \text{nm}$ multimode LD with maximal $10\ \text{W}$ output power is used for this stage.

The structure of the main amplifier is similar as that of the pre-amplifier. The ~ 7 -meter-long gain fiber with core/inner cladding diameter of $30/250\ \mu\text{m}$ is used for this stage. The fiber core NA is 0.05 and the inner cladding absorption of the YDF is $2\ \text{dB/m}$ at $915\ \text{nm}$ wavelength. One $(6+1)\times 1$ combiner is used to couple the maximal $280\ \text{W}$ pump power from four multimode LDs at $915\ \text{nm}$ into the amplifier.

To enhance the optical-to-optical conversion efficiency, the backward pump scheme is used for both the pre- and main amplifier stages. The main difference from the configurations of the YDPFLs in the previous sections is that an SLED is used instead of the FP laser diode to generate seed light with a broadband optical spectrum.

Two fiber pigtailed isolators (ISO1 and ISO2) are equipped to block the counter-propagating light after the seed diode and the pre-amplifier stage. The band-pass film with 18 nm FWHM bandwidth centered at 1060 nm is coated on the optical lens surface within the isolator to filter out the ASE and the stimulated Raman scattering (SRS) optical spectrum components. Two optical couplers (OC) with optical power splitting ration of 0.1% : 99.9% from Lightcomm are used to monitor the forward and backward signal in the laser cavity located after the ISO1 and ISO2.

As for surface damage, in general facet is more fragile. The dirt on the fiber facet and irregularities of the facet dramatically reduce the damage threshold. The approximate surface damage threshold of fused silica fiber can be obtained by the following equation for 1064 nm laser [144]:

$$FD_{th} = 22(\Delta\tau_p)^{0.4} J/cm^2 \quad (4.2)$$

Where FD_{th} is the damage threshold of the fiber facet and $\Delta\tau_p$ represents the pulse duration in ns. For the 80-ns laser pulse, the facet damage is ~ 0.9 mJ for the 30 μm fiber core. As the output pulse energy is higher than the facet damage threshold, to prevent the fiber facet, a collimator with isolator embedded is spliced to the output fiber of the main amplifier. The output beam size of the laser is expanded to ~ 6 mm.

The laser with pulse duration (FWHM) of 10 ns, 34 ns, 56 ns and 80 ns are selected to study the YDPFL. The pulse repetition rate can be adjusted from single shot to 1 MHz. The optical spectra are measured by YOKOGAWA AQ6370C and the pulse shapes are measured by Tektronix DPO4104B-L via a 1 GHz photo detector (PD) in the following experiments.

4.3.2 Discuss on the seed and cascade amplifier stage

The MOPA configuration is popular for high power pulsed fiber lasers and the laser pulse is gradually boosted by several cascaded amplifiers. The output lasers after each amplifier stage can be monitored and tuned to operate under safe conditions. As discussed in Section 3.3 the pulsed pump avenue can be used to improve the efficiency and suppress the inter-pulse ASE for a high power YDPFL with adjustable pulse duration and pulse repetition rate, it has been utilized for this laser. By using the same criteria: no ASE lasing spike at ~ 1030 nm, no higher order SRS component and minimum 20 dB for the ratio of signal peak to SRS at ~ 1115 nm, the threshold pulse repetition (f_i) rate is set at 110 kHz, 170 kHz, 300 kHz and 1100 kHz for the laser with pulse duration of 80 ns, 56 ns, 34 ns and 10 ns respectively.

Fig. 4-14 shows the pulse shapes and optical spectra of the seed laser with different pulse duration at f_i . As discussed in Section 3.1, the pulse shape of the final output pulsed high power laser is significantly distorted due to the gain saturation effect. In order to minimize this effect and the wasted pulsed energy during laser processing, the pulse shape of the seed laser pulse is carefully adjusted by tuning the driving current to the seed diode. In Fig. 4-14(a), the leading edge of the pulse is obviously smoothed compared to the rectangular pulse. Fig. 4-14(b) shows that the 3-dB bandwidth of the seed laser spectrum is ~ 11 nm which is much wider than that of a FP (1.8 nm for the FP diode used in the experiments of Chapter 3) or DFB (normally less than 1 nm) laser diodes and the seed laser spectrum is similar over different pulse duration.

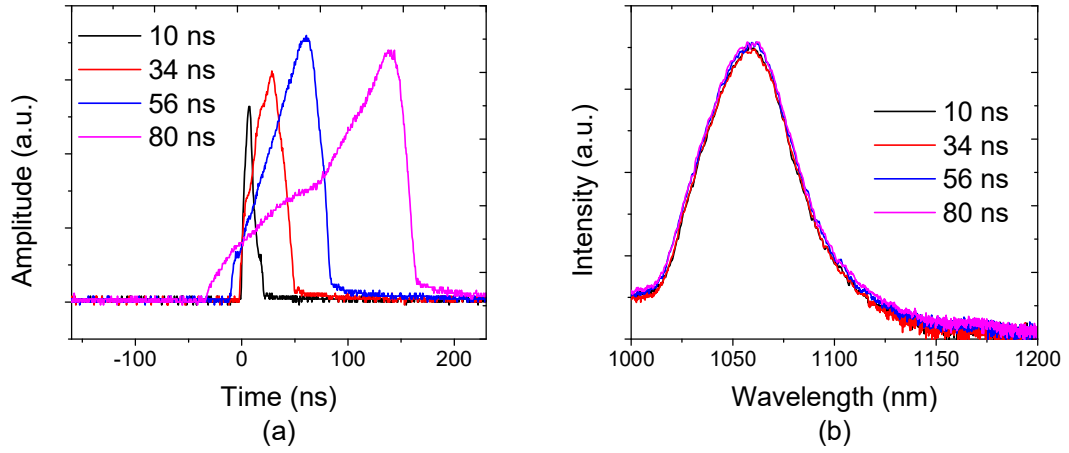


Fig. 4-14. The pulse shapes (a) and the optical spectra (b) of the seed laser of the YDPFL.

The average output power of the YDPFL after ISO2 is more than 600 mW for the laser with the four pulse durations at pulse repetition rates of 1100 kHz, 300 kHz, 150 kHz and 110 kHz, respectively. From the pulse shapes shown in Fig. 4-15(a), the pulses with longer pulse duration suffer more distortion for the pulse shape. The optical spectra shown in Fig. 4-15(b) shows the optical spectra at 3 dB of ~ 8 nm for the laser with the four pulse durations. Compared to the spectrum of the seed laser, the optical spectra here is narrower due to the ASE filter embedded in the ISO2 whose bandwidth is narrower than that of the seed laser.

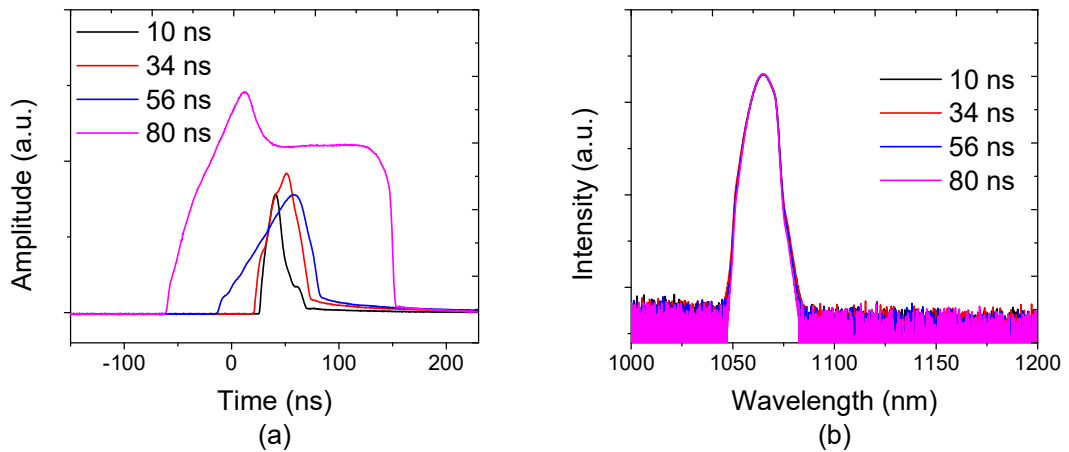


Fig. 4-15. The pulse shape (a) and the optical spectra (b) of the pre-amplifier stage of the YDPFL.

The pulse energy of the laser with 80 ns, 56ns, 34 ns and 10 ns pulse duration is 1.45 mJ, 0.94 mJ, 0.45 mJ and 0.14 mJ, respectively. Fig. 4-16(a) shows the pulse shape and peak power of the final output laser. The peak power is in the range of 15.3 kW to 17.3 kW for the laser of four pulse duration. Fig. 4-16(b) shows the UPERs for the laser with 34 ns seed pulse duration are higher than that of the others when the ablation threshold power is higher than 8 kW. When the ablation threshold power is less than 5 kW, the laser with 80 ns has the higher UPERs. During laser-material interactions, it suggests there are less wasted energy and thus narrower HAZ when choosing the laser parameters with these higher UPERs.

During the laser-material interaction, the energy of the laser pulse will first be partially reflected and absorbed by the surrounding plasma layer or particles produced during the laser-material interaction of the previous laser pulses. The remaining laser pulse energy will reach the surface of the material being processed (MUP), and a portion thereof will be reflected again by the material surface. Finally, the remainder contributes to the desired laser treatment. Due to the different pulse energy (1.45 mJ, 0.94 mJ, 0.45 mJ and 0.14 mJ for the laser with 80 ns, 56 ns, 34 ns and 10 ns pulse duration respectively) and energy wasted for processing the plasma, the laser treatment efficiency is subject to verify with the material [145].

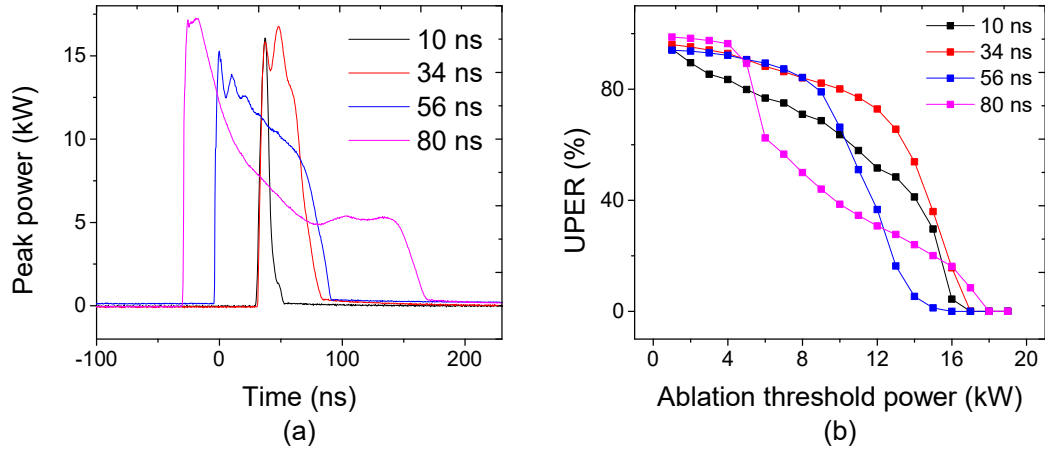


Fig. 4-16. (a) The peak power of the YDPFL pulse with different seed pulse duration. (b) UPERs at different threshold with several different seed laser pulse durations.

Comparing the YDPFL with 80 ns triangular seed pulse shape here with the one in Section 3.3.2 with 183 ns RWTT seed pulse shape (Fig. 4-17(a) and (b)), the peak power and pulse energy of the final output laser for the triangular and RWTT seed pulse shapes are 17.3 kW/1.45 mJ and 14.5 kW/0.8 mJ, respectively. The base of the laser pulse of the two YDPFLs is the same of 200 ns. The reason behind for using the RWTT shape instead of the triangular pulse shape used there is that the SBS cannot be eliminated for the YDPFL having the FP seed laser. For YDPFLs with long pulse duration, for example where the laser has a slow falling edge and a long tail with low peak power, this may result in stronger thermal effect and a wider HAZ during laser processing. From the curves in Fig. 4-17(c), the laser with triangular seed pulse shape here has higher UPERs at all ablation threshold power levels than that of the RWTT one.

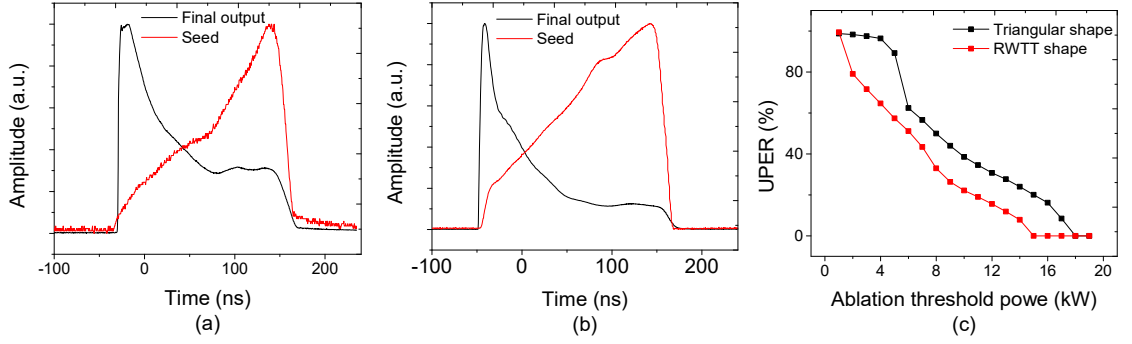


Fig. 4-17. The pulse shape of the seed and final output with triangular (a) and RWTT seed pulse shape (b). (c) UPERs for the YDPFLs with triangular and RWTT seed pulse shapes at different threshold.

From Fig. 4-18(a) the optical spectra are wider with higher average output power for the 80-ns pulse and the 3-dB spectrum bandwidth is ~ 10 nm. Comparing with the 3-dB spectrum width of the pulsed laser before injecting the main amplifier which is ~ 8 nm, there is a spectral broadening factor of 1.25 which is mainly due to the SPM [146]. The SPM-induced optical spectral broadening in glass fiber can be estimated by the following equations:

$$\varphi_{NL} = \frac{2\pi n_2}{\lambda A \Gamma^2} P_0 L_{eff} \quad (4.3)$$

Where φ_{NL} is the maximum nonlinear phase shift and n_2 represents the nonlinear index coefficient of $2.2 \times 10^{-20} \text{ m}^2/\text{W}$. λ is the laser wavelength and A is the fiber core area. $\Gamma = 0.8$ is the filling factor for signal laser. $P_0 = 38 \text{ W}$ is the peak power of the laser injecting into the main amplifier. L_{eff} can be obtained by the following equation [64]:

$$L_{eff} = \frac{1 - \exp(-\alpha L)}{\alpha} L \quad (4.4)$$

Where α is the loss of pump signal propagating in the fiber and L is the fiber length which is ~ 12 m. The calculated φ_{NL} is ~ 1.1 which is close to the experimental result.

From the equation in Chapter 2, the SRS threshold is:

$$\frac{g_r P_0^{CR} L_{eff}}{A_{eff}} \approx 16 \quad (4.5)$$

Where g_r is 10^{-13} m/W and the calculated SRS threshold (P_0^{CR}) for this laser is ~ 1.7 kW. The peak power of the 80-ns laser pulse is 17.3 kW at 160 W average output power. It is much higher than the SRS threshold power, and the SRS component can be found in the spectrum ~ 1115 nm.

The ASE and 1st-Raman spectra are the two components that cause spectral broadening at 1030 nm and 1115 nm, respectively. They result in a decrease in the laser intensity around the central wavelength. SRS also results in lower light conversion efficiency and more heat to dissipate for the laser system. Since a few components in the laser cavity only meet the operation requirements at the central wavelength of the laser (e.g., isolators), the ASE and SRS will cause potential issues with these components due to their spectral mismatches.

The optical spectra for the laser with different pulse duration are shown in Fig. 4-18(b). The SRS for the 10 ns and 34 ns is slightly higher than that of the 56 ns and 80 ns. For ASE part, there is no significant difference for all of them. The S/N for the laser at central wavelength to SRS is ~ 20 dB and it is ~ 25 dB for the ASE.

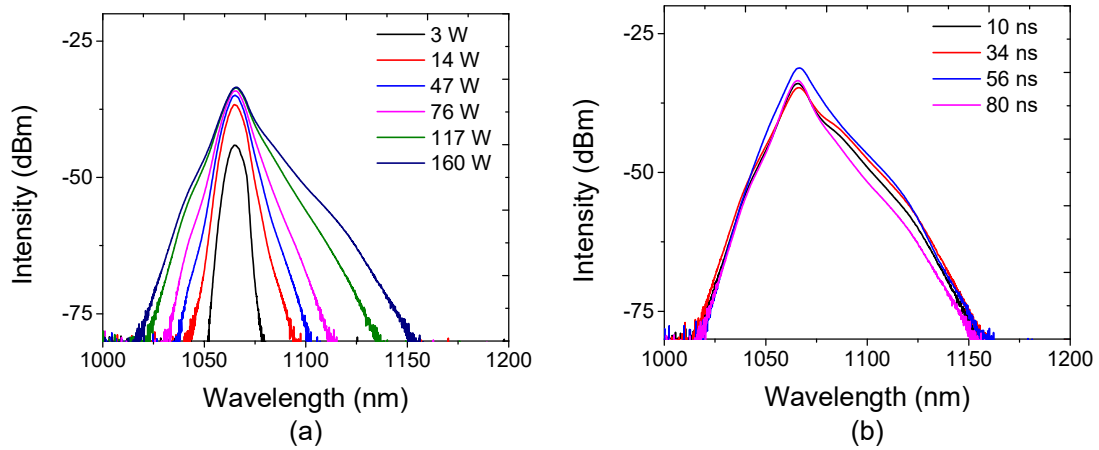


Fig. 4-18. (a) The optical spectra of the 80-ns final output laser pulses at different output power. (b) The optical spectra of the final output laser pulses at different pulse duration and ~160 W average output power.

Fig. 4-19 shows the pulse shapes and optical spectra of the backward propagation light monitored at Tap3. For the backward light, it contains ASE, SRS and the reflected light of the forward signal from the fusion points of the YDF of the main amplifier. The left and right peaks correspond to the reflected light from the F1 and F2 in Fig. 4-12 respectively. Because the reflected light has not been boosted in the main amplifier, the left peak is lower than the right one. The optical spectra of the reflected light are shown in Fig. 4-19(b), which are similar for the laser pulses with four pulse duration.

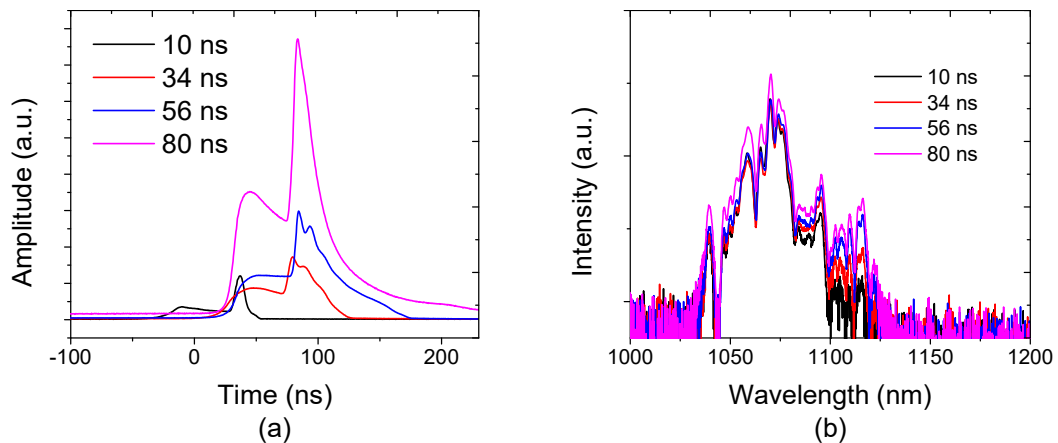


Fig. 4-19. The pulse shapes (a) and the optical spectra (b) monitored at the Tap3 of the YDPFL.

As discussed in Section 4.2.3, the slow leading edge which corresponding to a relatively narrow frequency spectral width through the Fourier transform of the leading-edge leads to severely decrease of the SBS threshold. However, the seed laser from an SLED with wide optical spectrum avoids the SBS effect in the experiments. For this YDPFL, no SBS was found in either the pre-amplifier or the main amplifier stage. The 4σ beam quality (M^2) of this laser is ~ 1.7 in both X and Y axis as shown in Fig. 4-20, and it is measured with 15 W output power and 80 ns pulse duration.

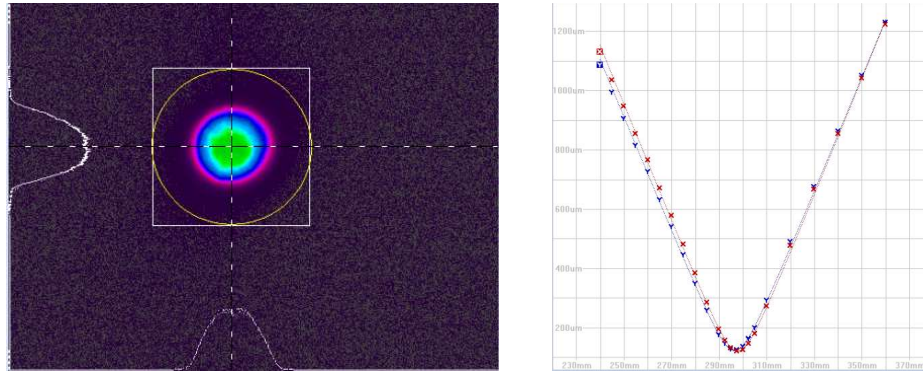


Fig. 4-20. M^2 test result of the YDPFL.

Fig. 4-21 illustrates the $\sim 67\%$ optical-to-optical conversion efficiency and it is obtained by calculating the ratio of the average output power of the YDPFL to the average pump power for the main amplifier. As a rule of thumb, the maximal extractable pulse energy from the laser cavity is ~ 10 times of the saturation energy (limited by ASE and spurious lasing) [147] and the maximal extractable pulse energy can be estimated by:

$$E_{ext} \approx 10 \frac{h\nu_s A}{(\sigma_{es} + \sigma_{as}) \Gamma_s} \approx 4 \text{ mJ} \quad (4.6)$$

Where $h\nu_s$ and A are the signal photon energy and the core area of the fiber. σ_{es} and σ_{as} represents the emission and absorption cross-section at the signal wavelength respectively. Γ_s is the filling factor of active dopant. Since the output pulse energy in the experiment is

1.45 mJ for the 80 ns laser pulses, the linearity of the efficiency indicates that the system still has the potential for power scaling. The pulse duration can be further increased or decreased by tuning the drive current board. The pulse repetition rate of the laser can be adjusted from one shot to 1 MHz. Similar to the pulse duration, it can be further increased.

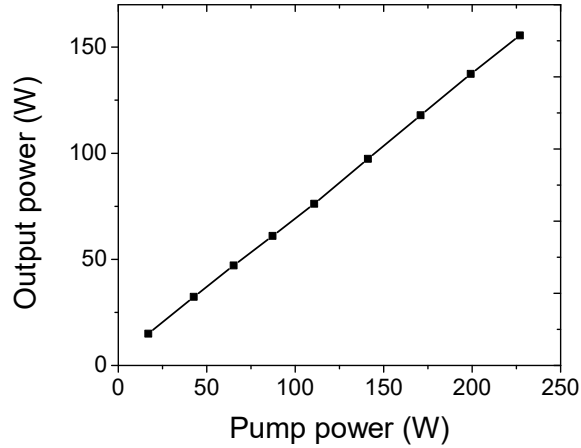


Fig. 4-21. The Optical-to-optical conversion efficiency for the main amplifier of the YDPFL.

Fig. 4-22 shows the waveforms of the seed laser with 80 ns pulse duration, the current applied to the pump diodes of the pre-amplifier and the main amplifier. According to the pulsed pump scheme proposed in Section 3.3, the threshold pulse repetition rate (f_i) of 110 kHz results in the pump duration of 9 μ s which is independent of the pulse repetition rate. The pump power (P_P) is kept at the maximum reachable level for the main amplifier stage. For the pre-amplifier stage, due to the maximum reachable pump power (10 W) is beyond the requirement for amplifying the seed pulse, consequently a fixed level below the maximum pump power is used for this stage. The seed pulse is injected at the end of the pump pulse to obtain the optimal performance. When the pulse repetition rate reaches (or is higher than) f_i , the time span between seed pulses is equal to (or longer than) the pump duration which leads to CW pump (Fig. 4-22 (e) and (f)). For the other pulse duration of this YDPFL, the same pulsed pump is implemented and the only difference is the pump

duration which is determined by the corresponding f_i .

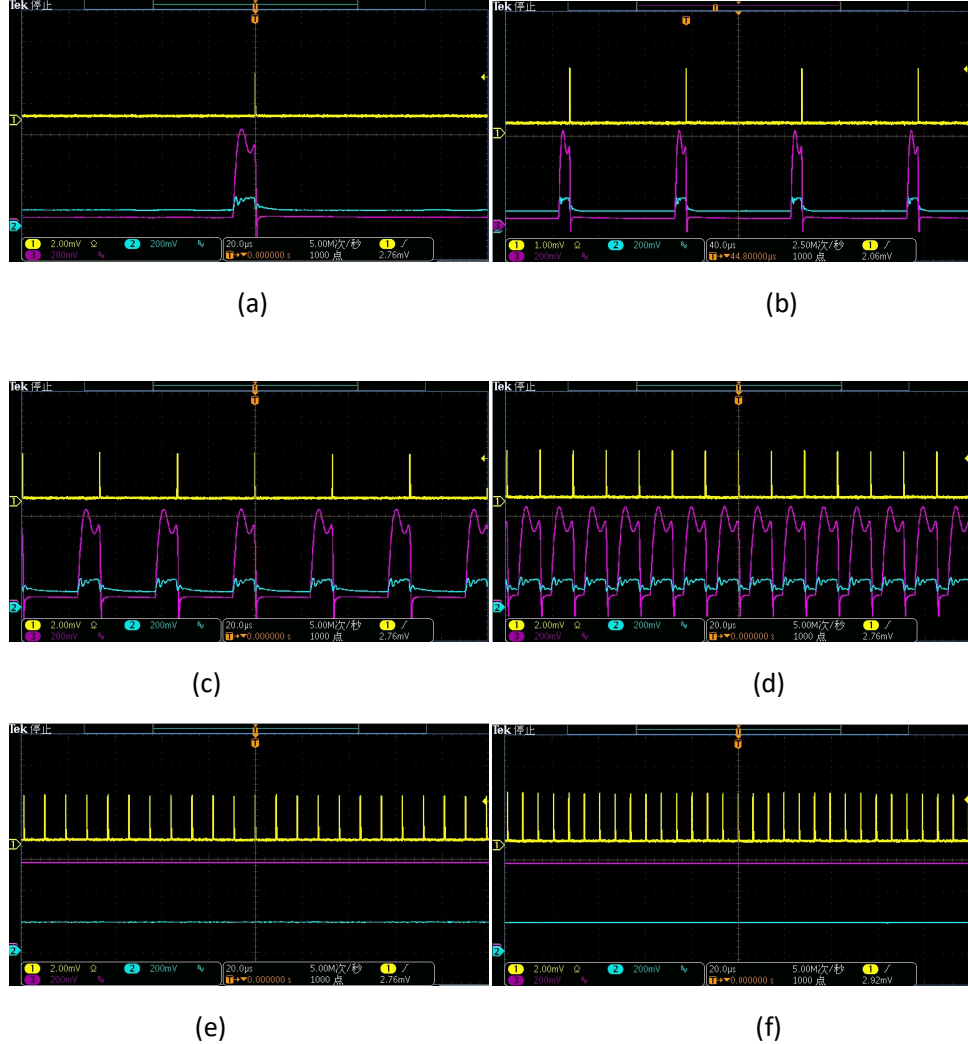


Fig. 4-22. The waveform of the 80-ns seed pulse (yellow), driving current for the pump LD of pre-amplifier (cyan) and main amplifier (purple) when the YDPFL is operating at 2 kHz (a), 10 kHz (b), 30 kHz (c), 70 kHz (d), 110 kHz (e) and 150 kHz (f) with f_i of 110 kHz.

The peak power of the final output laser with 80 ns seed pulse duration is shown in Fig. 4-23(a). For the laser at pulse repetition rate of 30 kHz, 70 kHz and 110 kHz, the peak power is fairly similar. Due to less stored energy in the main amplifier just before the seed laser injecting into the cavity with lower pulse repetition rate, the falling tail of 30 kHz pulse, and the pulses of 10 kHz and 2 kHz is less than that of the 110 kHz. When the laser

is operating at 150 kHz, the peak power is reduced as expected, the tail remains the same due to the distribution of the upper level ions along the gain fiber. Fig. 4-23(b) shows the optical spectra of the pulses at different pulse repetition rates. Obviously, the optical spectrum is broadened with higher peak power due to the SPM, ASE and SRS.

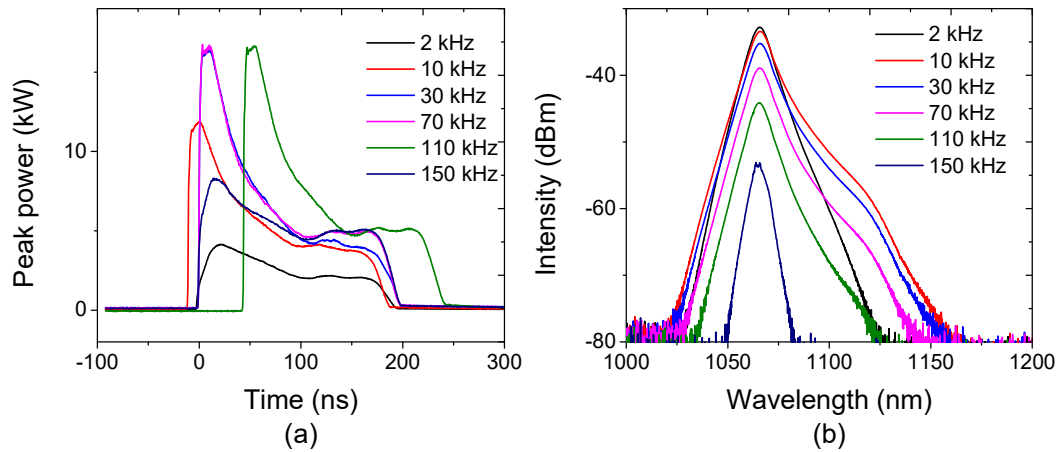


Fig. 4-23. Pulse shape (a) and optical spectra (b) of the 80-ns final output laser at several different pulse repetition rates.

The inter-pulse ASE of the YDPFL with 80 ns seed pulse at 2 kHz pulse repetition rate is measured with a fiber pigtailed AOM with two FC connectors at the fiber ends as shown in Fig. 4-24 (Left). The collimated output laser from the YDPFL with the average power of 0.7 W irradiates at the FC connector of the AOM and the ASE and laser signal is distinguished by the 10 μ s opening window of the AOM. The result shows that the ASE accounts a proportion of 14% for the total average output power and the optical spectra are shown in Fig. 4-24 (Right). It suggests, owing to the pulsed pump scheme utilized for the YDPFL, low inter-pulse ASE power is reached and the laser has the peak power of 4.1 kW at a low pulse repetition rate of 2 kHz.

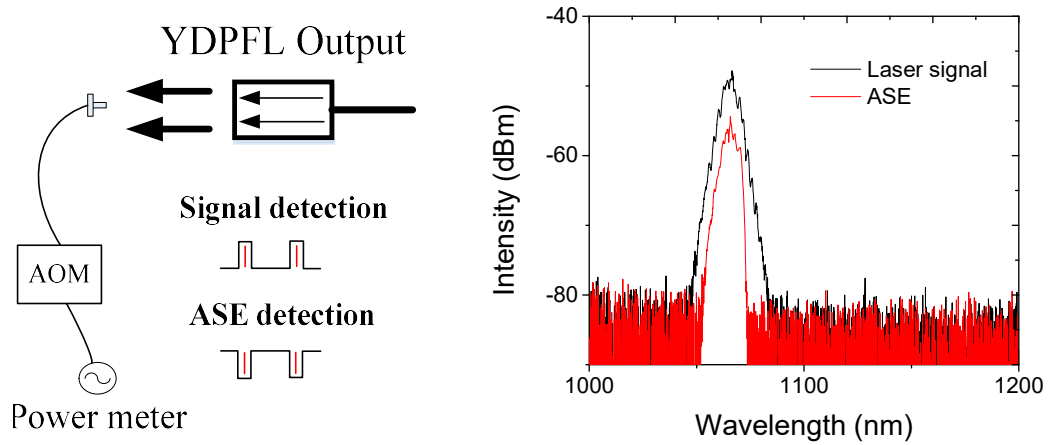


Fig. 4-24. (Left) The output laser of the YDPFL irradiates at the FC connector of the AOM with 10 μ s open window for distinguishing the ASE and signal. **(Right)** The optical spectra of the laser signal and ASE.

4.3.3 Conclusion

A highly versatile, high power YDPFL with an average output power of 160 W has been demonstrated, and the MOPA configuration YDPFL consists of two cascaded amplifiers with 30 μ m LMA fiber for the main amplifier stage

In order to mitigate the SRS component and enhance the pulse energy, owing to the directly modulated seed pulse and built-in pulse shaping feature, a triangular seed pulse shape with several pulse durations (80 ns, 56 ns, 34 ns and 10 ns) is investigated with the YDPFL. The laser with pulse energy of 1.45 mJ has been reached with 80 ns seed pulse, and the power in the 1st Raman peak at \sim 1115 nm is at -20 dB compared to the center wavelength of the signal laser.

To address the SBS which is a killing factor for high power YDPFL, especially when the laser is implemented with a triangular seed pulse shape which leads to significantly deteriorate the SBS threshold power, instead of using the DFB and FP LDs, an SLED seed source with 3 dB optical spectrum of 20 nm, has been chosen to produce the seed pulses. No SBS spike has been captured in the laser pre-amplifier and main amplifier

cavities.

The inter-pulse ASE, which is a potential risk when the YDPFL operating at lower pulse repetition rate, has been suppressed through the pulsed pump method for YDPFL with adjustable pulse duration and pulse repetition rate proposed in Section 3.3. The threshold pulse repetition rate (f_i) is determined according to the criteria discussed in that section and it is only related to the seed pulse duration. The pump duration for each seed pulse is fixed and calculated from the f_i and the pump power at the main amplifier stage is kept at the maximum reachable level. When the YDPFL is operating with a low pulse repetition rate of 2 kHz, thanks to this design, the inter-pulses ASE is 14% of the total output power and the laser peak power of 4.1 kW has been reached.

The performance of the YDPFL is characterized with the UPER parameter. For the YDPFL with the four pulse durations, UPERs for the laser with 34 ns seed pulse duration are largest with higher than 8 kW ablation threshold power. For the ablation threshold power less than 5 kW, the laser with 80 ns has the higher UPERs. It suggests there are less wasted energy and thus narrower HAZ when choosing these laser parameters with higher UPERs during laser-material interactions. However, due to the different pulse energy (1.45 mJ, 0.94 mJ, 0.45 mJ and 0.14 mJ for the laser with 80 ns, 56 ns, 34 ns and 10 ns pulse duration respectively) and energy wasted for processing the plasma, the laser processing efficiency is subject to further verification with the material.

The optical-to-optical conversion efficiency of $\sim 67\%$ for the main amplifier and the 4σ beam quality (M^2) of 1.7 is obtained. The power of this YDPFL can be further scaled up. The YDPFL with the novel design in this section is a favorable candidate for industrial applications requiring robustness and reliability characteristics.

4.4 HIGH PEAK POWER YTTERBIUM-DOPED PULSED FIBER LASER

For YDPFLs with short pulse duration in femtoseconds or short picoseconds range, the laser-material interaction is dominated by photon coupling induced microstructures during laser treatment [148]. When the laser pulse duration reaches a longer time scale such as nanoseconds, a large amount of heat is generated, and laser processing is considered to be thermal treatment [124]. Within the thermal and non-thermal processing range, several different mechanisms occur according to the laser pulse duration and the detailed response which is strongly dependent on the heat transfer coefficient and the optical properties of the material under laser treatment [62]. Fig. 4-25 shows the laser-material interaction during the laser processing with long and ultra-short pulse laser. For the ultra-short laser processing, there is less thermal effect and HAZ, no debris/micro cracking/damaged surface. For long pulse laser, the efficiency for deep engraving, cutting and drilling is higher than that of the ultra-short pulse laser.

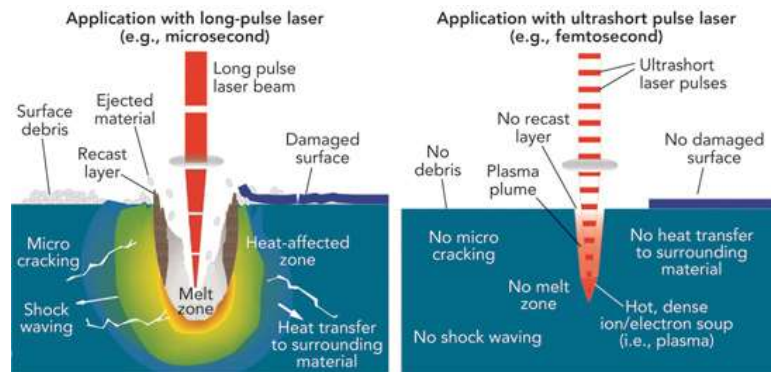


Fig. 4-25. The processing effects of an ultrashort (e.g., femtosecond) pulse laser compared to a long-pulse (e.g., microsecond) laser [149].

Lasers with different pulse duration have different mechanisms behind the laser-material interaction. For a few laser applications, particular laser pulse duration is

preferred to achieve the desired laser processing effect. In Chapter 5, we find that the pulse duration of the laser is one of the fatal factors for achieving the blackening effect of aluminum with alumina surface. In some cases, multiple laser treatments with different pulse duration are required for a same workpiece. All these makes the YDPFLs with adjustable pulse duration in a wide range an attractive and valuable laser source for industrial applications.

Driven by this, in this section, I demonstrate a monolithic high peak power YDPFL with adjustable pulse duration extending to sub-ns range.

4.4.1 Seed laser with adjustable pulse duration from ps to ns

The most widely used technique for generating ultra-short laser pulses, mode-locking, is inappropriate as the pulse width and pulse repetition rate are non-variable due to the fixed laser cavity and the harmonic oscillation nature [150].

Another avenue, gain-switching, is a potential candidate. The generation of lasers with ps pulse duration by this technique has been demonstrated by researchers since the last decade. In 2008, H. Liu et al. reported 90 ps pulses from a gain-switched laser diode at 1 MHz repetition rate with tunable center wavelength from 1053 nm to 1073 nm [151]. In 2013, P. S. Teh et al. reported 28 ps pulses produced by a gain-switched Fabry-Parot (FP) laser diode with maximum pulse energy of 3.23 μJ at 53 MHz pulse repetition rate and single-polarization output power of 200 W [152]. In 2014, Y. Yokoyama et al. proposed the design for generating 50 ps laser pulses from a gain-switched distributed feedback (DFB) laser diode at 1064 nm [153]. A monolithic semiconductor optical amplifier (SOA) was integrated into the DFB laser and generated 300 mW peak output power after amplification.

For laser pulses with pulse duration in ps or in the range of several ns, SBS does not occur because the signal pulse duration is less than the phonon lifetime (typically <10 ns) [64]. For long duration pulsed laser, as discussed in the previous sections, SBS is one of the capping factors for high power YDPFL. As demonstrated in Section 4.3, an SLED seed source with a broadband optical spectrum is a favorable candidate for solving this issue. For this high peak power YDPFL design, seed pulses are generated using SLEDs in the experiments, rather than the DFB or FP laser diodes utilized by many other researchers in the past.

4.4.2 Experimental setup

The configuration of the YDPFL for the experiments is demonstrated in Fig. 4-26 and a directly modulated SLED (LC96A1060CWG-20R from II-VI Inc.) is used to generate seed pulse with adjustable pulse duration and pulse repetition rate. The ASE light from the SLED is used as the seed for the YDPFL.

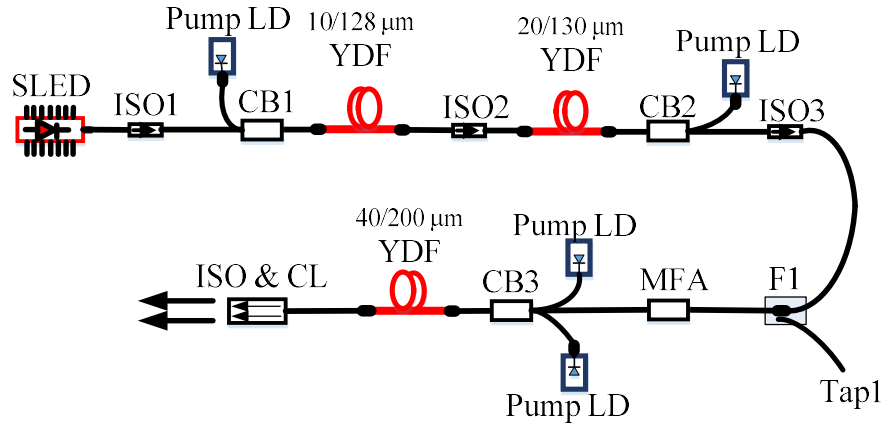


Fig. 4-26. Structure of the YDPFL in the experiments (ISO: isolator, CB: optical combiner, MFA: mode field adaptor, CL: collimator, F1: splicing fusion point 1).

The 1st-amplifier stage consists of a $(1+1) \times 1$ combiner (CB1) and a 7-meter-long Nufern YDF. The core/inner cladding diameter and numerical aperture (NA) of the gain

fiber are 10/130 μm and 0.075/0.46, respectively. The inner cladding absorption is 1.3 dB/m at 915 nm. A 915-nm multimode LD with maximal 11 W output power is coupled into the amplifier with the forward pumping scheme.

A 5.5-meter-long Nufern YDF with 20/130 μm core/inner cladding diameter and 0.08/0.46 NA is used for the 2nd-amplifier stage. The inner cladding absorption is 2.9 dB/m at 915 nm. A (1+1) \times 1 combiner (CB2) couples maximal 11 W pump power from one 915 nm multimode LD with backward pump scheme.

For the 3rd-amplifier stage, the core/inner cladding diameter of the 1.2-meter-long nLight YDF is 40/200 μm and the absorption of the inner cladding is 9.3 dB/m at 920 nm. One (2+1) \times 1 combiner (CB3) is used to couple the maximal 39 W pump power from two multimode LDs at 976 nm into the amplifier with forward pumping scheme.

Comparing to the configurations of the YDPFLs in previous sections, one more amplifier stage is implemented here and the fiber with relatively larger mode field diameter is used for the 3rd-amplifier stage to reduce the SRS which is a limiting factor for the peak power of the laser pulses. To reduce the forward ASE especially for the 350 ps laser pulses, the forward pump scheme is used for the 1st-amplifier stage. For 2nd-amplifier stage, the backward pump scheme is used to enhance the amplifier's efficiency. For the 3rd-amplifier stage, to reduce the SRS effect due to the high peak power of the output laser, the forward pump scheme is used to reduce the effective fiber length.

Three fiber pigtailed isolators (ISO1, ISO2 and ISO3) are equipped to block the counter-propagating light after the SLED, 1st-amplifier and 2nd-amplifier stages. The band-pass coating with 14 nm (FWHM) bandwidth centered at 1060 nm is coated on the optical lens surface within the ISO2 to filter out part of the ASE and the stimulated

Raman scattering (SRS) components. The MFA after the ISO3 is to efficiently transfer light between the two fibers with different modal fields.

A multimode fiber is attached closely to the fusion point (F1) between the ISO3 and MFA to monitor the backward SBS spike from Tap1.

As for surface damage, in general, the facet is more fragile. Dirt and facet irregularities dramatically reduce the damage threshold. To prevent the damage of the fiber facet, a collimator with isolator embedded is spliced to the output pigtail of the 3rd-amplifier and the output beam size is expanded to ~ 6 mm. To mitigate the SRS, the pigtail length of the collimator is kept as short as 0.5 m.

The efficiencies in the following paragraphs are obtained by calculating the ratio of the average output laser power of the YDPFL to the pump power. The optical spectra and the pulse shapes are measured by the optical spectrum analyzer (OSA) (YOKOGAWA AQ6370C) and the oscilloscope (OSC) (Tektronix 20GHz DSA72004C) with maximum 100GS/s real time sampling rate via a Newport 12GHz IR Photo detector (PD) (1544-B) respectively.

In the experiments, the 1st-amplifier and 2nd-amplifier stages are kept working at fixed pump power. The pump power for the 3rd-amplifier stage is adjustable. A home-made drive circuit board for the SLED is carefully tuned to ensure that the SLED operates in the gain-switching region and only the first spike of the relaxation oscillation is present for the 350 ps seed laser.

4.4.3 Seed and 1st-amplifier stage

The average output power for the SLED at pulse duration of 350 ps and 183 ns with different pulse repetition rate is listed in Table 4-2. Obviously, the linearity of the output

power is fairly promising. For the 350 ps pulse, the average output power at the SLED seed is $\sim 20 \mu\text{W}$ at 130 kHz pulse repetition rate and it is 1.35 mW for the ~ 183 ns pulses at 7 kHz pulse repetition rate. The pulse duration of the seed laser can be further reduced through tuning the driving circuit board, pulse duration of ~ 200 ps has been reached according to our preliminary experiments. From Fig. 4-27(a), the peak power of the 350 ps pulse is 0.41 W which is much lower than that of the 183-ns pulse (1.1 W). The SLED is operating in the ASE region when generating 350 ps or 183 ns pulse (Fig. 4-27(b)) and the central wavelength is shifted from ~ 1052 nm for the 350 ps pulse to ~ 1056 nm for the 183-ns pulse. The 3-dB bandwidth of optical spectrum is ~ 20 nm for the SLED seed source which is much wider than that of a DFB or FP laser.

Table 4-2. Average output power at several pulse durations with different pulse repetition rate.

Pulse duration	Pulse repetition rate	Average output power
350 ps	800 kHz	128 μW
350 ps	200 kHz	30.7 μW
183 ns	45 kHz	8.71 mW
183 ns	10 kHz	1.95 mW

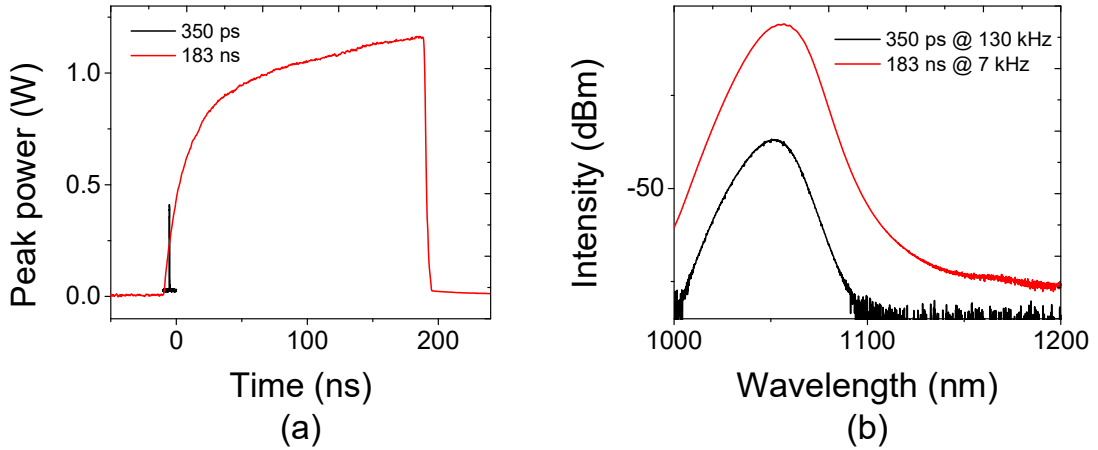


Fig. 4-27. The pulse shape (a) and optical spectrum (b) of the laser pulses with 350 ps and 183 ns pulse duration.

Fig. 4-28(a) shows the average output power after 1st-amplifier stage with different seeding conditions. It is manifest higher efficiency can be reached with higher pulse repetition rate for the pulse with same pulse duration. For the 183-ns pulse, due to the much higher peak power and longer pulse duration of the seed pulse, the efficiency is 14.6% and 12.7% for the 183-ns pulse with 45 kHz and 10 kHz pulse repetition rate respectively. For the 350 ps pulse, the efficiency is much lower as only 5.6% and 2.7% for the pulse at the 800 kHz and 200 kHz pulse repetition rate, respectively. Please note, the efficiency is 1% even when there is no seed signal. The pump power for the 1st-amplifier stage is set at 1.84 W as the output pulse is large enough for the 2nd-amplifier stage. As the 1st-amplifier stage is operating with low optical conversion efficiency, there should be large amount of inter-pulse ASE. However, due to the ASE nature of the seed pulse from SLED, it cannot be distinguished from the optical spectrum of the laser from the 1st-amplifier stage (Fig. 4-28(b)). To filter out the unwanted ASE component, as described in the Experiment setup section, a band pass filter is embedded in the ISO2 and the 3-dB optical spectrum is narrowed to ~ 7 nm. The central wavelength is shifted to ~ 1060 nm. The output pulse

energy after the 1st-amplifier stage is 0.16 μJ and 1.1 μJ for the 350 ps and 183 ns respectively.

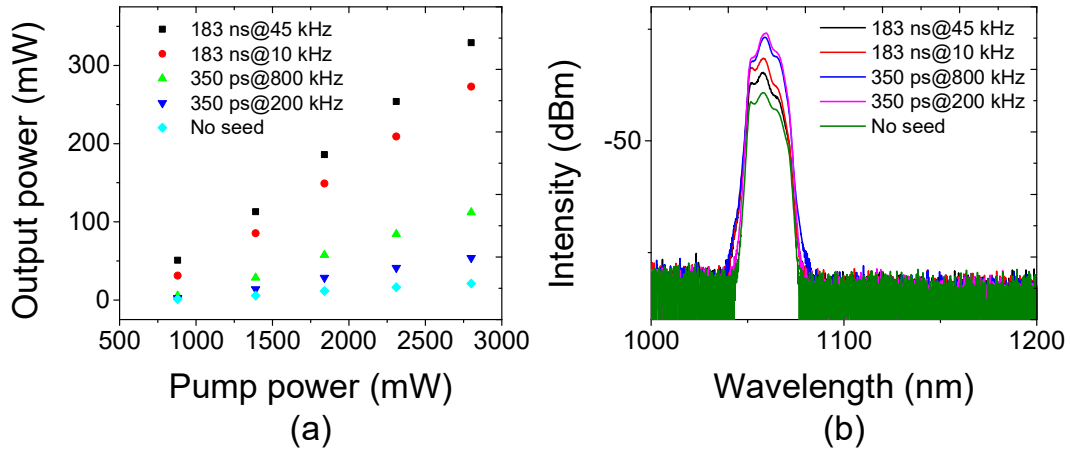


Fig. 4-28. The average output power (a) and the optical spectra (b) of the 1st-amplifier stage with different seeding conditions.

4.4.4 2nd-amplifier and 3rd-amplifier stages

The average output power of the 2nd-amplifier stage with 350 ps and 183 ns at different pulse repetition rate is depicted in Fig. 4-29(a). The optical conversion efficiency reaches 58% and 60% for the laser with 350 ps and 183 ns pulse duration respectively. From Fig. 4-29(b) and (c), there is obvious SRS and ASE component for the 350 ps pulse at 200 kHz pulse repetition rate with 5.68 W pump power. When the pump power reduces to 4.28 W, the output power is higher than 1 W for the 2nd-amplifier stage and there is no significant ASE and nonlinear effects. Thus for 2nd-amplifier stage, the pump power is fixed at 4.28 W.

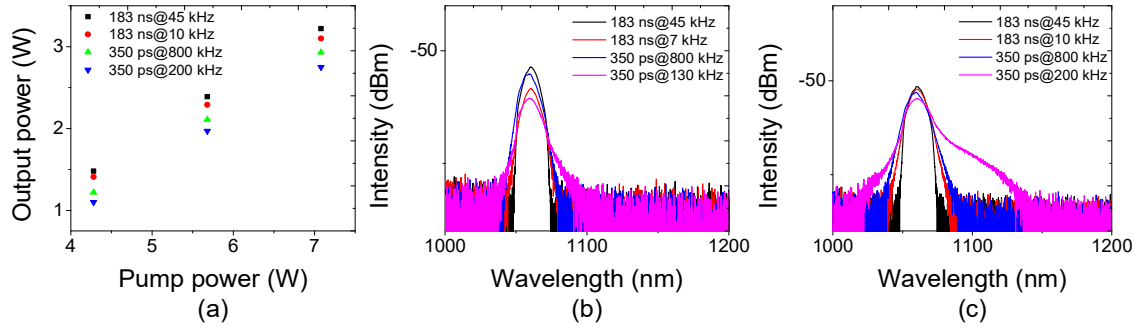


Fig. 4-29. (a) The average output power of the 2nd-amplifier stage with different pump power. (b) and (c) are the optical spectrum of the 2nd-amplifier stage when the pump power is at 4.28 W and 5.68 W respectively.

For the pulsed laser with 350 ps pulse duration at 130 kHz pulse repetition rate, the optical spectra of the final output laser are shown in Fig. 4-30(a). The spectrum of the final output is broadened compared to the spectrum of the 2nd-amplifier stage. The ASE and SRS components produced in the 3rd-amplifier stage are responsible for the widening at 1030 nm and 1110 nm respectively. The 3-dB bandwidth spectrum of the final output laser pulse is broadened from 13.4 nm at the 2nd-amplifier stage to 15.2 nm due to the Self-Phase Modulation (SPM) effect. The signal-to-noise ratio (SN) of the signal peak to SRS (1110 nm) and ASE (1030 nm) is 13 dB and 22 dB. The output pulse energy measured after the 2nd-amplifier stage and the final output is 8 μ J and 92 μ J, respectively.

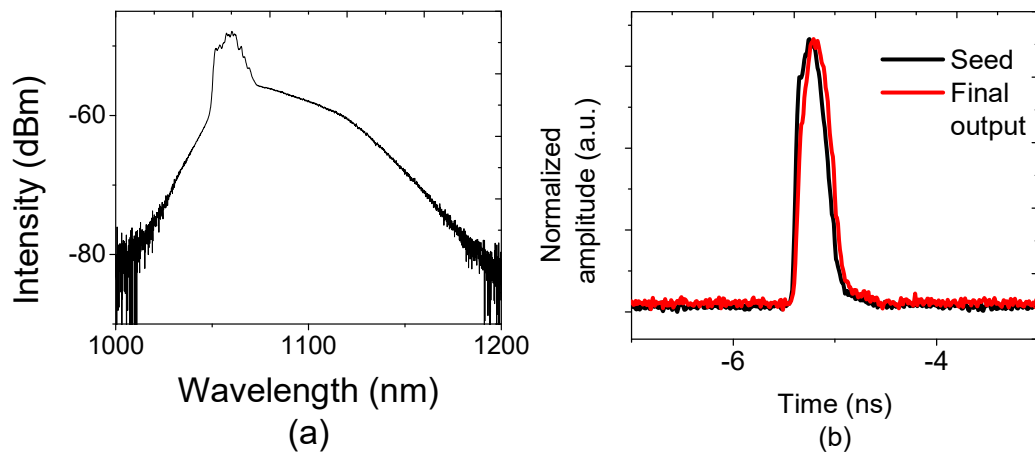


Fig. 4-30. For the 350 ps laser pulses, optical spectrum at the final output (a) and pulse shapes at the seed and the final output (b).

The normalized pulse shapes of the seed source and at the final output are shown in Fig. 4-30(b) with FWHM pulse duration of 350 ps. From the statistical function of the real-time oscilloscope, the pulse duration varies from 263 ps to 442 ps with the mean value of 350 ps for the seed and amplified pulses when using more than one thousand counts. The $\sim \pm 90$ ps jitter of the pulse duration can be classified into three categories.

First, the jitter from the driving current of the circuit board plays a crucial role for the final optical pulse duration jitter. The electric drive pulse is generated from a cost effective homemade circuit board. The seed pulse with longer pulse duration is from a complex programmable logic device (CPLD) chip with adjustable pulse repetition rate and pulse duration. Then the narrow peak of the seed pulse is picked by a bus transceiver and then amplified by two parallel metal-oxide-semiconductor field-effect transistors (MOSFETs). The amplified current pulses are applied to the SLED without DC bias. The pulse width jitters contributed from all these ICs can be greatly improved by fine tuning the circuit design.

Second, part of the time jitter comes from the random and uncorrelated optical pulse jitters. The random photon number fluctuations at low photon levels is the root cause of this time jitter and the rapidity of the turn-on time makes the difference for the timing jitter between the popular utilized DFB and FP laser diodes [154]. Under the same condition, the ratio of the time jitter to the pulse width is 15% for a DFB laser and reduced to 3.6% for a FP lasers. The suppression of time jitter in FP lasers is related to a decrease in the coherence time of the ASE in the time domain by multiplexing of ASE components in the frequency domain [155]. The study on the pulse width jitter of a gain-switched SLED has not been reported to the best of our knowledge. However according to

the analysis above, the jitters for an SLED should be less than that of a DFB or FP laser as more ASE components in the output laser for an SLED. Introducing external seeding signal has been proposed to be an effective way to reduce the jitters [156].

Third, the oscilloscope used in the experiment has an inherent time jitter of 10 ps, which limited the resolution to 10 ps.

To investigate the ASE component of the final output laser, an AOM with a window of 600 ns is used to distinguish the laser pulses and the ASE component. The measurement results show that the laser proportion in the output laser is ~53% for the YDPFL operating at 130 kHz pulse repetition rate with 350 ps pulse duration (Fig. 4-31). Please note when no pump power is applied to the 3rd-amplifier stage, the signal proportion is ~72%. This indicates that part of the ASE is from 2nd-amplifier stage and further enhanced in the 3rd-amplifier. The ASE can be mitigated significantly by applying an AOM or band pass filter after the 2nd-amplifier stage. The YDPFL has a final average output power of ~12.5 W exclusive ASE part and the laser peak power of 275 kW for the 350 ps laser. The pulsed pump scheme discussed in Section 3.3 has also been implemented to this YDPFL, it serves the similar functions as discussed in the high average power YDPFL in Section 4.3 and will not be detailed here. The linear fit slope optical-to-optical efficiency is 28% for the 3rd-amplifier stage. The 4σ beam quality (M^2) is 2.7 and 2.8 for the X and Y directions respectively.

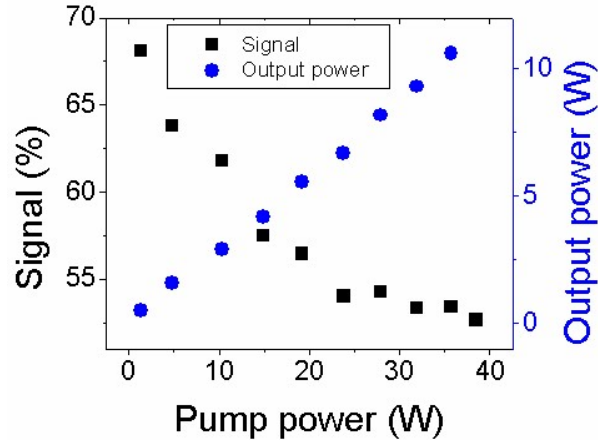


Fig. 4-31. Laser signal proportion and final output laser power with pump powers.

Fig. 4-32(a) shows the pulse shapes after the 2nd-amplifier stage and at the final output for the laser with 183 ns seed pulse. The leading edge of the seed pulse is intentionally smoothed as discussed in Section 4.1 to render more pulse energy on the top of the output laser pulse. From the pulse shape at the final output, it has been severely distorted due to the gain saturation effect and the 3-dB pulse duration is narrowed to ~ 10 ns (FWHM). The peak power and pulse energy of the final output laser are 137 kW and 3.2 mJ at 7 kHz pulse repetition rate, respectively. Fig. 4-32(b) shows the spectra after the 2nd-amplifier and at the final output. Similar to laser with 350 ps pulse duration, the spectrum is wider at the final output due to SPM, ASE and SRS.

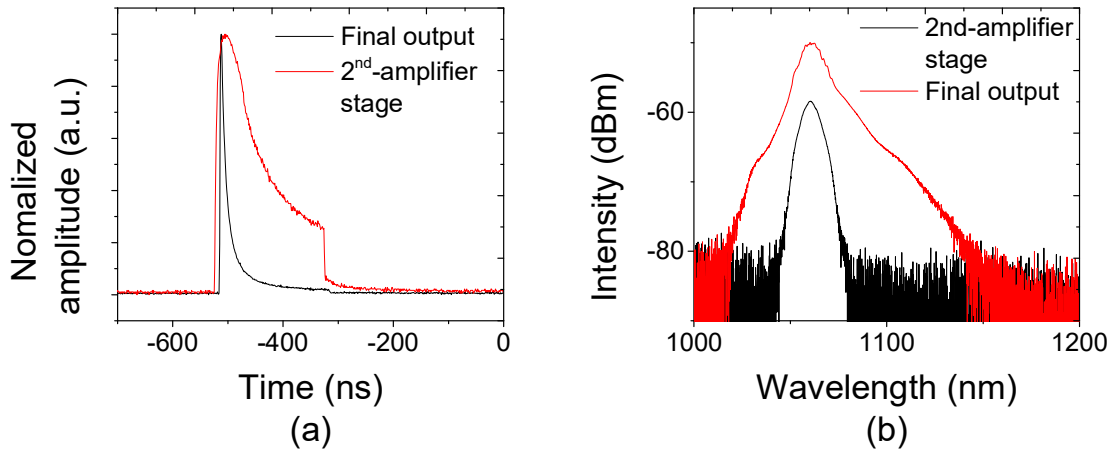


Fig. 4-32. Pulse shapes (a) and optical spectra (b) after the 2nd-amplifier and final output of the laser pulses with 183 ns pulse duration.

As a rule of thumb for high power fiber laser design, there are no unnecessary components in the laser cavity, especially for the high power amplifier stage. In this case, a multimode fiber is put closely to F1 to monitor the backward light in the 3rd-amplifier stage instead of an optical coupler. Fig. 4-33 shows the captured waveform on the oscilloscope via a photo detector. No SBS spike has been triggered and captured by the oscilloscope.

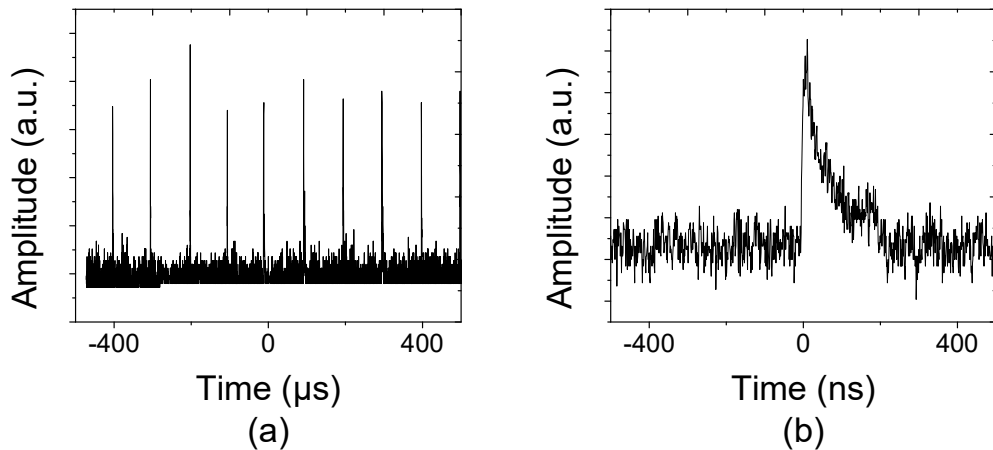


Fig. 4-33. Waveform of pulse trains (a) and one pulse (b) monitored from Tap1 to capture the SBS in 3rd-amplifier stage by oscilloscope via a photo detector.

4.4.5 Conclusion

YDPFLs with wide adjustable pulse duration are appealing and valuable laser sources for industrial applications due to the different mechanisms behind the laser-material interaction for different laser pulse duration. In this section, we demonstrate a novel high peak power YDPFL with adjustable pulse duration in the range of 350 ps to hundreds of ns seeded by an SLED.

The monolithic YDPFL is constructed with MOPA configuration and three cascade amplifiers are used to boost the seed signal from the SLED. For the 1st-amplifier and 2nd-amplifier, the core diameter of the gain fiber is 10 μm and 20 μm respectively, and fixed pump power from multimode pump LD at 915 nm is used for these two stages. A 1.2-m-length 40/200 μm gain fiber and tunable pump power from 39 W multimode pump LD at 976 nm is used for the 3rd-amplifier stage. The 976 nm laser diodes with TEC used here is to reduce the gain fiber length and to mitigate the SRS component in the 3rd-amplifier stage because the fiber has a higher absorption at that wavelength

For the laser with 350 ps pulse duration generated through gain-switching technique, peak power of 275 kW and pulse energy of 92 μJ is reached. The 90 ps jitter of the pulse duration is analyzed qualitatively. The ASE component of the final output laser is investigated via an AOM with 600 ns window, and the laser proportion is $\sim 53\%$. For the laser with 183 ns seed pulse duration, the leading edge of the seed pulse is smoothed, the peak power of 137 kW and pulse energy of 3.2 mJ is obtained. The 4σ M^2 is 2.7 and 2.8 for the X and Y directions, respectively.

Due to the ~ 20 nm optical spectrum of the SLED, SBS which is a capping factor for high peak power YDPFL is avoided. Similar as the high average power YDPFL discussed

in Section 4.3 the pulsed pump technique proposed in Section 3.3 is implemented to the YDPFL here to suppress the inter-pulse ASE at pulse repetition rate less than f_i .

The pulse repetition rate can be tuned from one shot to 2 MHz and it can be further increased. For the pulse duration, it also can further reduce to ~ 200 ps range by tuning the driving circuit board. This novel high peak power YDPFL is ideal for many industrial applications.

4.5 SUMMARY

I dedicated this chapter for the high power YDPFL with MOPA configuration seeded by directly modulated diode.

Firstly, from the perspective of laser material interaction during laser processing, the energy of the laser pulse whose peak power is higher than the ablation threshold power of the material contributes to the final desired treatment outcomes. The rest of the laser pulse energy is wasted and forms the HAZ. For a high power YDPFL with directly modulated seed source, the different laser pulse shapes result in different laser processing efficiencies.

To better characterize the laser pulse of high power YDPFLs by considering the laser-material interaction, a new parameter, Usable Pulse Energy Ratio (UPER) is proposed. The UPER is defined as the ratio of the pulse energy of the part of the nanosecond laser pulse whose peak power is higher than the predefined ablation threshold power to the maximum reachable pulse energy. We comprehend qualitatively whether the workpiece can be laser processed or not, how much pulse energy is wasted, and how wide the HAZ is after laser treatment through this parameter.

A high power YDPFL with three seed pulse shapes, rectangles, triangles and RWTT

shapes have been experimentally investigated. When the ablation threshold power is higher than 3 kW, the UPER of the laser with triangular and RWTT is lower than that of the rectangular shape. However, the UPER grows to 70.3% for a laser having a triangular seed pulse shape and it is about 5% higher than that of the rectangular seed pulse shape at a lower ablation threshold power of 2 kW.

In addition to the undoubted merits of pulse shaping such as higher UPER at low ablation threshold power and less SRS components, when the leading edge of the seed pulse rises slowly and smoothly, such as a triangular shape, it renders another dilemma, SBS. The smooth rising edge of the triangle possesses a narrow frequency spectrum, and results in a significant deterioration of the SBS threshold. Lots of SBS spikes are captured for the laser with triangular seed pulse shape. However, for the seed laser with RWTT shape, no SBS has been found in the experiment

Secondly, a novel high power YDPFL with an average output power of 160 W has been demonstrated, and the MOPA configuration YDPFL consists of two cascaded amplifiers with 30 μm LMA fiber for the main amplifier stage.

The potential risks, SRS, SBS and ASE, for a high power YDPFL have been cautiously addressed. In order to mitigate the SRS component and enhance the pulse energy, a triangular seed pulse shape is adopted for the laser. The laser with pulse energy of 1.45 mJ has been reached with 80 ns seed pulse, and the power in the 1st Raman peak is at -20 dB compared to the center wavelength of the signal laser.

To address the SBS which is a killing factor for high power YDPFL, especially when the laser is implemented with a triangular seed pulse shape which leads to significantly deteriorate the SBS threshold power, an SLED seed source with 3 dB optical spectrum of

20 nm, has been chosen to produce the seed pulses.

The inter-pulse ASE, which is a risk when the YDPFL working at lower pulse repetition rate, has been suppressed through the novel pulsed pump method for YDPFL with adjustable pulse duration and pulse repetition rate proposed in Section 3.3. When the YDPFL is operating with a low pulse repetition rate of 2 kHz, thanks to this design, the inter-pulses ASE is only 14% of the total output power and the laser peak power of 4.1 kW has been reached.

The performance of the YDPFL is characterized with the UPER parameter. For the YDPFL with the four pulse durations (80 ns, 56 ns, 34 ns and 10 ns), UPERs for the laser with 34 ns seed pulse duration are largest with higher than 8 kW ablation threshold power. For the ablation threshold power less than 5 kW, the laser with 80 ns has the higher UPERs. It suggests there are less wasted energy and thus narrower HAZ when choosing the laser parameters with these higher UPERs during laser-material interactions. However, due to the different pulse energy (1.45 mJ, 0.94 mJ, 0.45 mJ and 0.14 mJ for the laser with 80 ns, 56 ns, 34 ns and 10 ns pulse duration respectively) and energy wasted for processing the plasma, the laser processing efficiency is subject to further verification with the material.

The optical-to-optical conversion efficiency of $\sim 67\%$ for the main amplifier and the 4σ beam quality (M^2) of 1.7 is obtained. The YDPFL with the novel design in this section is a superior candidate for industrial applications requiring robustness and reliability characteristics.

Finally, I demonstrate a novel high peak power YDPFL with adjustable pulse duration in the range of 350 ps to hundreds of ns seeded by an SLED. The monolithic YDPFL is

constructed with MOPA configuration which consists of three cascade amplifiers. A 1.2-m-length 40/200 μm LMA gain fiber and tunable pump power from 39 W multimode pump LD at 976 nm is used for the 3rd-amplifier stage.

For the laser with 350 ps pulse duration generated through gain-switching technique, peak power of 275 kW and pulse energy of 92 μJ is reached. The 90 ps jitter of the pulse duration is analyzed qualitatively. The ASE component of the final output laser is investigated via an AOM with 600 ns window, and the laser proportion is $\sim 53\%$. For the laser with 183 ns seed pulse duration, the leading edge of the seed pulse is smoothed, the peak power of 137 kW and pulse energy of 3.2 mJ is obtained. The $4\sigma M^2$ is 2.7 and 2.8 for the X and Y directions, respectively.

Due to the ~ 20 nm optical spectrum of the SLED, SBS is avoided. Similar as the high average power YDPFL, the pulsed pump technique proposed in previous chapter is implemented to this laser to suppress the inter-pulse ASE at pulse repetition rate less than f_i . The pulse duration can be further reduced to ~ 200 ps range by tuning the driving circuit board. This novel high peak power YDPFL is ideal for many industrial applications.

Chapter 5 NANOSECOND PULSED FIBER LASER

BLACKENING OF ALUMINUM ALLOY WITH ALUMINA SURFACE

5.1 INTRODUCTION

As described in Section 2.3, lasers are designed for certain applications, and applications also provide feedback on laser design requirements. In this chapter, an application by a high power nanosecond YDFL is studied.

Laser-assisted blackening or coloring on metal surfaces possesses many merits over conventional techniques such as ink printing, electrolytic oxidation, and emulsions, including non-contact handling, scratch resistance, no accelerated fading, digital technology which makes it effortless to change or edit the marking patterns, and environmental friendly [157]. As a result of these merits, laser-assisted blackening or coloring of metal surfaces is becoming an active research topic and has attracted the interest of many researchers [158-160].

Aluminum (Al) with an alumina surface is widely used because Al is the richest metal in the crust and an alumina surface that improves corrosion resistance, electrical insulation, surface smoothness and hardness [161,162]. Notwithstanding the abundance of Al, few reports have been made on laser induced coloring or blackening on it [163,164]. The mechanism behind has also not been explained for the laser induced blackening of the Al with alumina surface to the best of our knowledge.

In the following experiments, a 1060 Al alloy plate (Al > 99.6%, 1060 Al alloy is an Al-based alloy in the wrought family and is covered by the ISO standard) with an alumina surface is blackened by a high power nanosecond YDPFL.

5.2 EXPERIMENTAL SETUP

A commercial laser system equipped with a MOPA high power nanosecond YDPFL with a wavelength of 1064 nm is utilized for the experiments (Fig. 5-1). The laser beam is guided to and focused at a point of $\sim 46 \mu\text{m}$ diameter spot by the Galvo head and F-theta lens subsequently. The laser parameters, unless otherwise specified, are kept at 2 ns pulse duration, 1 μm hatching, 1 m/s scanning speed, 11.76 μJ pulse energy, 500 kHz pulse repetition rate and the sample is mounted right in the focal position.

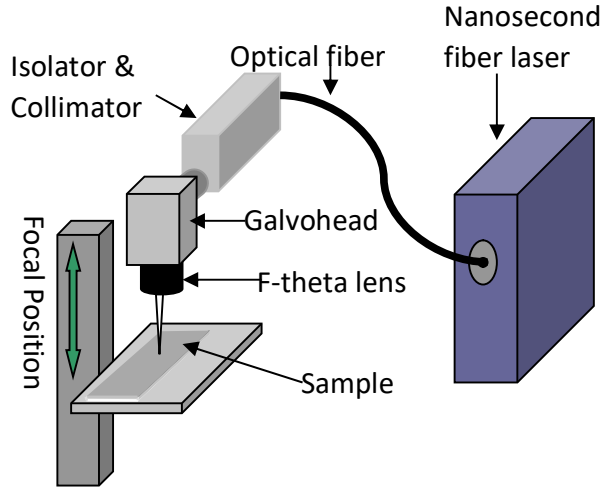


Fig. 5-1. Laser irradiation setup up with a high power nanosecond YDPFL (The pulse duration of the laser is tunable from 2 ns to 200 ns with an average output power of 20 W (Averaging over the entire time span between laser pulses and the pulse duration), the beam quality $M^2(4\sigma)$ equals to 1.3 and pulse repetition rate ranges from 1 kHz to 1 MHz).

A 1060 Al alloy plate with 0.2 mm thickness bought from the open market is used as the experimental sample. Prior to the laser irradiation, the sample is oxidized through anodizing electrolytic oxidation and the thickness of the alumina layer is $\sim 8 \mu\text{m}$.

5.3 MECHANISMS BEHIND THE BLACKENING

The matrix of 8 mm x 8 mm square blocks on the sample was irradiated with laser of

different parameters in air. Each block ($8\text{ mm} \times 8\text{ mm}$) is processed with a specified set of pulse energy and repetition rate, while maintaining the other parameters. The image in Fig. 5-2(a) shows the laser-treated sample. These square blocks are blackened at different level and can be distinguished by naked eyes. The middle part enclosed by red lines shows the color of shining black and we refer these square blocks as Black Square Blocks (BSBs). The square blocks on the right side of the BSBs show gray color, and they are referred as Gray Square Blocks (GSBs). For the square blocks on the left side of the BSBs, they are either partially blackened or not blackened at all due to the low laser power density.

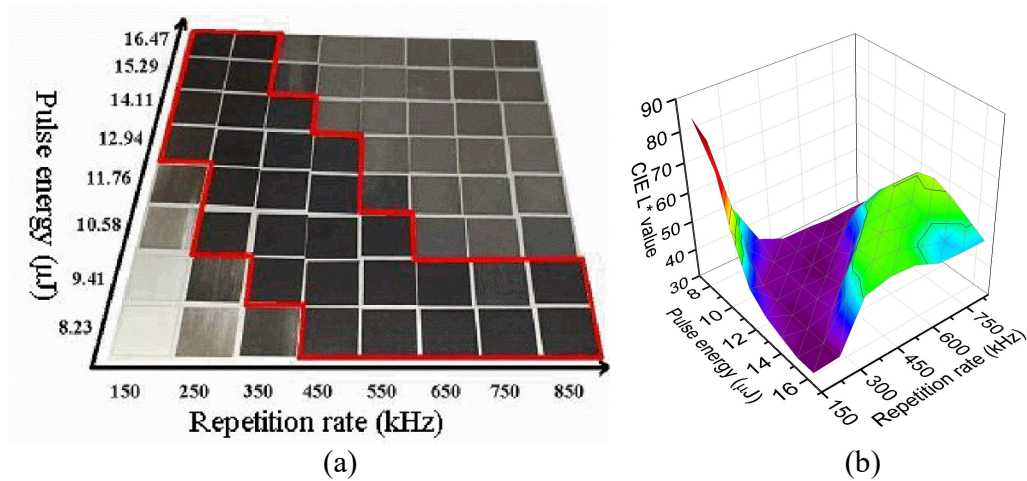


Fig. 5-2. (a) The image of the square blocks after the laser treatment. The different visual effects are obtained with different pulse energy ranging from $8.23\text{ }\mu\text{J}$ to $16.47\text{ }\mu\text{J}$, with $\sim 1.18\text{ }\mu\text{J}$ increment per step. The pulse repetition rate ranges from 150 kHz to 850 kHz . To have a clear view the photo is taken at a tilted angle. The BSBs are enclosed in red lines. The GSBs are the blocks on the right side to the BSBs. (b) the CIE L^* value for each square block in (a).

To describe the blackening effect of these square blocks quantitatively after laser irradiation, the standard CIE L^* value of them is measured by a spectrophotometer (CM-2600d from Konica Minolta) [165]. The CIE L^* value is relevant to the black and white color with the value from 0 to 100 representing the color from atrous black to pure white. From Fig. 5-2(b), it is obvious that the BSBs have the smallest CIE L^* value which ranges

from 34.4 to 39 among all the square blocks. The CIE L^* value of the GSBs ranges from 47 to 57.6. For the square blocks located at the left-down corner in Fig. 1(a), the CIE L^* value is large because the weak laser irradiation has only partially changed the optical properties of the sample after irradiation. When the laser pulse energy increases, the required pulse repetition rate to get a BSB reduces. With the same pulse repetition rate and different pulse energy, the square block could be changed to BSB or GSB after laser irradiation, and vice versa. This suggests that the laser treatment effect is the combination result of both the laser pulse energy and the number of pulses. To further study this, the CIE L^* value for all the square blocks is plotted corresponding to the laser power density in Fig. 5-3.

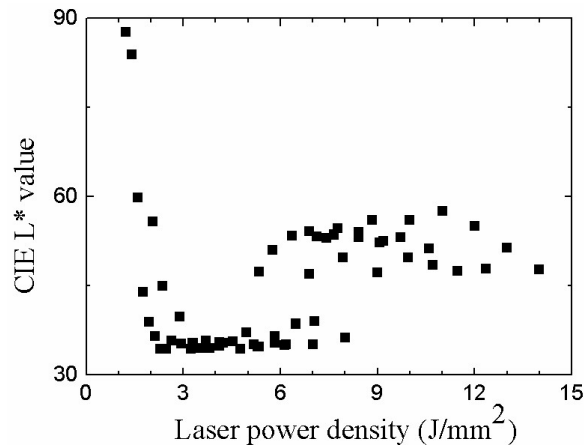


Fig. 5-3. The CIE L^* value of the sample square blocks vs. laser power density (Accumulated irradiation dose which is calculated by multiplying the laser power and the number of pulses per area).

From Fig. 5-3, it is comprehensible that to obtain a BSB the power density needs to be controlled within a range. However, for power density ranging from 5.35 J/ mm² to 8 J/ mm², both BSBs and GSBs can be formed. It suggests that, except the laser power density, the heating and cooling patterns associated with the laser pulse energy and repetition rate are also influential for the laser blackening. There are only GSBs fabricated when the

laser power density is higher than 8 J/mm^2 . The hatching and laser scanning speed are indeed crucial factors, because they are not only to affect the blackening effect as they are linking to the heating and cooling patterns just discussed, but also closely related to the processing efficiency especially when coming to high volume industrial usage.

To study the hatching influence of the laser treatment, several hatching values from $0.2 \text{ }\mu\text{m}$ to $9 \text{ }\mu\text{m}$ are selected (Please note the minimum reachable hatching value is $0.15 \text{ }\mu\text{m}$ limited by the laser system). In the experiments, the laser system is working with $9.41 \text{ }\mu\text{J}$ pulse energy, 500 kHz pulse repetition rate and 1000 mm/s scanning speed. From the results shown in Fig. 5-4(a), the CIE L^* value goes down along with smaller hatching value or higher laser power density. When the hatching value is equal or less than $1 \text{ }\mu\text{m}$, the shining blackening effect after laser processing can be achieved. For the hatching value above 5 , part of the area is not fully blackened and the CIE L^* value is more than 40 .

For the laser scanning speed experiments, the laser system parameters are the same as those in the hatching experiments except that the hatching value is fixed at $1 \text{ }\mu\text{m}$. The results in Fig. 5-4(b) show that the CIE L^* value bottoms at 34.1 when the scanning speed is at 600 mm/s and it is larger with faster scanning speed. For scanning speed between 1000 mm/s to 4000 mm/s , the blackening effect is consistent and BSBs still can be achieved. At a scanning speed of 5000 mm/s , only partial plate is blackened. However, the high power density causes part of the alumina to be removed with scanning speed of 200 mm/s .

Comparing the results of the hatching and scanning speed experiments, we can find that the CIE L^* value is 32.01 with the 23.53 J/mm^2 laser power density at $0.2 \text{ }\mu\text{m}$ hatching value. However, the CIE L^* value goes to 44.77 with the same 23.53 J/mm^2 laser power

density at 200 mm/s laser scanning speed. It reassures the laser power density as well as the heating and cooling patterns are crucial factors for resulting in BSB or GSB. Slow scanning speed (200 mm/s) with hatching value (1 μm) will create more thermal effect than that introduced by fast scanning speed (1000 mm/s) with hatching value (0.2 μm).

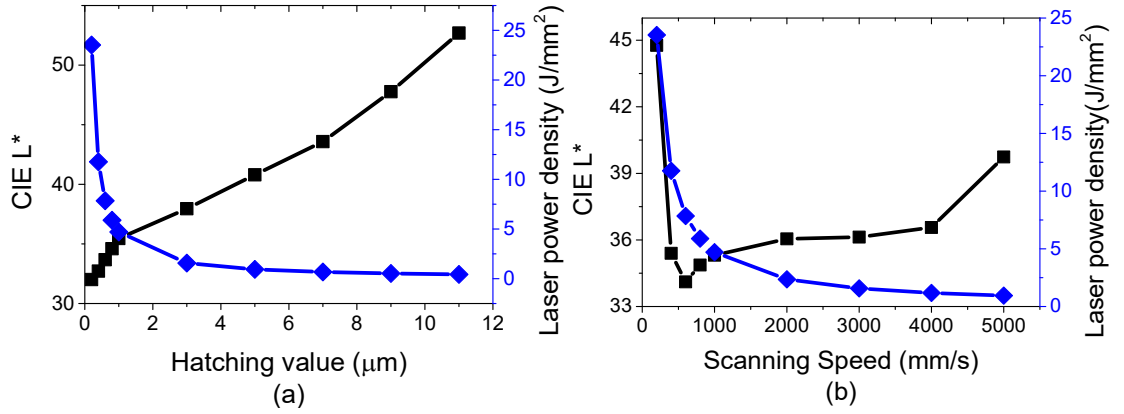


Fig. 5-4. The CIE L* value and laser power density corresponds to (a) the hatching and (b) scanning speed respectively. The laser system is working with 9.41 μJ pulse energy, 500 kHz pulse repetition rate.

From the above analysis, laser hatching value and scanning speed are significant factors affecting the laser power density and the thermal effect. For hatching value and scanning speed, they are controlled by the Galvohead. When the laser working with specific output power (or pulse energy) at fixed pulse repetition rate, the hatching value or scanning speed determines the overlap profile of the laser pulses during laser processing. This is directly related to the laser power density. It in turn links to the blackening effect and the formation of BSB or GSB. With suitable laser pulse energy, small hatching value and slow scanning speed will lead to smaller CIE L* value and BSBs will be produced. But if the hatching value and scanning speed is too small, the high laser power density and thermal effect will cause the alumina layer to be partially or fully removed. This leads to the destruction of the alumina and the formation of GSB as discussed in the subsequent paragraphs.

The surfaces profiles of the original samples without laser irradiation, the BSBs and the GSBs are measured by a Dektax XT Profilometer. The deep pits in the two curves are scribed by laser intentionally to make it easy for distinguishing the boarder of the surfaces with or without laser processing (Fig. 5-5). It shows that the surfaces of the BSBs and original material surfaces look relatively smooth with peak-to-peak roughness less than 3 μm (red curve in Fig. 5-5). There is no obvious height and roughness difference between them. The surface profiles of the GSBs are changed largely after the laser treatment and the surfaces are fully covered with various peaks and valleys. The peak-to-peak roughness is more than 7 μm and the height difference between the surfaces of the GSBs and original surface is around 8 μm . This indicates that most of the alumina layer is removed.

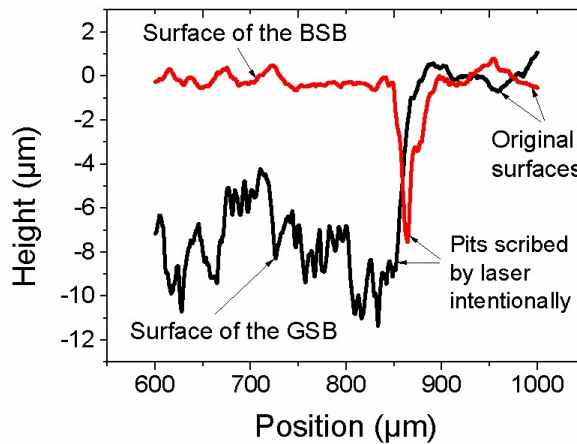


Fig. 5-5. The surfaces profiles of the BSB, the GSB and the original sample. The BSB and the GSB are the square blocks taken from Fig. 5-2 with 11.76 μJ pulse energy and 250 kHz and 850 kHz repetition rate respectively.

The surface of the GSB (Fig. 5-6(a)) is covered by the sponge-like NSs and MSs. These NSs/MSs are randomly allocated and the shapes and sizes are different from each other without fixed patterns. For the laser-induced GSBs in air, the mechanism behind is that they are formed by ablation of alumina and modification of the surface. From Fig. 5-6(b) there is no recognizable structural difference between the surfaces of the BSB (right part)

and the original sample (left part), while only color difference can be observed from this image. The continuity of the texture of the interface suggests that there is no NS or MS found at the alumina surface [10]. This also proves the findings in Fig. 5-5.

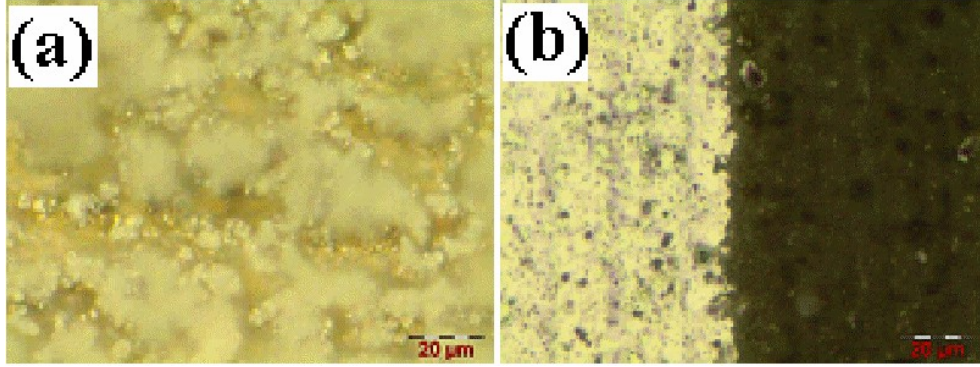


Fig. 5-6. The microscope images of the surfaces profiles of the BSB, the GSB and the original sample. The BSB and the GSB are the square blocks taken from Fig. 5-2 with 11.76 μ J pulse energy and 250 kHz and 850 kHz repetition rate respectively.

From the above analysis, the surface of the BSBs is the same as the original surface. To further identify the mechanism behind the black color of a BSB, the sample is firstly scribed on the back with a sharp blade without being cut through, and then it broke down by being bent back and forth. The cross-section is examined via a field emission scanning electron microscope (FE-SEM, EVO 18 from ZEISS). Lots of alumina blocks are peeled off from the Al alloy substrate by the bending force (Fig. 5-7). The boundary between the alumina layer and the bulk Al substrate is solid and smooth for the original plate without laser irradiation (Fig. 5-7(a) and Fig. 5-7(b)). However, there is a porous layer found at the bottom position of the alumina layer for the BSB (Fig. 5-7(c) and Fig. 5-7 (d)). The layer is filled with voids (Fig. 5-7(d)) whose diameter varies from several nanometers to several micrometers, which are much smaller than the laser beam size which is $\sim 46 \mu\text{m}$. These NSs/MSs are believed to be the reason for the black color. Fig. 5-8 shows the SEM image of the GSBs' surface.

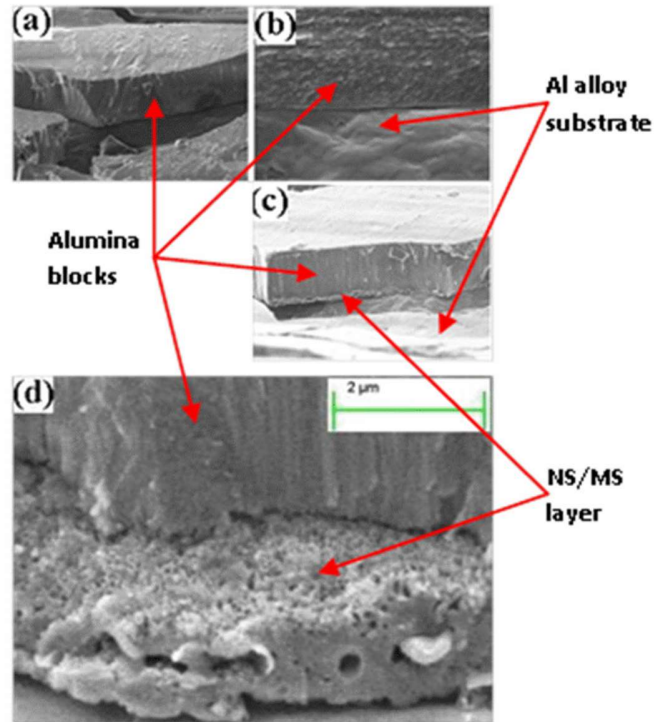


Fig. 5-7(a) and (b), the SEM images of the cross-sections of the original sample without laser irradiation ((a) amplified by 2 K X, (b) amplified by 20 K X). (c) and (d), the SEM images of the cross-sections of the BSBs ((c) amplified by 4 K X, (d) amplified by 15 K X).

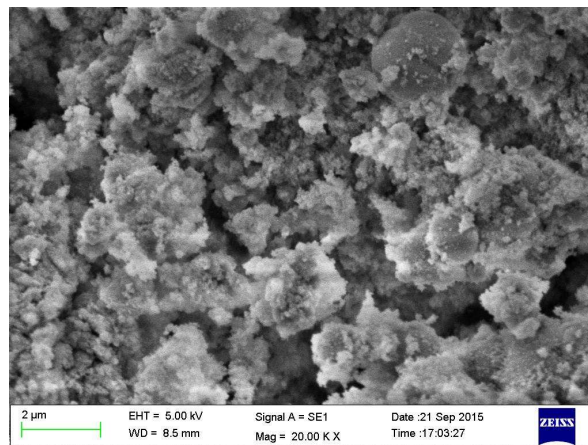


Fig. 5-8. The SEM images of the surface of GSBs.

The formation of the BSBs is different from that of the GSBs as the BSBs are formed

inside the sample and the later are formed in the open air. When the laser pulse with lower power density reaches at the alumina surface without ablation happening, it propagates through the alumina layer and reaches at the Al alloy substrate as alumina is transparent at near-infrared (NIR) wavelength [166]. The Al substrate absorbs the laser pulse energy and the thermal effect causes melting and evaporation of the aluminum at the interface area as the evaporation temperatures for aluminum and alumina are different (2327 °C and 2977 °C respectively). The plasma formed is confined by the surrounding medium and therefore results in higher temperature, larger pressure, and stronger shielding effect than that in open air [167,168]. These are supposed to be responsible for the thin NSs layer formed in the BSBs. During the laser ablation, vapor bubbles are created in the melted area and parts of them are coalesced together. Some bubbles cannot burst like in open air after laser pulse ceased because of the confinement of the medium, and this results in the formation of the micrometer size voids [169]. For those blocks on the left side of the BSBs in Fig. 5-2(a), the partially blackening color is the same reason as that of the BSBs.

The optical spectrum reflectance property is studied by a Perkin-Elmer spectrophotometer (Lambda 850) in ultraviolet (UV), visible light and infrared (IR) regimes for the original sample, the BSBs and the GSBs. The results in Fig. 5-9 show that the shapes of the reflectance curves of the BSBs and GSBs are similar and the reflectivity is much lower than that of the original sample. At the same time the BSB has the lowest reflectance. The fluctuations on the curves of the original sample and the BSB are due to the interference of the reflected light wave on the top and under boundaries of the alumina film [170]. Because most of the alumina layer is removed during the laser irradiation, there is little if any fluctuation on the curve for the GSB.

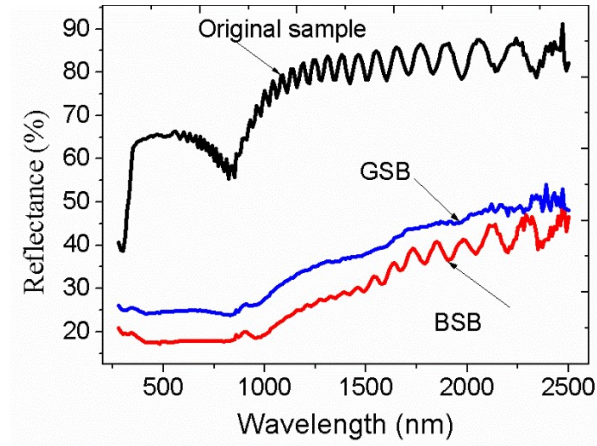


Fig. 5-9 The reflectance of the original sample without laser processing, the BSB and the GSB. The BSB and GSB are the square blocks chosen from Fig. 6-1(a) with 11.76 μJ pulse energy, 250 kHz and 850 kHz repetition rate respectively.

The plasmonic trapping of light by the NSs/MSs causes the much lower reflectance of the GSBs and the BSBs from deep UV to IR regime comparing with that of the original sample. However, the light trapping capability of the porous NSs/MSs in BSBs is stronger than that of the sponge-like NS/MS in GSBs. This is the reason behind the structural gray color of the GSBs and the much darker color of the BSBs. The reflectance of the BSB is less than 20% and the reflectance curve is fairly flat with less than 0.5% vibration in the spectrum range from 400 nm to 840 nm.

For a GSB, the alumina layer is partially or fully removed after the laser treatment. However, for a BSB the alumina layer is intact and the NSs/MSs is formed below the alumina layer. The following pictures indicate that a GSB is formed above the BSB formed prior to that (Fig. 5-10(a)). Therefore, there is obvious boundary between GSBs and BSBs.

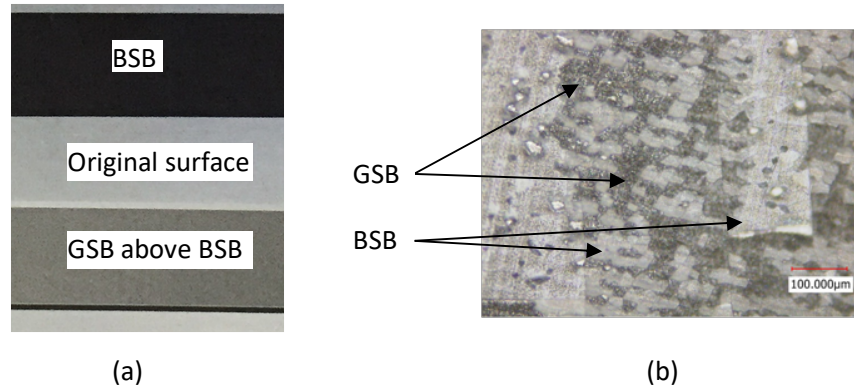


Fig. 5-10. (a) The BSB, original surface of the plate without laser treatment, and the GSB which is formed above a BSB. (b) The GSB and BSB are co-existent after laser treatment.

Compared with that for a BSB, more thermal effect is needed to carry out the ablation process to form a GSB. This can be achieved by larger pulse energy, higher power density and faster scanning speed etc. However, for a laser system, there is certain drift of the pulse energy among the laser pulses and the material under processing is not totally homogeneous. When considering all these factors, the GSBs and BSBs may co-exist when choosing the laser parameters around the ablation threshold level for GSB. This has been proven by the experimental result which is captured by the Keyence VK-X100 series microscope in Fig. 5-10(b), which suggests there is no obvious boundary for GSBs and BSBs under this circumstance. Several GSBs at the GSB-BSB border area in Fig. 5-2(a) also contain part of BSBs.

5.4 FEASIBILITY OF THE YTTERBIUM-DOPED PULSED FIBER LASER BLACKENING APPLICATION

The thickness of the alumina layer is measured with a coating thickness gauge (Minitest-600B) with a specified precision of $\pm 2 \mu\text{m}$. The results show that the thickness of the plate varies from $6.8 \mu\text{m}$ to $9.7 \mu\text{m}$. Fig. 5-11 is a surface profile curve of the plate

without laser treatment measured by a Dektax XT Profilometer. It shows the surface of the alumina is not flat and there is a peak-to-peak variation of $\sim 3 \mu\text{m}$.

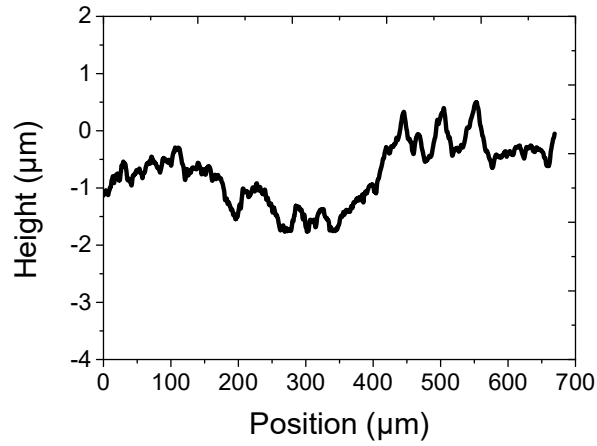


Fig. 5-11. The surface profile of the plate without laser treatment.

Two scenarios of the inconsistency and variation of the surface may relate to the blackening effect. Fig. 5-12(a) illustrates that the thickness nonuniformity is because the thickness of the alumina layer varies from $6 \mu\text{m}$ to $10 \mu\text{m}$. Fig. 5-12(b) shows that the thickness of the alumina layer is uniform and the inconsistency can be caused by the non-uniform surface of the aluminum substrate.

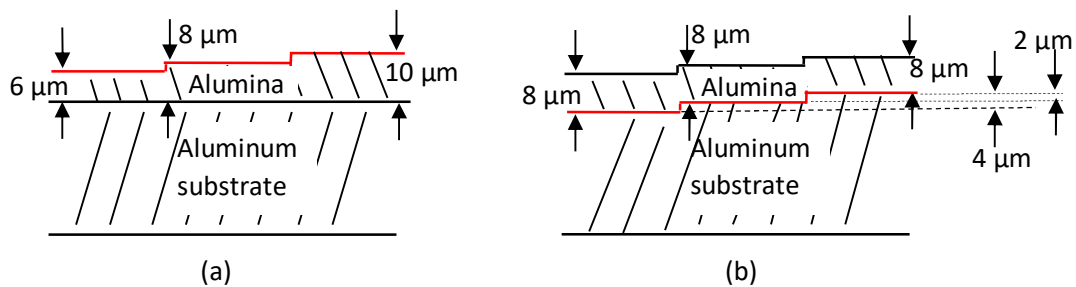


Fig. 5-12. The possible scenarios that may affect the blackening effect (the drawing is not in scale), (a) the thickness of the alumina layer is not consistent and it varies from $6 \mu\text{m}$ to $10 \mu\text{m}$. (b) the thickness of the alumina layer is consistent. However, the surface of the aluminum substrate is not smooth which causes the inconsistent alumina surface.

For the case of Fig. 5-12(a), as the transmission at the IR wavelength is around 60% \sim 80% for the alumina depending on the anodizing process [166], thicker alumina layer

leads to less laser pulse energy interaction with the aluminum substrate, and thus higher pulse energy or laser power density is needed to form the BSB. From the analysis and the discussion on the hatching and scanning speed experiments, a BSB can be generated with a relatively large range of laser parameters. As an example, BSBs can be produced with the laser pulse energy changing from 8.23 μJ to 16.47 μJ with other parameters fixed according to our experiments. For the inconsistency of 50% (4 μm variation to the 8 μm average), BSBs can be formed but the CIE L^* values may be a bit different. If the inconsistency for the alumina layer becomes much higher, definitely the blackening effect will be degraded.

For the case of Fig. 5-12(b), the thickness of the alumina layer is the same but the distance from the laser head to the surface of the aluminum is varied. To further study this, the impact of the focal position offset between the aluminum plate surface and the focal point position of the laser system is experimentally investigated. The results in Fig. 5-13 show that the BSBs can be fabricated and the CIE L^* value is kept relatively stable when the focal position offset is within ± 1 mm. Hence for the several-micrometer-long offset in Fig. 5-12(b), there should be negligible impact on the blackening effect. If the inconsistency goes higher than 1 mm, the inconsistency will be significant so that BSB cannot be produced or a GSB is formed instead. This off-set focal position issue can be mitigated to some extent by using the long focus distance lens.

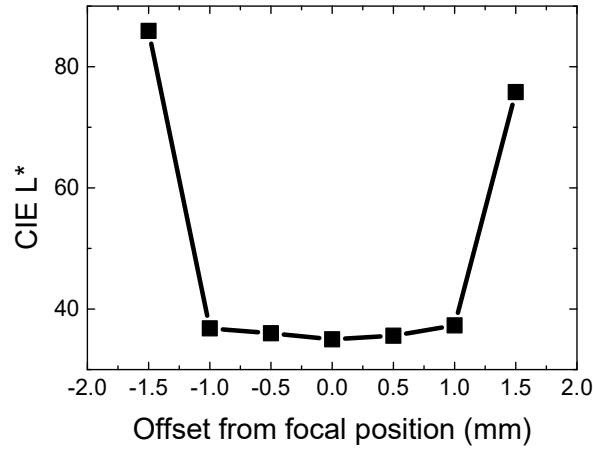


Fig. 5-13. CIE L* value with the offset between the plate surface and the focal position of the laser system.

To examine the environmental temperature influence, the sample is heated to and kept at around 33°C, 60°C and 100°C and then the laser irradiation with the same parameters is performed. Three BSBs are formed successfully with the CIE L* value is 35.0, 36.9 and 33.2 respectively.

In addition, five BSBs are generated on the sample at a time interval of one hour by laser irradiation with the same parameters. The results showed that the minimum and maximum CIE L* values were 34.5 and 34.7 which indicates positive consistence.

The laser irradiation experiments have also been performed with long pulse duration laser, whose pulse duration is 6 ns, 20 ns, 30 ns and 200 ns. The results show that BSBs can be formed when using 6 ns and 20 ns pulse duration with appropriate pulse energies. However, the degree of the tolerance of the pulse energy to obtain BSB decreases as pulse the duration increases. In our experiments, no BSB is successfully fabricated to have a pulse duration of 30 ns or 200 ns regardless of the laser parameters selected. The possible reason is that the thermal effect of the laser pulse is more severe as the duration of the laser pulse is prolonged. When larger pulse energy or power intensity is used, the outer

alumina layer has been destroyed. When the lower pulse energy or power intensity is reduced, the peak power of the laser pulse is insufficient to form the NSs/MSs.

5.5 POTENTIAL APPLICATIONS FOR THE BLACKENING SURFACE

Researchers have extensively studied the effects of surface textures on solar energy and light sensing applications [171-173]. Absorbers with NSs/MSs surfaces, such as nano/microporous cavities, nanotubes, nanosheets, nanoparticles and nanowires, have been shown to have enhanced thermoelectric performance or better energy conversion efficiency. The NSs/MSs formed on the aluminum substrate has promising heat conductivity. All of these features result in the BSB a potential candidate for absorbers for optical power sensing applications, especially in the visible range and in harsh operating environments.

Fig. 5-14 shows a surface absorber of a commercial power meter (from OPHIR Inc.) for long pulse laser or CW laser power measurement [174]. The optically absorbing refractory absorber is deposited on the heat conducting substrate which is made from copper or aluminum. When the laser beam irradiates the surface of the absorber, it will penetrate a thin layer with thickness of around $0.1\ \mu\text{m}$ to $1\ \mu\text{m}$ and will be absorbed by the absorber during the penetrating process. Heat generated in this process is flowing into the heat conducting substrate so that the temperature of the surface absorber will not be excessively high. The absorptivity of these absorbers ranges from ~ 0.8 to 0.97 [174].

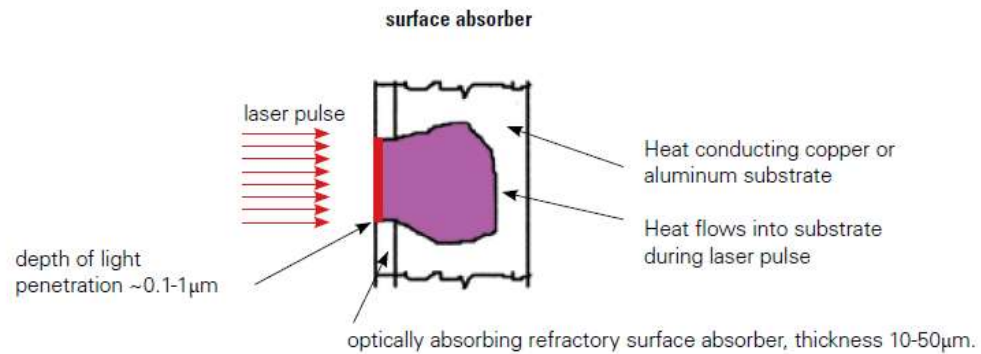


Fig. 5-14. The structure of the surface absorber (This picture is from the catalog of OPHIR Inc.).

From the analysis in the previous section, a layer of porous-like NSs/MSs is formed below the alumina surface for a BSB and the reflectance of the BSB is much lower than that of the original aluminum plate in the wavelength range of 280 nm to 2500 nm. When the spectrum range is from 400 nm to 840 nm, the reflectance is less than 20% and the flatness of reflectance curve is less than 0.5%. To some extent, a BSB has similar configuration with the surface absorber because the NSs/MSs layer can be utilized as the optically absorbing refractory surface absorber and the aluminum substrate part is exactly the same. The thin thickness of the NSs/MSs layer ($\sim 0.5 \mu\text{m} - 1 \mu\text{m}$) may lead to low power detection range. An alumina layer on the NSs/MSs surface which is transparent over 400 nm to 2500 nm will cause power loss. However, this layer can be used as the protective outer surface as the alumina has the features of corrosion resistance, electrical insulation and high surface smoothness and hardness [161,162], and thus it will enable the BSB to be work in tough environment.

Comparing with NSs/MSs produced using other methods such as electrochemical synthesis [173] and electrodeposited [175], etc., the location of the laser induced NSs/MSs have the superiority of to be edited or changed easily as required with

digital laser marking system.

5.6 SUMMARY

The application of blackening of a bulk Al alloy substrate with an alumina surface by a high power YDPFL is studied. Instead of using ultrafast (femtosecond or picosecond pulse) lasers to achieve NS/MS as many other research groups did, the NSs/MSs here are formed with a cost-efficient nanosecond YDPFL at 1064 nm wavelength.

The BSBs and the GSBs formed are characterized qualitatively and quantitatively. The CIE L^* value of the BSBs is much smaller than that of the GSBs and the laser fluence need to be controlled in an appropriate range together with the heating and cooling patterns to form the BSBs. The surface of the BSBs is as smooth as the original sample. The laser induced porous NS/MS layer which is responsible for the structural black color is formed and located beneath the alumina surface of the BSBs. The reflectance for both the BSB and GSB is much lower than the original sample from 280 nm to 2500 nm, and the BSB has the lowest reflectance in these optical spectrum ranges. The reflectance curves are fairly flat in visible light range for the BSB and GSB. The feasibility of this nanosecond pulsed fiber laser at 1 μm wavelength is proved. This cost-efficient nanosecond pulse fiber laser-induced blackening technique is useful for light power sensing, anti-reflective surface and surface decoration applications.

It is recognizable from this application that the pulse duration, pulse energy, pulse stability, and output laser beam quality are directly related to the final blackening effect. This, in turn, emphasizes the strong bond between the application and the laser design.

Chapter 6 CONCLUSIONS AND RECOMMENDATIONS FOR FUTURE WORK

6.1 CONCLUSIONS

In summary, this thesis focuses on the investigation of the high power YDPFLs at 1 μm wavelength region to achieve outstanding performance. The research mainly involves three subjects including the theoretical modeling and pulsed pump for high power YDPFLs, the design of high average power and high peak power YDPFLs, and the application by high power YDPFLs. The main achievements in terms of the analysis of the high power YDPFLs are summarized as follows.

- 1) After the introduction of the elements for high power YDPFLs and the literature review of YDPFL technology in Chapter 2, the pulsed pump method for suppress the ASE between pulses for high power YDPFLs has been studied in the first part of Chapter 3. In Section 3.2, by modeling the pulsed pump YDFA and numerically solving the rate equations, the most crucial factors in pulsed pump, P_p and t_p , are investigated. The results show that the P_p and t_p are directly related to the maximum reachable pulse energy and efficiency. In Section 3.3, a new pulsed pump design for ns YDPFLs with adjustable pulse repetition rate and pulse duration is proposed. For this pulsed pump scheme, the pump power (P_p) is kept at the maximal reachable pump power level or a fixed level, and the pump duration (t_p) for each seed pulse is modulated according to the pulse duration. The t_p is constant for every seed pulse with same pulse duration. When the pulse repetition rate is less than the threshold pulse repetition rate (f_t), the

peak power is enhanced and the inter-pulse ASE is suppressed. The experimental results show the efficiency is improved by ~10% at 2 kHz pulse repetition rate and ~6% at 5 kHz pulse repetition rate for long (130 ns) and short (20 ns) pulse duration respectively comparing with the CW pump scheme. For pulse repetition rate higher than f_t , the inter-pulse ASE is at a low level and the pulsed pump is hardly required by using higher P_P and shorter t_p . There is the same trend reached from both the numerical simulation and experimental results.

- 2) I dedicate Chapter 4 for the design of high power YDPFLs. Firstly, to characterize the laser pulse by considering the laser-material interaction, a new parameter, Usable Pulse Energy Ratio (UPER), to characterize the laser pulse of high power YDPFL is presented in Section 4.2. The UPER is defined as the ratio of the pulse energy of the part of the nanosecond laser pulse whose peak power is higher than the predefined ablation threshold power to the maximum reachable pulse energy. With this parameter, we understand whether the workpiece can be laser processed, how much pulse energy is wasted, and how wide is the heat affected zone (HAZ) after laser processing. There is severe pulse shape distortion for high power YDPFLs due to gain saturation. From material processing point of view, the higher the UPER, the less HAZ and side effect. One advantage associated with high power YDPFLs by directly modulated LD as seed laser followed by cascaded amplifier stages is the arbitrary seed pulse shape tuning feature. By using this feature, high power YDPFLs with three seed pulse shapes, rectangles, triangles, and rectangles with triangular tops (RWTT) have been experimentally investigated. With triangular

and RWTT seed laser, the UPER of the output laser pulse is less than that of the rectangular shape when the ablation threshold power is higher than 3 kW. However, it grows to 70.3% for the triangular seed pulse shape which is about 5% higher than that of the rectangular seed pulse shape at a lower ablation threshold power of 2 kW. The SBS and SRS, associated with the laser of these seed pulse shapes, have been discussed. SBS spikes are frequently generated with the laser of triangular seed pulse shape due to a significant deterioration of the SBS threshold caused by the narrow frequency spectrum of the smoothed leading edge of the triangular shape pulse. Then high average power and high peak power YDPFLs are designed in the following section.

- (a) High average power YDPFL. A novel high power MOPA YDPFL with an average output power of 160 W has been demonstrated. To mitigate the SRS component and enhance the pulse energy, a triangular seed pulse shape is adopted for the laser. Pulse energy of 1.45 mJ has been reached for the laser with 80 ns seed pulse. The power in the 1st Raman peak at ~ 1115 nm is at -20 dB compared to the center wavelength of the signal laser. To address SBS, especially when the laser is implemented with a triangular seed pulse shape, an SLED seed source with 3 dB optical spectrum of 20 nm, has been utilized to produce the seed pulses. The inter-pulse ASE, which is a potential risk when the YDPFL operating at low pulse repetition rate, has been suppressed through the pulsed pump method proposed in Section 3.3. The YDPFL operating with four pulse duration (80 ns, 56 ns, 34 ns and 10 ns) has been studied. UPERs for the laser with 34 ns seed pulse duration are largest with

higher than 8 kW ablation threshold power. For the ablation threshold power less than 5 kW, the laser with 80 ns has the higher UPERs. The optical-to-optical conversion efficiency of $\sim 67\%$ for the main amplifier and the 4σ beam quality (M^2) of 1.7 is obtained. The YDPFL in this section is a superior candidate for industrial applications requiring.

- (b) High peak power YDPFL. A high peak power YDPFL with adjustable pulse duration from 350 ps to hundreds of ns seeded by an SLED is demonstrated. The monolithic YDPFL is constructed with MOPA configuration which consists of three cascade amplifiers. A 1.2-m-length 40/200 μm LMA gain fiber and pump laser at 976 nm are used for the 3rd-amplifier stage. For the laser with 350 ps pulse duration, the seed laser generated through gain-switching technique, a peak power of 275 kW and pulse energy of 92 μJ is obtained. 90 ps jitter of the pulse duration is analyzed qualitatively. The ASE component of the YDPFL is investigated via an AOM and the laser proportion is $\sim 53\%$. For the laser with 183 ns seed pulse duration, the leading edge of the seed pulse is smoothed and pulse energy of 3.2 mJ and peak power of 137 kW is achieved. The $4\sigma M^2$ is 2.7 and 2.8 for the X and Y directions, respectively. Due to the ~ 20 nm optical spectrum of the SLED, SBS is avoided. Similar as the high average power YDPFL discussed in Section 4.3, the pulsed pump technique proposed is also implemented to this laser to suppress the inter-pulse ASE at pulse repetition rate.
- 3) YDPFLs are designed for certain applications. At the same time, the applications also feedback requirements for YDPFLs design. In Chapter 5, instead of using

the bulky and expensive ultrafast high power pulsed laser, blackening of a bulk Al alloy substrate with an alumina surface by using the high power ns YDPFL is achieved. The black square block (BSBs) and the gray square block (GSBs) formed are characterized qualitatively and quantitatively. The laser induced porous nanostructures/microstructures (NS/MS) layer which is responsible for the structural black color is formed and located beneath the alumina surface of the BSBs. The NSs/MSs layer is suggested to be responsible for the structural color. The reflectance for the BSB surface is much lower than that of the original sample from 280 nm to 2500 nm and the uniform of it is less than 0.5% in visible light range. The feasibility of this application is investigated and proved. This cost-efficient nanosecond pulse fiber laser-induced blackening technique is useful for light power sensing, anti-reflective surface and surface decoration applications.

6.2 RECOMMENDATION FOR FUTURE WORK

The studies described in the thesis suggest some interesting directions to pursue for the future work.

6.2.1 High peak power YDPFLs with LMA PCF

For high peak power YDPFL, the peak power of the laser pulse is limited due to SRS. One way to deal with it is to use LMA fiber, however, the larger fiber core results in degradation of the output laser beam quality.

As discussed in Chapter 2, the optical properties of the material are altered by the regular morphology of the microstructures incorporated into the material [115]. And the NA and uniformity of a PCF can be precisely controlled by tuning the size of the embedded holes and the pitching between holes [117]. This makes it possible to fabricate a PCF core with large diameter but very low NA . The manufacturing single-mode PCFs with core diameter from 10 μm to more than 100 μm are feasible after carefully design the cladding structures and the high order mode normally experience higher losses or less overlap with the core region during the propagation.

By using such an LMA PCF to construct the final amplifier stage, the pulse energy and the peak power can be greatly enhanced without degrading the beam quality. As an example, the performance of YDPFL will be improved by using LMA PCF for pulsed fiber lasers that are seeded by SLEDs in Chapter 4. PCF splicing, output laser delivery and pump laser coupling etc. require special consideration, especially for industrial applications with reliability requirements.

6.2.2 High power UV laser seeded with YDPFL

From an industrial application point of view, some materials and processes such as plastics, flexible printed circuits cutting, and Polyethylene terephthalate material etc., can achieve the desired effect by the laser with green or UV wavelengths instead of 1 μm wavelength.

Due to the superiority of direct modulation technique, high power green lasers or UV lasers inoculated with YDPFL sources with adjustable pulse duration and pulse repetition rate will be an interesting topic for further study. As demonstrated in Chapter 4, the pulse

duration can be narrowed down to tens or hundreds of ps region by gain switch technique depending on the laser diode.

If ultrafast laser pulses, such as in fs region, are needed, the ultrashort UV laser can be achieved through the fiber laser source with mode lock technique. The side effect is the pulse duration can only be tuned in a relatively small region through FBG.

If ultrafast laser pulses are required, such as in the fs region, ultrashort UV lasers can be realized by fiber laser sources through mode lock techniques. The side effect is that the pulse duration can only be adjusted by the FBG in a relatively small region.

Reference

- [1] Gloge D. Optical Fibers for Communication. *Applied Optics*, 1974, 13(2):249-54.
- [2] Hubbard W M. Double-Reverse-Scatter Interference in Optical Fiber Communication Systems. *Applied Optics*, 1972, 11(11):2495-501.
- [3] Snitzer E. Optical Maser Action of Nd³⁺ in a Barium Crown Glass. *Physical Review Letters*, 1961, 7(12):444-446.
- [4] Koester C J, Snitzer E. Amplification in a fiber laser. *Applied Optics*, 1964, 3(10): 1182-1186.
- [5] <http://www.industrial-lasers.com/articles/print/volume-31/issue-1/features/2015-industrial-laser-market-outperforms-global-manufacturing-instability.html>.
- [6] Snitzer E. Proposed fiber cavities for optical masers. *Journal of Applied Physics*, 1961, 32(1): 36-39.
- [7] Jauregui C, Limpert J, Tünnermann A. High-power fiber lasers. *Nature photonics*, 2013, 7(11): 861-867.
- [8] Brown D C, Hoffman H J. Thermal, stress, and thermo-optic effects in high average power double-clad silica fiber lasers. *IEEE Journal of quantum electronics*, 2001, 37(2): 207-217.
- [9] Kratky A, Schuöcker D, Liedl G. Processing with kW fiber lasers: advantages and limits. XVII International Symposium on Gas Flow and Chemical Lasers and High Power Lasers. International Society for Optics and Photonics, 2008: 71311X-71311X-12.
- [10] Pavlov I, Dülgergil E, Ilbey E, et al. Diffraction-limited, 10-W, 5-ns, 100-kHz, all-fiber laser at 155 μm . *Optics letters*, 2014, 39(9): 2695-2698.
- [11] Rao Y J, Zhang W L, Zhu J M, et al. Hybrid lasing in an ultra-long ring fiber laser. *Optics express*, 2012, 20(20): 22563-22568.
- [12] Kobtsev S, Kukarin S, Fedotov Y. Ultra-low repetition rate mode-locked fiber laser with high-energy pulses. *Optics express*, 2008, 16(26): 21936-21941.
- [13] Chen Y F, Tsai S W. Simultaneous Q-switching and mode-locking in a diode-pumped Nd: YVO 4-Cr 4+: YAG laser. *Quantum Electronics, IEEE Journal of*, 2001, 37(4): 580-586.
- [14] Sotor J, Sobon G, Abramski K M. Sub-130 fs mode-locked Er-doped fiber laser based on topological insulator. *Optics Express*, 2014, 22(11): 13244-13249.
- [15] Lederer M J, Luther-Davies B, Tan H H, et al. Multipulse operation of a Ti: sapphire laser mode locked by an ion-implanted semiconductor saturable-absorber mirror. *JOSA B*, 1999, 16(6): 895-904.

- [16] Jeong Y, Nilsson J, Sahu J K, et al. Power scaling of single-frequency ytterbium-doped fiber master-oscillator power-amplifier sources up to 500 W. *Selected Topics in Quantum Electronics, IEEE Journal of*, 2007, 13(3): 546-551.
- [17] Michalis N. Zervas and Christophe A. Codemard. High Power Fiber Lasers: A Review. *IEEE Journal of Selected Topics in Quantum Electronics*, 2014, 20(5): 0904123
- [18] Röser F, Rothhard J, Ortac B, et al. 131 W 220 fs fiber laser system. *Optics letters*, 2005, 30(20): 2754-2756.
- [19] Stutzki F, Jansen F, Liem A, et al. 26 mJ, 130 W Q-switched fiber-laser system with near-diffraction-limited beam quality. *Optics letters*, 2012, 37(6): 1073-1075.
- [20] Kanzelmeyer S, Sayinc H, Theeg T, et al. All-fiber based amplification of 40 ps pulses from a gain-switched laser diode. *Optics express*, 2011, 19(3): 1854-1859.
- [21] Lago L, Mussot A, Douay M, et al. Single-mode narrow-bandwidth temporally shaped nanosecond-pulse ytterbium-doped fiber MOPA for a large-scale laser facility front-end. *Journal of the Optical Society of America B*, 2010, 27(11):2231-2236.
- [22] Vu K T, Malinowski A, Richardson D J, et al. Adaptive pulse shape control in a diode-seeded nanosecond fiber MOPA system. *Optics Express*, 2006, 14(23): 10996-11001.
- [23] Chen S P, Chen H W, Hou J, et al. 100 W all fiber picosecond MOPA laser. *Optics express*, 2009, 17(26): 24008-24012.
- [24] Teodoro F D. Multi-MW peak power, single transverse mode operation of a 100 micron core diameter, Yb-doped photonic crystal rod amplifier. *Proceedings of SPIE - The International Society for Optical Engineering*, 2007:645318-645318-5.
- [25] Limpert J, Roser F, Schimpf D N, et al. High repetition rate gigawatt peak power fiber laser systems: challenges, design, and experiment. *Selected Topics in Quantum Electronics, IEEE Journal of*, 2009, 15(1): 159-169.
- [26] Eidam T, Rothhardt J, Stutzki F, et al. Fiber chirped-pulse amplification system emitting 3.8 GW peak power. *Optics express*, 2011, 19(1): 255-260.
- [27] Eidam T, Wirth C, Jauregui C, et al. Experimental observations of the threshold-like onset of mode instabilities in high power fiber amplifiers. *Optics express*, 2011, 19(14): 13218-13224.
- [28] Bedö S, Lüthy W, Weber H P. The effective absorption coefficient in double-clad fibers. *Optics communications*, 1993, 99(5): 331-335.
- [29] Snitzer E, Po H, Hakimi F, et al. Double clad, offset core Nd fiber laser, *Optical Fiber Sensors*. 1988, PD5.
- [30] Po H, Snitzer E, Tumminelli R, et al. Double clad high brightness Nd fiber laser pumped by GaAlAs phased array. 1989, PD7.
- [31] Liu A, Song J, Kamatani K, et al. Rectangular double-clad fiber laser with two-end-bundled pump. *Electronics Letters*, 1996, 32(18): 1673-1674.

- [32] Martínezrios A, Starodumov A N, Po H, et al. Efficient operation of double-clad Yb³⁺-doped fiber lasers with a novel circular cladding geometry. *Optics Letters*, 2003, 28(18):1642-1644.
- [33] Liu A, Ueda K. The absorption characteristics of circular, offset, and rectangular double-clad fibers. *Optics Communications*, 1996, 132(5): 511-518.
- [34] Wadsworth W, Percival R M, Bouwmans G, et al. High power air-clad photonic crystal fiber laser. *Optics express*, 2003, 11(1): 48-53.
- [35] Po H, Cao J D, Laliberte B M, et al. High power neodymium-doped single transverse mode fiber laser. *Electronics Letters*, 1993, 29(17):1500-1501.
- [36] Zellmer H, Unger S, Albers P, et al. High-power cw neodymium-doped fiber laser operating at 9.2 W with high beam quality. *Optics letters*, 1995, 20(6): 578-580.
- [37] Dominic V, MacCormack S, Waarts R, et al. 110 W fiber laser. *Electronics Letters*, 1999, 35(14): 1158-1160.
- [38] Jeong Y, Sahu J, Payne D, et al. Ytterbium-doped large-core fiber laser with 1.36 kW continuous-wave output power. *Optics Express*, 2004, 12(25): 6088-6092.
- [39] IPG Photonics Corporation. IPG Photonics successfully tests world's first 10 kilowatt single-mode production laser. *Laser Focus World*, 2009.
- [40] Etzel H W, Gandy H W, Ginther R J. Stimulated emission of infrared radiation from ytterbium activated silicate glass. *Applied Optics*, 1962, 1(4): 534-536.
- [41] Streifer W, Scifres D R, Harnagel G L, et al. Advances in diode laser pumps. *IEEE journal of quantum electronics*, 1988, 24: 883-894.
- [42] Wu M C, Olsson N A, Sivco D, et al. A 970 nm strained-layer InGaAs/GaAlAs quantum well laser for pumping an erbium-doped optical fiber amplifier. *Applied physics letters*, 1990, 56(3): 221-223.
- [43] Hanna D C, Perry I R, Smart R G, et al. Efficient superfluorescent emission at 974 nm and 1040 nm from an Yb-doped fiber. *Optics communications*, 1989, 72(3): 230-234.
- [44] Allain J Y, Monerie M, Poignant H. Ytterbium-doped fluoride fiber laser operating at 1.02 μ m. *Electronics Letters*, 1992, 28(11):988-989.
- [45] Paschotta R, Nilsson J, Tropper A C, et al. Ytterbium-doped fiber amplifiers. *IEEE journal of Quantum Electronics*, 1997, 33(7): 1049-1056.
- [46] Miniscalco W J, Quimby R S. General procedure for the analysis of Er³⁺ cross sections. *Optics letters*, 1991, 16(4): 258-260.
- [47] Pask H M, Carman R J, Hanna D C, et al. Ytterbium-doped silica fiber lasers: versatile sources for the 1-1.2 μ m region. *Selected Topics in Quantum Electronics*, *IEEE Journal of*, 1995, 1(1): 2-13.
- [48] Krupke W F. Ytterbium solid-state lasers. The first decade. *Selected Topics in Quantum Electronics*, *IEEE Journal of*, 2000, 6(6): 1287-1296.

- [49] Pask H M, Archambault J L, Hanna D C, et al. Operation of cladding-pumped Yb³⁺-doped silica fiber lasers in 1 μ m region. *Electronics letters*, 1994, 30(11).
- [50] Kirchhof J, Unger S, Schwuchow A, et al. Materials for high-power fiber lasers. *Journal of non-crystalline solids*. 2006, 352(23): 2399-2403.
- [51] Paschotta R, Nilsson J, Barber P R, et al. Lifetime quenching in Yb-doped fibers. *Optics Communications*, 1997, 136(5): 375-378.
- [52] Burshtein Z, Kalisky Y, Levy S Z, et al. Impurity local phonon nonradiative quenching of Yb³⁺ fluorescence in ytterbium-doped silicate glasses. *Quantum Electronics, IEEE Journal of*, 2000, 36(8): 1000-1007.
- [53] Hanna D C, Perry I R, Smart R G, et al. Efficient super fluorescent emission at 974 nm and 1040 nm from an Yb-doped fiber. *Optics communications*, 1989, 72(3): 230-234.
- [54] Richardson D J, Nilsson J, Clarkson W A. High power fiber lasers: current status and future perspectives [Invited]. *Journal of the Optical Society of America B*, 2010, 27(11):B63-B92.
- [55] Stuart B C, Feit M D, Rubenchik A M, et al. Laser-induced damage in dielectrics with nanosecond to subpicosecond pulses. *Physical Review Letters*, 1995, 74(12):2248-2251.
- [56] Smith A V, Do B T. Bulk and surface laser damage of silica by picosecond and nanosecond pulses at 1064 nm. *Applied optics*, 2008, 47(26): 4812-4832.
- [57] Smith A V, Do B T, Hadley G R, et al. Optical damage limits to pulse energy from fibers. *IEEE Journal of Selected Topics in Quantum Electronics*, 2009, 15(1):153-158.
- [58] Shen N, Bude J D, Carr C W. Model laser damage precursors for high quality optical materials. *Optics express*, 2014, 22(3): 3393-3404.
- [59] Stuart B C, Feit M D, Herman S, et al. Nanosecond-to-femtosecond laser-induced breakdown in dielectrics. *Physical Review B*, 1996, 53(4): 1749.
- [60] Stolen R H, Lin C. Self-phase-modulation in silica optical fibers. *Physical Review A*, 1978, 17(4): 1448.
- [61] Fibich G, Gaeta A L. Critical power for self-focusing in bulk media and in hollow waveguides. *Optics letters*, 2000, 25(5): 335-337.
- [62] Zervas M N. High power ytterbium-doped fiber lasers—fundamentals and applications. *International Journal of Modern Physics B*, 2014, 28(12).
- [63] Smith A V, Do B T, Hadley G R, et al. Optical damage limits to pulse energy from fibers. *Selected Topics in Quantum Electronics, IEEE Journal of*, 2009, 15(1): 153-158.
- [64] Govind P. Agrawal, *Nonlinear Fiber Optics*. fourth edition.
- [65] Ferreira M F S. Nonlinear effects in optical fibers: limitations and benefits. *International Workshop and Conference on Photonics and Nanotechnology 2007. International Society for Optics and Photonics*, 2008: 679302-679302-9.

- [66] Petrov M P, Kiyon R V, Kuzin E A, et al. Gain saturation in three-and four-level fiber amplifiers. *Optics communications*, 1994, 109(5): 499-506.
- [67] Rigrod W. Saturation Effects in High-Gain Lasers. *Journal of Applied Physics*, 1965, 36(8): 2487-2490.
- [68] Parvin P, Ilchi-Ghazaani M, Bananej A, et al. Small signal gain and saturation intensity of a Yb: Silica fiber MOPA system. *Optics & Laser Technology*, 2009, 41(7): 885-891.
- [69] Smith R G. Optical power handling capacity of low loss optical fibers as determined by stimulated Raman and Brillouin scattering. *Applied Optics*, 1972, 11(11): 2489-2494.
- [70] Cotter D. Transient stimulated Brillouin scattering in long single-mode fibers. *Electronics Letters*, 1982, 18(12): 504-506.
- [71] Di Teodoro F, Morais J, McComb T S, et al. SBS-managed high-peak-power nanosecond-pulse fiber-based master oscillator power amplifier. *Optics letters*, 2013, 38(13): 2162-2164.
- [72] Mungan C E, Rogers S D, Satyan N, et al. Time-dependent modeling of Brillouin scattering in optical fibers excited by a chirped diode laser. *Quantum Electronics, IEEE Journal of*, 2012, 48(12): 1542-1546.
- [73] White J O, Vasilyev A, Cahill J P, et al. Suppression of stimulated Brillouin scattering in optical fibers using a linearly chirped diode laser. *Optics express*, 2012, 20(14): 15872-15881.
- [74] Petersen E, Yang Z Y, Satyan N, et al. Stimulated Brillouin scattering suppression with a chirped laser seed: comparison of dynamical model to experimental data. *IEEE Journal of Quantum Electronics*, 2014, 49(12):1040-1044.
- [75] Di Teodoro F, Morais J, McComb T S, et al. SBS-managed high peak power nanosecond-pulse fiber-based master oscillator power amplifier. *Optics letters*, 2013, 38(13): 2162-2164.
- [76] White J O, Vasilyev A, Cahill J P, et al. Suppression of stimulated Brillouin scattering in optical fibers using a linearly chirped diode laser. *Optics express*, 2012, 20(14): 15872-15881.
- [77] Dong L. Formulation of a complex mode solver for arbitrary circular acoustic waveguides. *Journal of Lightwave Technology*, 2010, 28(21): 3162-3175.
- [78] Engelbrecht R. Analysis of SBS Gain Shaping and Threshold Increase by Arbitrary Strain Distributions. *Journal of Lightwave Technology*, 2014, 32(9): 1689-1700.
- [79] Boggio J M, Marconi J D, Fragnito H L. Experimental and numerical investigation of the SBS-threshold increase in an optical fiber by applying strain distributions. *Journal of lightwave technology*, 2005, 23(11): 3808.
- [80] Yoshizawa N, Imai T. Stimulated Brillouin scattering suppression by means of applying strain distribution to fiber with cabling. *Lightwave Technology, Journal of*, 1993, 11(10): 1518-1522.

- [81] Hansryd J, Dross F, Westlund M, et al. Increase of the SBS threshold in a short highly nonlinear fiber by applying a temperature distribution. *Journal of lightwave technology*, 2001, 19(11): 1691.
- [82] Lee H, Agrawal G. Suppression of stimulated Brillouin scattering in optical fibers using fiber Bragg gratings. *Optics express*, 2003, 11(25): 3467-3472.
- [83] Cotter D. Stimulated Brillouin scattering in monomode optical fiber. *Journal of Optical Communications*, 1983, 4(1): 10-19.
- [84] Kobayakov A, Kumar S, Chowdhury D, et al. Design concept for optical fibers with enhanced SBS threshold. *Optics Express*, 2005, 13(14): 5338-5346.
- [85] Gray S, Walton D T, Chen X, et al. Optical fibers with tailored acoustic speed profiles for suppressing stimulated Brillouin scattering in high-power, single-frequency sources. *IEEE Journal of Selected Topics in Quantum Electronics*, 2009, 15(1): 37.
- [86] Krishnan K S. A New Type of Secondary Radiation. *Nature*, 1927, 121(3048):501-502.
- [87] Stolen R H, Gordon J P, Tomlinson W J, et al. Raman response function of silica-core fibers. *JOSA B*, 1989, 6(6): 1159-1166.
- [88] Spence D J, Zhao Y, Jackson S D, et al. An investigation into Raman mode locking of fiber lasers. *Optics express*, 2008, 16(8): 5277-5289
- [89] Mamdoohi G, Sarmani A R, Abas A F, et al. 20 GHz spacing multi-wavelength generation of Brillouin-Raman fiber laser in a hybrid linear cavity. *Optics express*, 2013, 21(16): 18724-18732.
- [90] Bernier M, Fortin V, El-Amraoui M, et al. 3.77 μm fiber laser based on cascaded Raman gain in a chalcogenide glass fiber. *Optics letters*, 2014, 39(7): 2052-2055.
- [91] Freudiger C W, Yang W, Holtom G R, et al. Stimulated Raman scattering microscopy with a robust fiber laser source. *Nature Photonics*, 2014, 8(2): 153-159.
- [92] Fini J M, Mermelstein M D, Yan M F, et al. Distributed suppression of stimulated Raman scattering in an Yb-doped filter-fiber amplifier. *Optics letters*, 2006, 31(17): 2550-2552.
- [93] Nolan D A, Berkey G E, Li M J, et al. Single-polarization fiber with a high extinction ratio. *Optics letters*, 2004, 29(16): 1855-1857.
- [94] Zenteno L, Wang J, Walton D, et al. Suppression of Raman gain in single-transverse-mode dual-hole-assisted fiber. *Optics express*, 2005, 13(22): 8921-8926.
- [95] Jansen F, Nodop D, Jauregui C, et al. Modeling the inhibition of stimulated Raman scattering in passive and active fibers by lumped spectral filters in high power fiber laser systems. *Optics express*, 2009, 17(18): 16255-16265.
- [96] Nodop D, Jauregui C, Jansen F, et al. Suppression of stimulated Raman scattering employing long period gratings in double-clad fiber amplifiers. *Optics letters*, 2010, 35(17): 2982-2984.
- [97] Alkeskjold T T. Large-mode-area ytterbium-doped fiber amplifier with distributed narrow spectral filtering and reduced bend sensitivity. *Optics express*, 2009, 17(19): 16394-16405.

- [98] Brooks C D, Di Teodoro F. Multimegawatt peak-power, single-transverse-mode operation of a 100 μm core diameter, Yb-doped rodlike photonic crystal fiber amplifier. *Applied Physics Letters*, 2006, 89(11): 111119-111119-3.
- [99] Limpert J, Schmidt O, Rothhardt J, et al. Extended single-mode photonic crystal fiber lasers. *Optics express*, 2006, 14(7): 2715-2720.
- [100] Eidam T, Hanf S, Seise E, et al. Femtosecond fiber CPA system emitting 830 W average output power. *Optics letters*, 2010, 35(2): 94-96.
- [101] Wirth C, Schreiber T, Rekas M, et al. High-power linear-polarized narrow linewidth photonic crystal fiber amplifier. *International Society for Optics and Photonics*, 2010: 75801H-75801H-6.
- [102] Hansen K R, Alkeskjold T T, Broeng J, et al. Theoretical analysis of mode instability in high-power fiber amplifiers. *Optics express*, 2013, 21(2): 1944-1971.
- [103] Eidam T, Wirth C, Jauregui C, et al. Experimental observations of the threshold-like onset of mode instabilities in high power fiber amplifiers. *Optics express*, 2011, 19(14): 13218-13224.
- [104] Smith A V, Smith J J. Influence of pump and seed modulation on the mode instability thresholds of fiber amplifiers. *Optics express*, 2012, 20(22): 24545-24558.
- [105] Smith A V, Smith J J. Mode instability in high power fiber amplifiers. *Optics express*, 2011, 19(11): 10180-10192.
- [106] Jauregui C, Eidam T, Otto H J, et al. Temperature-induced index gratings and their impact on mode instabilities in high-power fiber laser systems. *Optics express*, 2012, 20(1): 440-451.
- [107] Hansen K R, Alkeskjold T T, Broeng J, et al. Thermally induced mode coupling in rare-earth doped fiber amplifiers. *Optics letters*, 2012, 37(12): 2382-2384.
- [108] Laurila M, Jørgensen M M, Hansen K R, et al. Distributed mode filtering rod fiber amplifier delivering 292W with improved mode stability. *Optics express*, 2012, 20(5): 5742-5753.
- [109] Jauregui C, Otto H J, Stutzki F, et al. Passive mitigation strategies for mode instabilities in high-power fiber laser systems. *Optics express*, 2013, 21(16): 19375-19386.
- [110] Smith A V, Smith J J. Increasing mode instability thresholds of fiber amplifiers by gain saturation. *Optics express*, 2013, 21(13): 15168-15182.
- [111] Alkeskjold T. T., Laurila M., Weirich J., et al. Photonic crystal fiber amplifiers for high power ultrafast fiber lasers. *Nanophotonics*, 2013, 2(5-6):369-381.
- [112] Koplow JP, Kliner DAV, Goldberg L. Single-mode operation of a coiled multimode fiber amplifier. *Optics Letters* 2000, 25:442-4.
- [113] Fini J. Bend-resistant design of conventional and microstructure fibers with very large mode area. *Optics Express*, 2006;14:69-81.
- [114] Russell P. Photonic crystal fibers. Peking University Press, 2013.

- [115] Knight J C. Photonic crystal fibers. *Nature*, 2008, 7134(6950):847-51.
- [116] F. Benabid, P.J. Roberts. Linear and nonlinear optical properties of hollow core photonic crystal fiber. *Journal of Modern Optics*, 2011, 58(2):87-124.
- [117] Mortensen N. A., Folken J. R, Skovgaard P. M. W., et al. Numerical Aperture of Single-Mode Photonic Crystal Fibers. *IEEE Photonics Technology Letters*, 2002, 14(8):1094-1096.
- [118] Huang X, Guo B, Yang W, et al. Pulsed-pumped optical fiber amplifier. *Chinese optics letters*, 2009, 7(8):712-714.
- [119] Zhang H, Shen X, Chen D, et al. High Energy and High Peak Power Nanosecond Pulses Generated by Fiber Amplifier. *IEEE Photonics Technology Letters*, 2014, 26(22):2295-2298.
- [120] Wang Y, Hong P. Dynamic characteristics of double-clad fiber amplifiers for high-power pulse amplification. *Lightwave Technology Journal of*, 2003, 21(10):2262-2270.
- [121] Schmidt, O., C. Wirth, I. Tsybin, T. Schreiber, R. Eberhardt, J. Limpert, and A. Tünnermann. Average power of 1.1 kW from spectrally combined, fiber-amplified, nanosecond-pulsed sources. *Optics letters* 34, no. 10 (2009): 1567-1569.
- [122] Wei T, Tan Z, Li J, et al. Theoretical and experimental study of the pump pulse width optimization of the Yb-doped fiber amplifier. *Optik*, 2013, 124(16):2459-2462.
- [123] Malinowski A, Price J H V, Zervas M N. Sub-Microsecond Pulsed Pumping as a Means of Suppressing Amplified Spontaneous Emission in Tandem Pumped Fiber Amplifiers. *Quantum Electronics IEEE Journal of*, 2015, 51(12):1-7.
- [124] Williams E, Brousseau E B, Rees A. Nanosecond Yb fiber laser milling of aluminium: effect of process parameters on the achievable surface finish and machining efficiency. *The International Journal of Advanced Manufacturing Technology*, 2014, 74(5):769-780.
- [125] Kaakkunen J, Laakso P, Vanttaja I. Fast Micromachining Using Spatial Light Modulator and Galvanometer Scanner with Infrared Pulsed Nanosecond Fiber Laser. *Journal of Laser Micro*, 2014, 9(1):10-10.
- [126] Tan N N, Hung D T, Anh V T, et al. Improved patterning of ITO coated with gold masking layer on glass substrate using nanosecond fiber laser and etching. *Applied Surface Science*, 2015, 336:163-169.
- [127] Fang Q, Shi W, Fan J. 700-kW-Peak-Power Monolithic Nanosecond Pulsed Fiber Laser. *Photonics Technology Letters IEEE*, 2014, 26(16):1676-1678.
- [128] Köchner.W, *Solid-State Laser Engineering*, 6th Revised and Updated ed., USA: Springer, 1999, pp. 681-700.
- [129] Benavides O, Lebedeva O, Golikov V. Reflection of nanosecond Nd:YAG laser pulses in ablation of metals. *Optics Express*, 2011, 19(22):21842-8.
- [130] Benavides O, May L L, Gil A F. A comparative study on reflection of nanosecond Nd-YAG laser pulses in ablation of metals in air and in vacuum. *Optics Express*, 2013, 21(11):13068-74.

- [131] Wang B, Gallais L. A theoretical investigation of the laser damage threshold of metal multi-dielectric mirrors for high power ultrashort applications. *Optics express*, 2013, 21(12): 14698-14711.
- [132] Slezak O, Yasuhara R, Lucianetti A, et al. Wavelength dependence of magneto-optic properties of terbium gallium garnet ceramics. *Optics Express*, 2015, 23(10):13641-7.
- [133] Snetkov I L, Voitovich A V, Palashov O V, et al. Review of Faraday Isolators for Kilowatt Average Power Lasers. *Quantum Electronics IEEE Journal of*, 2014, 50(6):434-443.
- [134] Yoshida H, Tsubakimoto K, Fujimoto Y, et al. Optical properties and Faraday effect of ceramic terbium gallium garnet for a room temperature Faraday rotator. *Optics Express*, 2011, 19(16):15181-7.
- [135] 1030-1064nm Faraday Rotators and Isolators. Available: https://www.newport.com/medias/sys_master/images/images/hdd/h07/8796960751646/1030-1064nm-Faraday-Isolators-Datasheet.pdf.
- [136] Micromachining SPWI. Shorter pulse widths improve micromachining. *About Us*, 2013.
- [137] Li Z, Heidt A M, Teh P S, et al. High-energy diode-seeded nanosecond 2 μ m fiber MOPA systems incorporating active pulse shaping. *Optics letters*, 2014, 39(6): 1569-1572.
- [138] Teh P S, Alam S, Shepherd D P, et al. Generation of mode-locked optical pulses at 1035 nm from a fiber Bragg grating stabilized semiconductor laser diode. *Optics Express*, 2014, 22(11): 13366-13373.
- [139] Malinowski A, Vu K T, Chen K K, et al. High power pulsed fiber MOPA system incorporating electro-optic modulator based adaptive pulse shaping. *Optics express*, 2009, 17(23): 20927-20937.
- [140] Dajani I, Zeringue C, Shay T M. Investigation of Nonlinear Effects in Multitone-Driven Narrow-Linewidth High-Power Amplifiers. *IEEE Journal of Selected Topics in Quantum Electronics*, 2009, 15(2):406-414.
- [141] Morasse B, Chatigny S, Gagnon É, et al. Enhanced pulseshaping capabilities and reduction of non-linear effects in all-fiber MOPA pulsed system. *Lasers and Applications in Science and Engineering*. International Society for Optics and Photonics, 2009: 71951D-71951D-12.
- [142] Zibik, E. A., Sverdlov, B., Mohrdiek, S., Troger, J., Pawlik, S., Pfeiffer, H. U., & Lichtenstein, N. (2010, February), Novel single-mode fiber coupled broadband seed source for pulsed fiber laser systems, In *OPTO* (pp. 76161K-76161K). International Society for Optics and Photonics.
- [143] Kafar A, Stanczyk S, Targowski G, et al, High-optical-power InGaN superluminescent diodes with j-shape waveguide, *Applied Physics Express*, vol. 6, no. 9, pp. 092102, 2013.
- [144] Limpert J, Höfer S, Liem A, et al. 100-W average-power, high-energy nanosecond fiber amplifier. *Applied Physics B*, 2002, 75(4):477-479.

- [145] Schaaf P, Han M, Lieb K P, et al. Laser nitriding of iron with laser pulses from femtosecond to nanosecond pulse duration. *Applied physics letters*, 2002, 80(6): 1091-1093.
- [146] Zhang H, Wang X, Zhou P, et al. 6 mJ, high-average-power, all-fiberized Q-switched fiber master oscillator power amplifier with low repetition rate. *Applied Optics*, 2012, 51(29):6933-6.
- [147] Renaud C C, Alvarez-Chavez J A, Sahu J K, et al. 7.7 mJ pulses from a large core Yb-doped cladding pumped Q-switched fiber laser. *Lasers and Electro-Optics*, 2001.
- [148] Vorobyev A. Y., Guo C. Direct femtosecond laser surface nano/microstructuring and its applications. *Laser & Photonics Reviews*, 2013, 7(3):385–407.
- [149] Stephen Hypsh, Geoff Shannon. Femtosecond laser processing of metal and plastics in the medical device industry, *Industry Laser Solutions*, 2014.
- [150] Gomes L A, Orsila L, Jouhti T, et al. Picosecond SESAM-based ytterbium mode-locked fiber lasers. *IEEE Journal of Selected Topics in Quantum Electronics*, 2004, 10(1):129-136.
- [151] Liu H, Gao C, Tao J, et al. Compact tunable high power picosecond source based on Yb-doped fiber amplification of gain switch laser diode. *Optics Express*, 2008, 16(11):7888-93.
- [152] Teh P S, Lewis R J, Alam S U, et al. 200 W Diffraction limited, single-polarization, all-fiber picosecond MOPA. *Optics Express*, 2013, 21(22):25883-9.
- [153] Yokoyama Y, Kan T, Kageyama T, et al. 1064-nm DFB laser diode modules applicable to seeder for pulse-on-demand fiber laser systems. *Optical Fiber Technology*, 2014, 20(6):714-724.
- [154] Sano E, Shinagawa M, Takahashi R. Theoretical analysis of timing jitter in gain-switched semiconductor lasers. *Applied Physics Letters*, 1989, 55(6):522-524.
- [155] Wada K, Kitagawa N, Matsukura S, et al. Timing and amplitude jitter in a gain-switched multimode semiconductor laser. *Japanese Journal of Applied Physics*, 2016, 55(4):042702.
- [156] Lee S H, Kim K H, Deshmukh V M, et al. Injection Laser Wavelength-Dependent Timing Jitter Reduction of Gain-Switched Single-Mode VCSELs. *IEEE Journal of Quantum Electronics*, 2010, 46(9):1327-1331.
- [157] Li Z L, Zheng H Y, Teh K M, et al. Analysis of oxide formation induced by UV laser coloration of stainless steel. *Applied Surface Science*, 2009, 256(5):1582-1588.
- [158] Dusser B, Sagan Z, Soder H, et al. Controlled nanostructures formation by ultra-fast laser pulses for color marking. *Optics Express*, 2010, 18(3):2913-24.
- [159] Stratakis E, Zorba V, Barberoglou M, et al. Femtosecond laser writing of nanostructures on bulk Al via its ablation in air and liquids. *Applied Surface Science*, 2009, 255(10):5346-5350.
- [160] Veiko V, Odintsova G, Ageev E, et al. Controlled oxide films formation by nanosecond laser pulses for color marking. *Optics Express*, 2014, 22(20):24342-24347.

- [161] Bartzsch H, Glöß D, Böcher B, et al. Properties of SiO₂, and Al₂O₃, films for electrical insulation applications deposited by reactive pulse magnetron sputtering. *Surface & Coatings Technology*, 2003, 174(03):774-778.
- [162] Nie X, Meletis E I, Jiang J C, et al. Abrasive wear/corrosion properties and TEM analysis of Al₂O₃, coatings fabricated using plasma electrolysis. *Surface & Coatings Technology*, 2002, 149(2-3):245-251.
- [163] Huang H, Liu J. Femtosecond fiber laser based metal blackening. *Optical Engineering Applications*. International Society for Optics and Photonics, 2013:201-216.
- [164] Zhang B M, Liu M, Shum P P, et al. Design and fabrication of 100 kW peak power picosecond fiber laser for efficient laser marking and drilling. *Photonics Conference*. IEEE, 2015:70-71.
- [165] McLaren K. XIII—The Development of the CIE 1976 (L* a* b*) Uniform Colour Space and Colour-difference Formula. *Coloration Technology*, 1976, 92(9):338-341.
- [166] Wang J, Wang C W, Li Y, et al. Optical constants of anodic aluminum oxide films formed in oxalic acid solution. *Thin Solid Films*, 2008, 516(21):7689-7694.
- [167] Wu B. High-intensity nanosecond-pulsed laser-induced plasma in air, water, and vacuum: A comparative study of the early-stage evolution using a physics-based predictive model. *Applied Physics Letters*, 2008, 93(10):101104-101104-3.
- [168] Zhang C, Yao J, Lan S, et al. Effects of plasma confinement on the femtosecond laser ablation of silicon. *Optics Communications*, 2013, 308(11):54-63.
- [169] Bulgakova N M, Bulgakov A V. Pulsed laser ablation of solids: transition from normal vaporization to phase explosion. *Applied Physics A*, 2001, 73(2):199-208.
- [170] Zhang Z M, Lefever-Button G, Powell F R. Infrared Refractive Index and Extinction Coefficient of Polyimide Films. *International Journal of Thermophysics*, 1998, 19(3):905-916.
- [171] Lenert A, Bierman D M, Nam Y, et al. A nanophotonic solar thermophotovoltaic device. *Nature Nanotechnology*, 2014, 9(2):126-30.
- [172] Hochbaum A I, Chen R, Delgado R D, et al. Enhanced thermoelectric performance of rough silicon nanowires. *ChemInform*, 2008, 39(14):163-167.
- [173] Yu R, Lin Q, Leung S F, et al. Nanomaterials and nanostructures for efficient light absorption and photovoltaics. *Nano Energy*, 2012, 1(1):57-72.
- [174] Complete power/energy meter and beam profilers catalog. [online]. available: <http://www.ophiropt.com/laser-measurement-instruments/laser-power-energy-meters/services/catalog-download?r=drp>.
- [175] Lizama-Tzec F I, Macías J D, Estrella-Gutiérrez M A, et al. Electrodeposition and characterization of nanostructured black nickel selective absorber coatings for solar-thermal energy conversion. *Journal of Materials Science: Materials in Electronics*, 2015, 26(8):5553-5561.